

AMERICAN UNIVERSITY OF BEIRUT

SYNTHESIS AND CHARACTERIZATION OF NEW METAL-
ORGANIC FRAMEWORKS FOR SENSING AND
CATALYSIS APPLICATION

by
MAHMOUD KHALED ELCHEIKH MAHMOUD

A thesis
submitted in partial fulfillment of the requirements
for the degree of Master of Science
to the Department of Chemistry
of the Faculty of Arts and Sciences
at the American University of Beirut

Beirut, Lebanon
August 2019

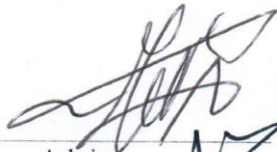
AMERICAN UNIVERSITY OF BEIRUT

SYNTHESIS AND CHARACTERIZATION OF NEW METAL-
ORGANIC FRAMEWORKS FOR SENSING AND
CATALYSIS APPLICATIONS

by
MAHMOUD KHALED ELCHEIKH MAHMOUD

Approved by:

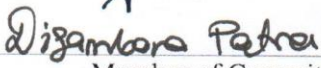
Dr. Mohamad Hmadeh, Assistant Professor
Chemistry


Advisor

Dr. Faraj Hasanayn, Professor
Chemistry


Member of Committee

Dr. Digambara Patra, Professor
Chemistry


Member of Committee

Date of thesis defense: August 30, 2019

AMERICAN UNIVERSITY OF BEIRUT

THESIS, DISSERTATION, PROJECT RELEASE FORM

Student Name: ELCheikh Mahmoud Mahmoud Khaled

Last

First

Middle

Master's Thesis

Master's Project

Doctoral Dissertation

I authorize the American University of Beirut to: (a) reproduce hard or electronic copies of my thesis, dissertation, or project; (b) include such copies in the archives and digital repositories of the University; and (c) make freely available such copies to third parties for research or educational purposes.

I authorize the American University of Beirut, to: (a) reproduce hard or electronic copies of it; (b) include such copies in the archives and digital repositories of the University; and (c) make freely available such copies to third parties for research or educational purposes

after:

One --- year from the date of submission of my thesis, dissertation, or project.

Two --- years from the date of submission of my thesis, dissertation, or project.

Three --- years from the date of submission of my thesis, dissertation, or project.

Mahmoud Elcheikh Mahmoud

28/08/2020

Signature

Date

ACKNOWLEDGEMENTS

First and foremost, I would like to express my gratitude to my advisor, Doctor Mohamad Hmadeh. Doctor Hmadeh has supported me with patience and valuable suggestions while giving me the freedom to work in my own way. I appreciate him helping me complete the writing of this dissertation and his continuous encouragement and support. I attributed my development as a critical and independence research to him and his encouragement, insight and faith in me are greatly appreciated.

I would also like to thank the rest of my thesis committee: Pro. Faraj Hasanayn and Prof. Digambara Patra for their helpful input and feedback.

Many thanks for the staff at the Central Research Science Laboratory (CRSL) for their help and maintenance of various equipment.

I am indebted to all the graduate students who shared this experience with me, I will cherish their encouragement support. Specially, a special thank you goes to current and past Hmadeh group members: Rawan Natour, Fadwa Al Fadel Raad, Ghewa Sabeh, Razan Issa, Rita Douaihy, Fayrouz Abou Ibrahim, Zeinab Nizam, Bouchra Mortada, Zeinab Kara Ali, Hala Atallah, Nour Saad, Asmaa Jradi, Linda Boshnak, and Raafat Ziadeh.

I would like to thank Ms. Manal Ammar and Doctor Ali Youssef for their help, advice and discussion on my research and teaching me some experimental details and skills.

I would like to outspread my thanks and love to all my wonderful friends for their collegial assistance, help, support and the fun times we had together: Fadwa AlFadel Raad, Salah Eddin El Jamal, Rawan Natour, Raafat Ziadeh, Abir Daknach, Fatima Keseerwan, Ghewa Sabeh, Antranik Jonderian, Mostafa Rammal, Anja Finke, Leanne Joy, Lana Kuduzovic and Christina Jalkh. I am so lucky to having you in my life.

A warm and sincere thanks go to my family. I am eternally grateful for their unconditional and everlasting love, their infinite prayers, and for giving me the strength to chase my dreams.

AN ABSTRACT OF THE THESIS

Mahmoud Khaled Elcheikh Mahmoud for Master of Science
Major: Chemistry

Title: Synthesis and characterization of new metal-organic frameworks (MOFs) for sensing and catalysis applications.

Metal organic frameworks (MOFs) are an emerging class of porous materials that have earned a significant amount of attention due to their design flexibility from their building blocks of organic linkers and inorganic clusters. In order to enhance the performance and to develop novel applications using MOFs, we outline here the design and synthesis of new kind of MOFs using new type of linkers. From the proposed linkers, we will be able to prepare a set of new materials with unprecedented electrical, chemical, and topological properties for applications including sensing and catalysis. In our proposed research work, we aimed to synthesize new type of MOFs to be used in sensing and photocatalysis. To this end, a new series of Lanthanides Metal Organic Frameworks (LnMOFs) was synthesized via solvothermal reaction. The four new luminescent MOFs synthesized by mating $\text{LnNO}_3 \cdot 6\text{H}_2\text{O}$ where Ln is (La and Ce) cations with 1,5 dihydroxy-2,6-naphthalenedicarboxylic and 2,6-naphthalenedicarboxylic acid. In this project, AUBM-2(Ce) and AUBM-3(Ce) were selected for sensing the heavy toxic metals (Pb(II), Cr(IV), As(III), Cd(II), Hg(II)) and for paraquat. The hydroxyl-functionalized structures have shown to be promising luminescent sensory materials with high selectivity and sensitivity towards the detection of mercury. In a second part of our research work, our focus was on the development of new MOFs for photocatalysis applications. We report the successful incorporation of the photo-active bis(4-(4-carboxyphenyl)-terpyridine)Ruthenium(II) ($\text{Ru}(\text{cptpy})_2$) strut into a robust metal organic framework, AUBM-4. The single crystal X-ray analysis revealed the formation of a new one-dimensional structure of $\text{Ru}(\text{cptpy})_2$ complexes linked together by Zr atoms that are eight coordinated with O atoms. The chemically stable MOF structure was employed as an efficient photocatalyst for carbon dioxide conversion to formate under visible light irradiation. To the best of our knowledge, the obtained conversion rate was among the highest reported in the literature for similar systems. Our strategy of using the $\text{Ru}(\text{cptpy})_2$ complex as a linker to construct the MOF catalyst appears to be very promising in artificial photosynthesis.

CONTENTS

| | |
|--|-----|
| ACKNOWLEDGEMENTS..... | I |
| ABSTRACT..... | II |
| LIST OF ILLUSTRATIONS..... | III |
| CHAPTER | |
| I. INTRODUCTION | 5 |
| A. Metal-Organic Frameworks (MOFs) | 5 |
| 1. Preamble | 5 |
| 2. Overview of History..... | 6 |
| 3. Design and Synthesis of Metal-Organic Frameworks..... | 9 |
| 4. Metal-Organic Frameworks for Gas Storage and Separation..... | 16 |
| 5. Metal-Organic Frameworks for Sensing..... | 21 |
| 6. Metal Organic Frameworks for Catalysis..... | 24 |
| II. PROJECT 1 | |
| A. Sensing properties of two lanthanides-based metal organic frameworks. | 28 |
| B. Supporting Information..... | 39 |
| III. PROJECT 2 | |
| A. Metal Organic Framework-Photocatalyst Incorporating Bis(4'-(4-Carboxyphenyl)-Terpyridine)Ruthenium(II) for Visible Light-Driven Carbon Dioxide Reduction..... | 60 |
| B. Supporting Information..... | 68 |
| IV. CONCLUSION..... | 81 |

BIBLIOGRAPHY..... 83

ILLUSTRATIONS

| Figure | Page |
|--|------|
| 1.1. Number of metal–organic frameworks (MOFs) structures reported in the Cambridge Structural Database (CSD) from 1978 through 2006 ¹ | 7 |
| 2.1. Part of a Werner complex, Ni(SCN) ₂ (4-methylpyridine) crystal structure. Color code : Ni: green, C: grey, S: yellow, and N:blue ² | 8 |
| 2.2. Example of Hofmann clathrate structure ³ | 8 |
| 2.3. Example of Prussian blue crystal structure ³ | 9 |
| 2.4. Crystal structure of MOF-5 ⁴ . C: black, red: oxygen and yellow ball describes the pore in the network..... | 10 |
| 3.1. Scheme showing different components of MOFs ⁵ | 12 |
| 3.2. Examples of organic linkers..... | 13 |
| 3.3. A general scheme for the post synthetic modification (PSM) of MOFs (top). Example of post-synthetic modification reactions performed with IRMOF-3(bottom).. | 15 |
| 3.4. The prominent diversity of (A) metal clusters, (B) organic linkers incorporated in the synthesis of MOFs..... | 16 |
| 3.5. Crystal Structure of a series of IRMOFs and their corresponding functionalized ligand derivatives. R ₁ = -H, R ₂ = -Br, R ₃ = -NH ₂ , R ₄ = -O-CH ₂ -CH ₂ -CH ₃ , R ₅ = -O-CH ₂ -CH ₂ -CH ₂ -CH ₂ -CH ₃ , R ₆ = -C ₄ H ₂ , R ₇ = -C ₆ H ₄ | 17 |
| 5.1. Illustration of emission prospects in a porous Metal-Organic Frameworks, where the inorganic clusters (blue) are coordinated to organic linkers (yellow) with an incorporated guest (green) ⁶ | 23 |
| 5.2. A schematic diagram of the antenna effect ⁷ | 24 |
| 6.1. (a) Coordinatively unsaturated metal connecting points as active catalytic sites. (b) Incorporation of active catalytic sites into the bridging ligands of MOFs..... | 27 |

CHAPTER I

INTRODUCTION

1. Preamble

Metal organic frameworks (MOFs) are a novel class of crystalline materials comprised of metal nodes and organic linkers connected via coordination bonds. These materials are organized in a 1D, 2D, or 3D extended network so that pores of regular sizes are obtained⁸. MOFs constitute an active research topic for the past twenty years due to their rich chemistry and unique characteristics such as high surface area exceeding 10000 m²/g,⁹⁻¹⁰ relatively high mechanical and thermal stabilities¹¹⁻¹², along with the possibility of being adjusted while conserving the functional sites¹³. MOFs showed great potential applications in several fields including catalysis¹⁴, gas storage¹⁵, magnetism¹⁶, sensing, adsorption¹⁷ and luminescence¹⁸, in addition to drug delivery¹⁹, biomedical imaging²⁰, antimicrobial activity²¹, dye sensitized solar cells²², storage and encapsulation of dyes and pH sensitive molecules²³⁻²⁴. Moreover, synthesis of MOFs is directed under mild conditions. Where many kinds of functional groups can be incorporated directly into their structure, which is sometimes problematic for zeolites and carbon-based porous materials. Interestingly the pore shape, pore size, surface functionalities, and network topology can be tuned systematically by altering the metal clusters and /or the organic linkers. Therefore, the structures and properties of MOFs can be designed to fit the needs of specific applications. MOFs are very attractive because of their tunability and remarkable degree of diversity in the inorganic and organic units they can possess in their structures, a feature that make MOF chemistry as one of the most developed field in

material science¹. In this chapter, the development of MOFs is reviewed, and their applications in sensing and catalysis will be discussed.

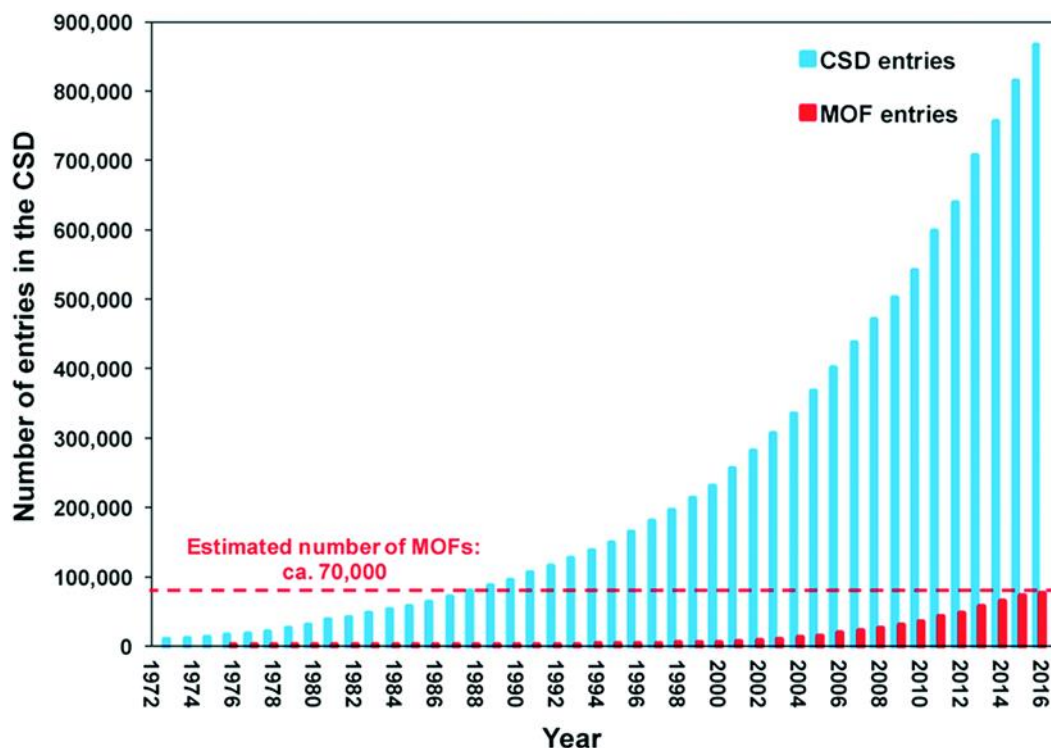


Figure 1.1. Number of metal–organic frameworks (MOFs) structures reported in the Cambridge Structural Database (CSD) from 1978 through 2006¹. The bar graph illustrates the recent dramatic increase in the number of reports.

2. Overview of History

Coordination compounds were studied for the first time by Alfred Werner (1866–1919). Werner-type complexes were based on using metal centers and nitrogen organic linkers with a general formula of MX_2L_4 . Where M is consigned to divalent metal in an octahedral geometry (e.g. Zn, Cu), X is assigned to an anionic ligand (e.g. NCO^- , CN^- , NO_3^-), and L is consigned to pyridine coordinated molecule (Figure 1.2).

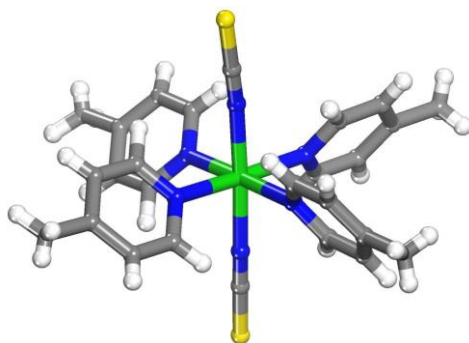


Figure 2.1. Part of a Werner complex, $\text{Ni}(\text{SCN})_2(4\text{-methylpyridine})$ crystal structure. Color code : Ni: green, C: grey, S: yellow, and N: blue².

At the era of 1960s, other illustrations that involved compounds of Hofmann-type clathrate were discovered and fully investigated by Iwamoto and co-workers, and these compounds were extracted from an original one that had the formula $\text{Ni}(\text{NH}_3)_2(\text{CN})_4(\text{C}_6\text{H}_6)$ and was discovered by K.A. Hofmann (Figure 1.3).

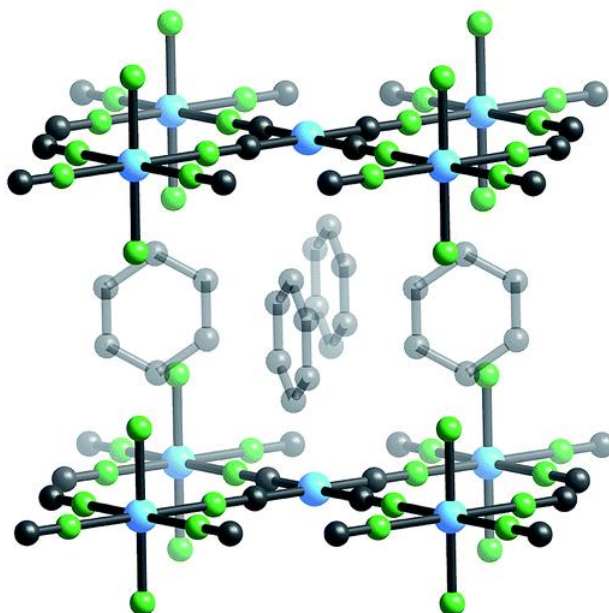


Figure 2.2. Example of Hofmann clathrate structure³.

In the early 1970, another type of compounds, known as Prussian blue, were synthesized, consisting of mixed valence Fe ions bridged via cyano-entity, and identified by X-ray technique (Figure 1.4).

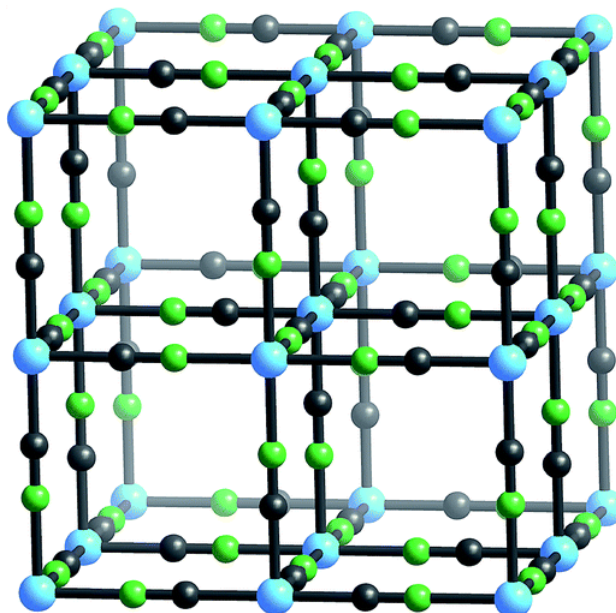


Figure 2.3. Example of Prussian blue crystal structure³.

In 1956, the first natural Zeolites were discovered by Axel Frederik Cronstedt, namely Stilbite. Since then, research on this class of porous materials has increased significantly. Moreover, in 1990, functional microporous materials started to appear when Robson and co-workers reported porous coordination polymers which exhibited ion exchange properties²⁵. In the meantime, Omar M. Yaghi and co-workers synthesized an innovator compound (MOF-5) that has been reported to be the first robust and highly porous hybrid material, as compared to zeolite and activated carbon⁴. MOF-5 is synthesized from zinc acetate building block and 1,4-dicarboxylic acid, having a **pcu**-topology (Figure 1.5).

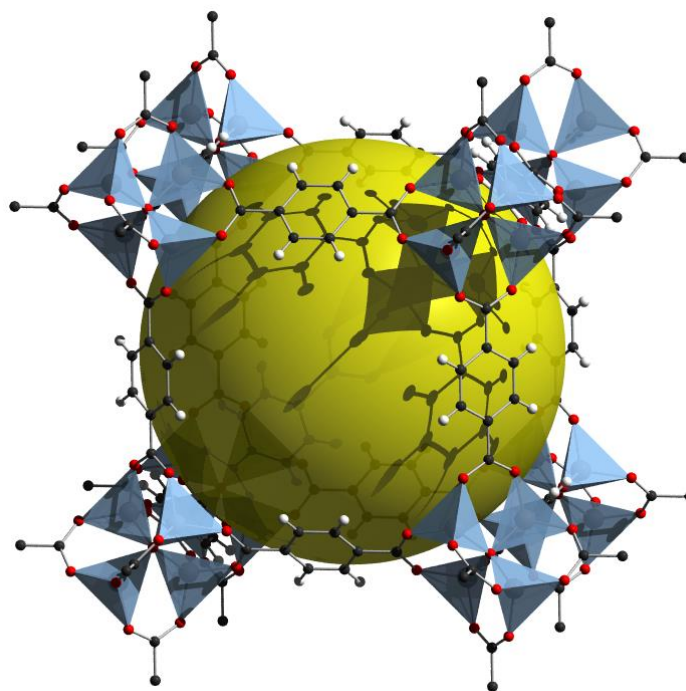


Figure 2.4. Crystal structure of MOF-5⁴. C: black, red: oxygen and yellow ball describes the pore in the network.

From 1990s, MOFs have become one of the hottest topics in material chemistry, which have world-wide unique growth. The variability in the potential geometry, size, permanent porosity, adjusted pore size, and functionality has opened the way for more than 20,000 various MOFs to be created and characterized over the past few decades¹³.

3. Design and Synthesis of Metal-Organic Frameworks

Metal-organic frameworks (MOFs) are composed of metal nodes and organic linkers connected via strong bonds organized in 1D, 2D or 3D networks (Figure 1.6). Technically, an extensive variety of structural, electrical, optical, and catalytic properties can be incorporated into the frameworks by coherent design.

The inorganic components of MOFs are usually transition metal ions. Importantly many different metal ions are known to favor different coordination numbers and geometries, which include tetrahedral, linear, square-planer, octahedral, trigonal-bipyramidal, T-shaped, and square-planer. For instance, Cu(II) ions that are known to have d^9 electronic configurations favor the square-planer geometries; however, it can also exist with other coordination numbers, contingent on the choice of organic solvents and ligands²⁶. Moreover lanthanide ions are also used to create and design novel network topologies due to their large coordination numbers (up to 10)²⁷.

For the organic part of the MOFs, there are extensive diversity of selections as well. Ligands with rigid backbones are frequently chosen, because these types of linkers facilitate to predict the network geometry prior synthesis. In addition, the rigidity plays an important role in sustaining the open pore structure of the MOF after the removal of the included solvents. The organic linkers used in MOFs can be classified into three groups anionic, or cationic linkers, and electrically neutral organic linkers (Figure 1.7). The mostly used anionic linkers are carboxylates²⁸ since they have the ability to aggregate metal ions into clusters in this manner forming more stable frameworks. Cationic organic linkers are little used because of their low attractions for cationic metal ion²⁹⁻³⁰. Interestingly the most regularly used neutral organics linkers are pyrazine and 4,4'-bipyridine (bpy)³¹⁻³². These linkers are particularly suitable as pillars in the creation of pillared layer in 3D network³³⁻³⁴.

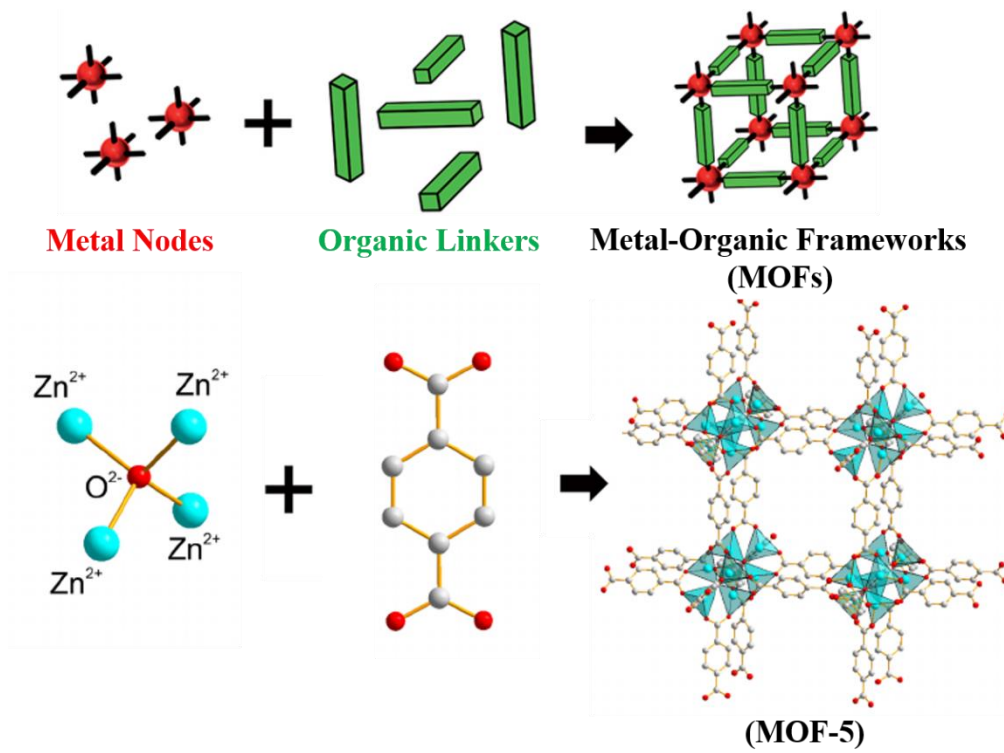


Figure 3.1. Scheme showing different components of MOFs⁵.

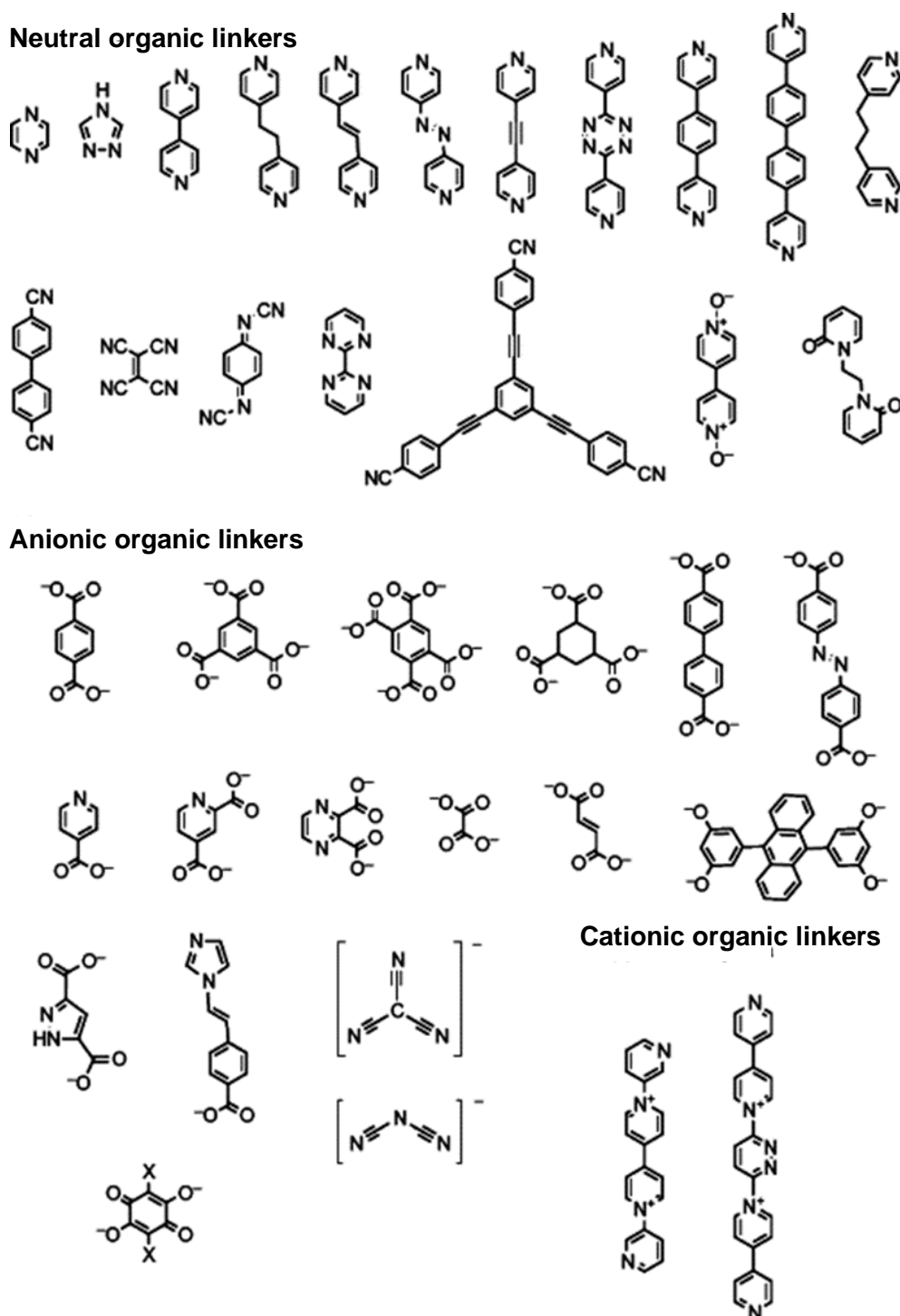


Figure 3.2. Examples of organic linkers³⁵.

Metal Organic frameworks (MOFs) are usually synthesized via solvothermal techniques, where the reactions are accomplished in an organic solvent or in water at high temperatures in a closed system. However, these methods demand long reaction times,

from some hours up to several days, depending upon the desired MOF and the reaction solvent, concentration, temperature, and other conditions. Alternative synthetic strategies have been developed based on exploiting conventional electric or microwave heating, electrochemistry, mechanochemistry, and ultrasonication.³⁶⁻³⁷ These techniques can also regulate the crystal size from millimeter down to micrometer by varying the concentration and the temperature of the reactants in the solution. One of the main advantages of MOFs is the ability to incorporate complex functionalities into the frameworks backbones. However, it is difficult sometimes to introduce functional groups during MOFs synthesis, nevertheless integrating the functionality may be accomplished through post synthetic modification (PSM), which is the chemical derivatization of MOFs after their formation³⁸ (Figure 1.8). MOFs can be post synthetically modified by different methods, where new functional groups are incorporated using covalent³⁹⁻⁴⁰, non-covalent^{25, 41}, or coordinative interactions⁴²⁻⁴³. Some of the common reactions to accomplish PSM are postmetallation⁴⁴⁻⁴⁵ and protonation⁴⁶. Interestingly, PSM method can incorporate a broad range of functional groups to create a series of functionally within the MOF structures without altering the topology.

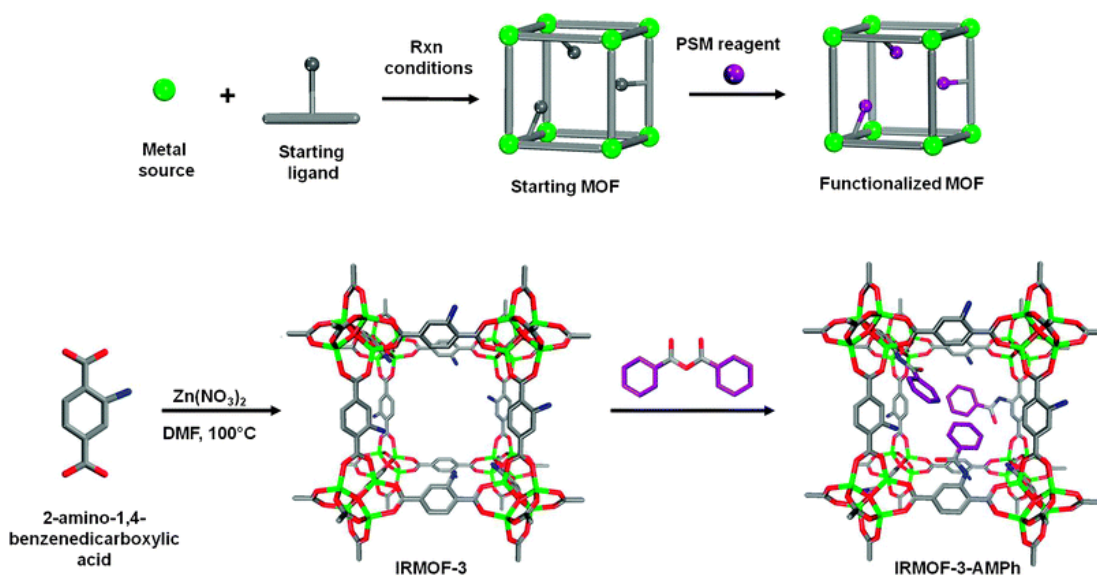


Figure 3.3. A general scheme for the post synthetic modification (PSM) of MOFs (top). Example of post-synthetic modification reactions performed with IRMOF-3(bottom)⁴⁷.

The conspicuous interest in MOFs does not rely back on their high surface areas only, but also on the immense number of metal salts and organic linkers that could be incorporated in the synthesis processes⁴⁸ (Figure 1.9). This variety in the choice of metal ions and organic linkers leads to a diversity of MOFs having different structures with altered properties and targeted for various applications including gas storage, separations and catalysis. In some cases, neither the crystal structure nor the properties of the MOF change upon varying the functionalities of the organic linkers, such types are called isorecticular MOFs (IRMOFs)⁴⁹ as shown in (Figure 1.10).

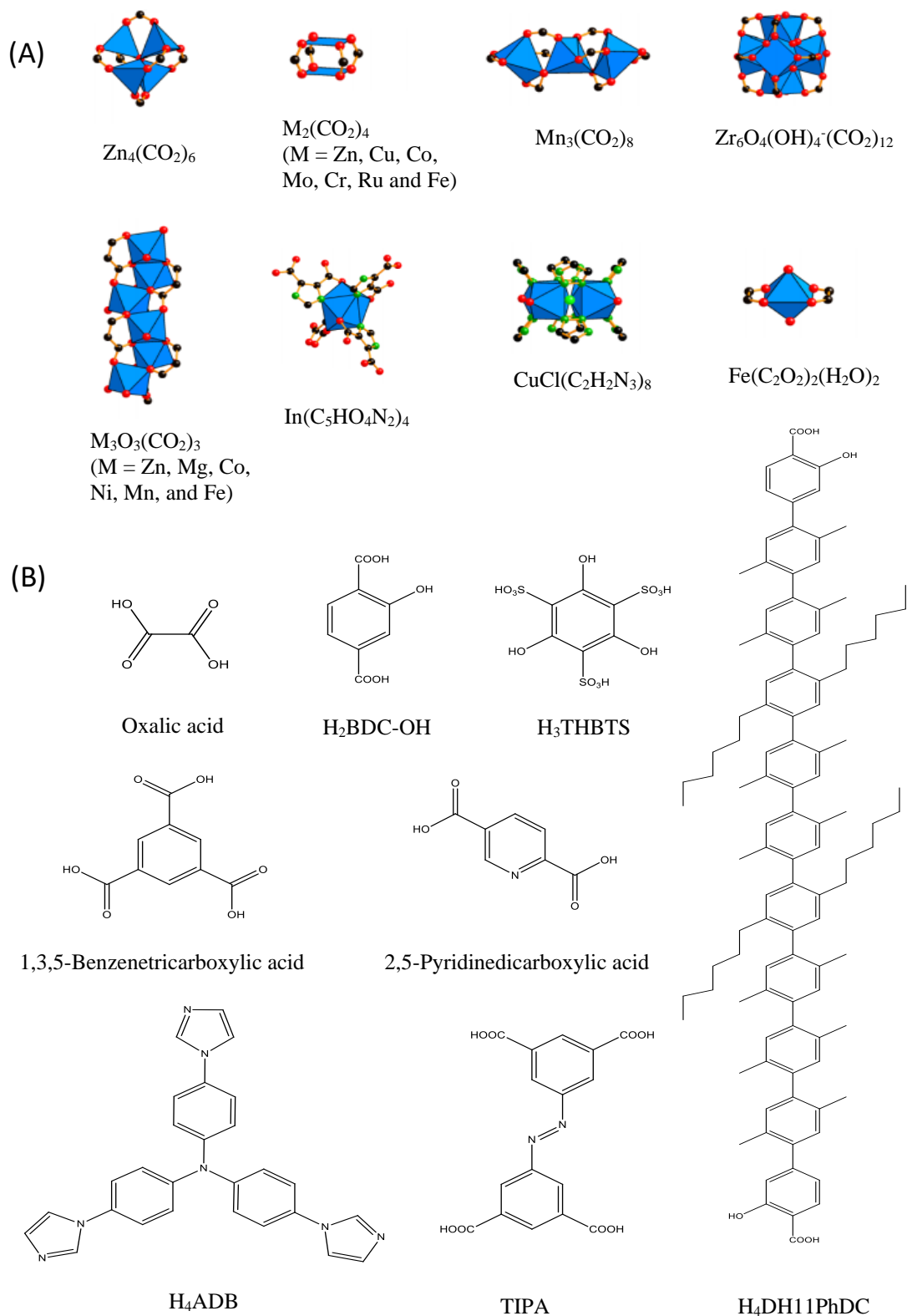


Figure 3.4. The prominent diversity of (A) metal clusters, (B) organic linkers incorporated in the synthesis of MOFs.

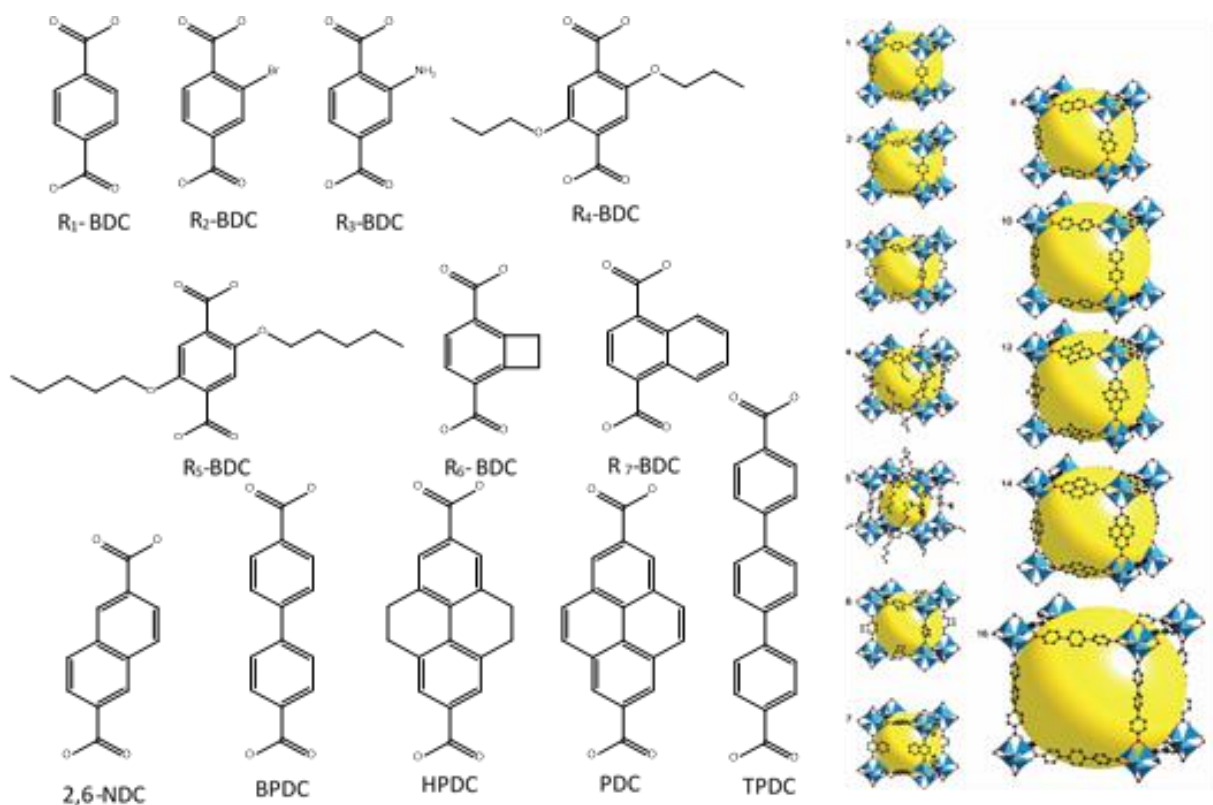


Figure 3.5. Crystal Structure of a series of IRMOFs and their corresponding functionalized ligand derivatives. $R_1 = -H$, $R_2 = -Br$, $R_3 = -NH_2$, $R_4 = -O-CH_2-CH_2-CH_3$, $R_5 = -O-CH_2-CH_2-CH_2-CH_2-CH_3$, $R_6 = -C_3H_5$, $R_7 = -C_6H_5$.

4. Metal-Organic Frameworks for Gas Storage and Separation

Metal-organic frameworks (MOFs) are porous materials made from the coordinative bonding between inorganic clusters (metal ions) and organic linkers. These materials are considered as a unique adsorbent due to many extraordinary properties. One of these, is the diversity in the functionality of metal ions and linkers that provide a great improvement in gas adsorption/selectivity properties. Moreover, since the pores of these materials are homogenous in size and cohesive in their function, a non-hysteretic recyclability in the uptake and release of gases was reported. Additionally, compared to other porous materials, the pores in MOFs have no walls, which in turn can provide a

facile uptake and release of carbon dioxide (several orders of magnitude faster than in zeolites and porous carbon materials). Most importantly, what characterizes MOFs is that they are made from readily available highly scalable starting materials (from grams to multi-ton quantities) in addition to their high thermal stability in air (up to 400-500 °C) as well as a high chemical stability (boiling water, organic solvents). Therefore, the flexibility with which these materials can be tailored on the molecular level for many applications including gas storage and separation has led to the highest uptakes ever reported for many gases including hydrogen, methane, and carbon dioxide.

Recently, the energy needs of the world are gradually increasing, which is leading to a depletion in the fossil fuel reserves. Therefore, renewable ways to generate, store, and deliver energy are being investigated. Interestingly, Hydrogen has been considered as a near-ideal clean energy material due to its zero-carbon content, and its high gravimetric energy density, which can nearly triple that of gasoline. Besides, hydrogen can be generated from an almost inexhaustible resource water. However, one of the biggest bottlenecks in achieving a hydrogen economy, is the lack of a safe, efficient, and economical on-board hydrogen storage system., the US department of Energy (DOE) has set certain standards for a hydrogen storage system which are 0.075 kg/kg and 0.070 kg/L for gravimetric and volumetric storage, respectively. By 2012, Those capacities reached 0.055 kg/kg for the gravimetric and 0.040 kg/L for the volumetric systems. In addition, these storage systems should be able to operate between -40 and 85 °C, at pressures less than 100 bar, and tolerate 1000 use-cycles by 2010 and 1500 use-cycles by 2015¹.

MOF-5, which is called IRMOF-1 or Zn₄O(BDC)₃ (BDC = 1,4-benzenedicarboxylate), was one of the first MOFs examined for hydrogen storage due to its high porosity, high surface area (4400 m²/g), and stable structure in the absence of guest molecules⁵⁰. The

measured sorption isotherm for H₂ at 78 K reveals type I behaviour, in which saturation is reached at low pressures followed by a pseudo-plateau at higher pressures. At 78 K and 1 bar, the H₂ uptake of IRMOF-1 is 4.5 wt%, which corresponds to 17.2 H₂ per Zn₄O(BDC)₃ formula unit. However, at room temperature, the uptake of H₂ by IRMOF-1 increases linearly with pressure reaching 1.0 wt % at 20 bars. Researchers further realized that the H₂ uptake capacity of IRMOF-1 varies according to the method used to prepare and activate it⁵¹⁻⁵⁶.

According to several computational studies, MOFs at room temperature adsorb little hydrogen even under high pressures. This is due to the low interaction energy between the framework and physisorbed H₂... To overcome this problem, researchers synthesized new MOFs containing unsaturated metal centers, which are able to chemisorb H₂ either as intact molecules or by oxidative addition⁵⁷⁻⁵⁹. This method has been shown to enhance the H₂ adsorption enthalpies.

Recently, Yaghi and his research team synthesized a new MOF namely MOF-210 with ultra-high surface area⁶⁰, (6240 m²/g). The team found that the H₂ uptake of this newly MOF (86 mg g⁻¹), was higher than the H₂ uptake of MOF-5, MOF-177, UMCM-2, and NOTT-112.⁹⁻¹² Additionally, the calculated total hydrogen uptake in MOF-210 (176 mg g⁻¹) exceeds that of typical alternative fuels (methanol and ethanol and hydrocarbons (pentane and hexane)). Moreover, MOF-210 also showed large total hydrogen uptake (163 mg g⁻¹, which was higher than that of MOF-177)⁶¹. Unfortunately, there is currently no material that demonstrates promising hydrogen uptake at room temperature (RT). This could be due to the weak adsorbent-adsorbate interaction caused by insufficient binding sites. As a result, novel materials having high micro-porosity must

be developed in order to realize a compact fuel tank. Noting that, MOF-210 is reported to have the highest hydrogen uptake of 2.7 wt% at RT.

4.1 Methane storage in MOFs

As an alternative fuel, methane is also an important candidate⁶²⁻⁶⁴. Methane is the primary component of natural gas, is cleaner than petrol, provides more energy because of its higher hydrogen to carbon ratio, and produces lower carbon emissions. Methane is abundant and inexpensive compared with conventional fossil fuels, such as gasoline and diesel. However, in order to produce compact automobiles with a driving range of several hundred miles, an effective and safe on-board storage system must be achieved. The current storage target set by the DOE is 180 cm³ cm⁻³ (standard condition for temperature and pressure (STP)) at 35 bars, which is comparable to the energy density of compressed natural gas at 250 bar²³. For a porous framework to achieve the DOE targets, it must satisfy the following requirements: significant adsorption capacity, efficient charge/discharge rate, high hydrophobicity, moderate adsorption enthalpy and high heat capacity⁶⁵.

The gravimetric uptake of methane is generally proportional to the BET surface area of porous solids. Furthermore, most conventional inorganic materials with BET surface areas of 1000 m² g⁻¹ do not take up large amounts of methane at 35 bar; for example zeolites (31-82 mg g⁻¹)⁶⁶⁻⁶⁹ and mesoporous silicas (14-65 mg g⁻¹)⁶². However, if the BET surface area reaches more than 2000 m² g⁻¹, we can expect a large amount of methane uptake; this is the case for activated carbons and MOFs with methane uptake of 160mg g⁻¹.¹³ One of the best performing MOFs takes up 253 mg g⁻¹ of methane at 290

K⁷⁰, which is even greater than the uptake of high-surface-area carbons (211 mg g⁻¹ for Max_{sorb} and 250 mg g⁻¹ for chemically activated anthracite taken at 293 K)⁷¹⁻⁷². On the other hand, methane uptake by MOFs with ultra-high surface area was also measured at 298 K. The calculated total uptakes for MOF-200, 205 and 210 were 446, 394, and 476 mg g⁻¹ respectively which were 50% greater than those of the anthracene-based MOFs, Porous Coordination Network-14 (PCN-14)⁷⁰. It is worth noting that the corresponding volumetric methane densities in the present MOFs are 2, 3, and 2.5 times greater than volumetric bulk density (g L⁻¹) of methane at the same temperature and pressure. More importantly, the isotherms are nearly linear up to 80 bars, so that these materials can deliver most of the sorbed methane in the pressure range of 10–100 bar.

4.2. Carbon dioxide capture and separation

To stabilize atmospheric CO₂ levels, it is necessary to develop CO₂ capture and sequestration technologies (i.e. short- and long-term CO₂ storage as well as selective CO₂ separation)⁷³⁻⁷⁴. The capture and separation of CO₂ can be achieved by using solvents, cryogenic techniques, and solid sorbents⁷⁵. To date, most of the processes in large-scale operations are performed by amine-based wet scrubbing systems (i.e. post-combustion CO₂ capture by chemisorption)⁷⁶⁻⁷⁷, because the low CO₂ partial pressure and high flue gas temperature (50-120 °C) require strong interaction with CO₂.⁷³ However, these processes suffer from high regeneration energy, large equipment size, solvent degradation and equipment corrosion⁷⁵. Therefore, adsorption separation is considered a more promising method for cost-effective CO₂ recovery. Recently, two novel technological pathways were proposed for CO₂ capture systems: pre-combustion capture and oxy-combustion⁷⁶⁻⁷⁷. Since CO₂ concentrations in these gas streams are much higher than in the flue gas streams in post-combustion capture, many limitations of the state-of-the-art

amine-based systems may be resolved by using these technological pathways in combination with highly porous solids.

The saturation CO₂ uptake in porous solids is again proportional to the porosity of the materials. High surface area MOFs such as MOF-177 and MIL-101 show good CO₂ uptakes (1490 and 1760 mg g⁻¹)⁷⁸⁻⁷⁹, which are greater than those of MOF-5 (970 mg g⁻¹), carbon materials (420 and 370 mg g⁻¹ for Norit RB2 and BPL carbon) and zeolites (220-350 mg g⁻¹)⁷⁸⁻⁸⁰. The high CO₂ storage capacity is a requirement for short-term CO₂ storage and transport of CO₂. More recently, the CO₂ uptake capacity of the ultra-high surface area MOFs were tested. Owing to the large storage volumes, the CO₂ uptake value of 2,400 cm³ g⁻¹ in both MOF-200 and 210 exceeds those of any other porous materials.

Regarding CO₂ separation, strong binding energy is relatively more important than large storage space. The materials presently used for separation applications are amine solutions, zeolites, and porous membranes. MOFs have been shown to exhibit exceptional CO₂ storage capacity under equilibrium conditions when pure CO₂ is introduced into the pores⁸¹⁻⁸⁶. However, their capacities are dramatically reduced when exposed to mixtures of gases under dynamic conditions, as would be the case in power plant flue gas and methane mining applications. Recently, it is reported that a MOF replete with open magnesium sites (Mg-MOF-74) has excellent selectivity, facile regeneration, and among the highest dynamic capacities reported for CO₂ in porous materials. Through separation experiments, the metal environment in the framework can drastically change the gas selectivities if these metals are coordinatively unsaturated^{78, 87}. Therefore, the incorporation of heterogeneity into the MOF system plays a key role in improving the selective gas capture.

5. Metal-Organic Frameworks for Chemical Sensing.

Luminescence quenching is a significant method to detect small amount of analyte in a solution⁸⁸. Luminescence can be divided into three essential types. The first one is fluorescence; which spin is allowed and has numerous lifetimes values in nanoseconds. The second type is phosphorescence, which spin is prohibited and has some lifetime values that can be as long as numerous seconds. While the third type is scintillation, which is a light emission stimulated by exposition to ionizing radiation⁸⁹. Scintillation also has lifetimes in the order of nanoseconds.

There are several routes to synthesize luminescent MOFs (Figure 5.1). The most common way is to combine luminescence inorganic metal clusters. The best choices for these materials are lanthanide ions, particularly La(III) and Ce(III), due to the robust visible luminescence of these ions in the red and green regions. Moreover, the electronic transitions of lanthanide ions are prohibited according to Laporte selection rules, which leads to low quantum yields and weak absorbance, the prohibition can be exceeded by mating a strongly absorbing element called a lumiphore into the MOF framework. When exposed to irradiation, lumiphores can easily transfer energy from their triplet excited state to the lanthanides emitting states, in condition that there is a robust vibronic connection between the lumiphore and the cluster (Figure 5.2). This phenomenon, called the antenna effect, is responsible for a great increase in luminescence production by the lanthanide ion. Decent organic lumiphores are molecules with large conjugate pi systems. In the solid state, if lumiphores are in near immediacy, electronic interaction, ligand to ligand charge transfer, can influence, the luminescence⁹⁰.

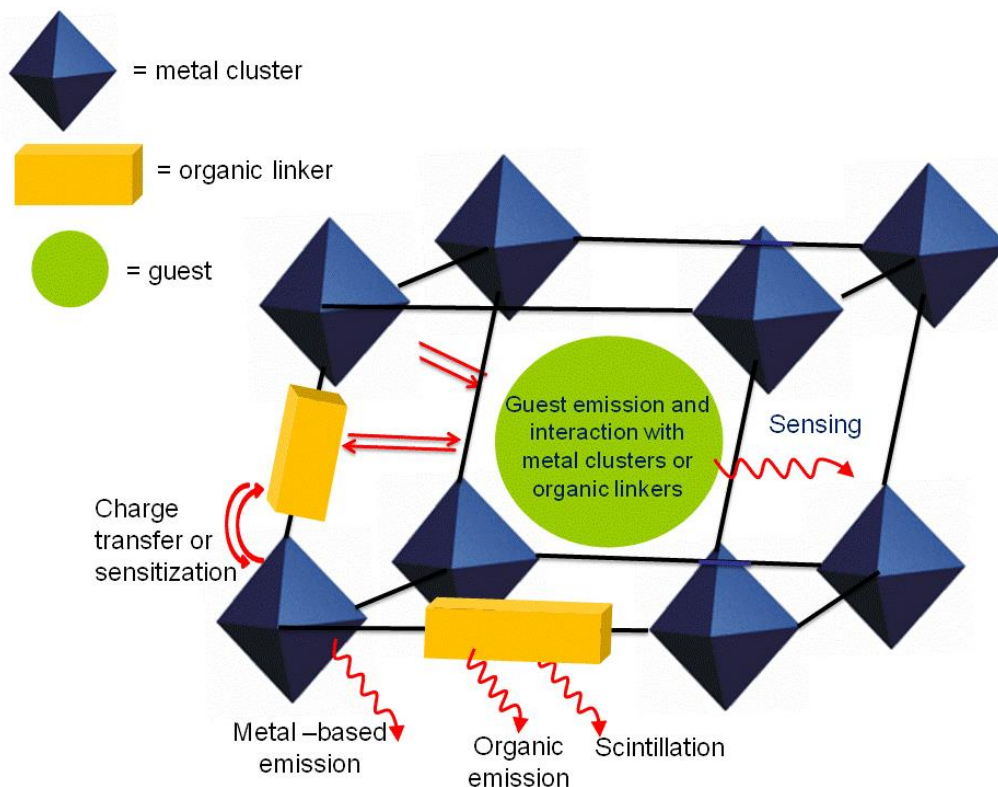


Figure 5.1. Illustration of emission prospects in a porous Metal-Organic Frameworks, where the inorganic clusters (blue) are coordinated to organic linkers (yellow) with an incorporated guest (green) ⁶.

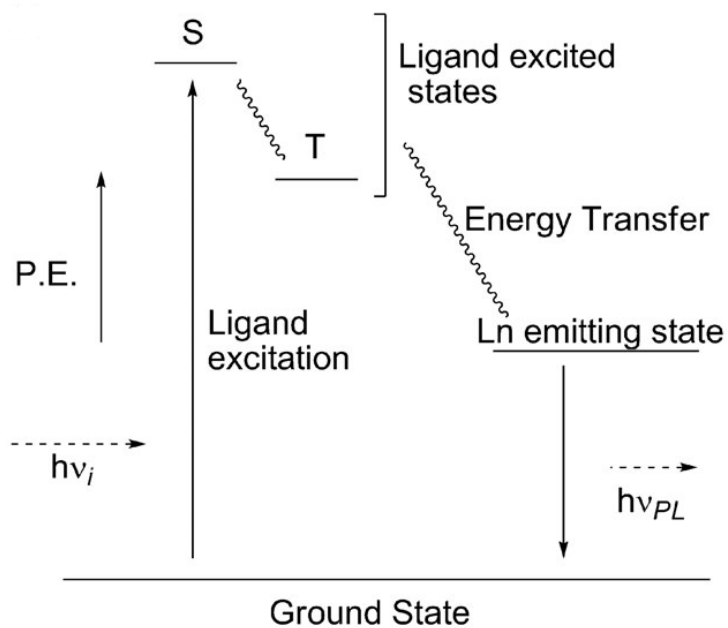


Figure 5.2. A schematic diagram of the antenna effect ⁷.

Numerous detection methods have been projected to use luminescent MOFs as prospective sensors. One of these ways is wavelength shift. For instance, the fluorescence emission wavelength of $Zn_4O(NTB)_2 \cdot 3DEF \cdot EtOH$ (H_3NTB is 4,4',4''-nitrilotrisbenzoic acid) shifts depend on the existence of the guest molecules in the MOF framework. The desolvation of this MOF result into a blue shift in the luminescence maximum by the reason of the absence of π - π interactions between the interpenetrated networks.

Another detection method engages intensity changes. For example, $Eu(BTC)$ MOF shows an expressive quenching and enhancement of its photoluminescence when exposed to acetone and DMF, respectively⁹¹. Also, the $Eu(PDC)$ and $Tb(BTC)$ MOFs have the ability to sense and detect anions and metal ions, which bind to nitrogen atoms and O-H groups in the MOF, respectively⁹²⁻⁹³. Moreover, Li and co-workers used luminescence quenching of MOFs in the detection of explosives⁹⁴. They created a Zn-MOF that includes 4,4'-biphenyldicarboxylate and 1,2-bipyridylethene linkers. The MOF fluorescence shows a clear quenching by 2,3-dimethyl-2,3-dinitrobutane (DMNB) and 2,4-dinitrotoluene (DNT)⁹⁴.

6. Metal-Organic Frameworks for Catalysis.

MOFs are used as rigid platforms for physical interactions such as gas storage and separation, as well as chemical reactions such as catalysis. MOFs not only have the same catalytic features of zeolites such as porosity, diversity in pore sizes and shapes, but also contain functionalizable organic linkers. These features make the materials great candidates as heterogeneous catalysts, which can have liquid-like diffusion properties, a variety of chemical functionalities, and can be tuneable⁹⁵⁻⁹⁶. Most catalytic applications have been explored by using parts of the structure as the catalytic function, either through

the metal moiety or the organic linker molecules. It has been shown that the introduction of open metal centers into MOFs can offer a promising tool in catalysis because of the regular arrangement of metal centers in the pore channels that induces regioselectivity or shape or size selectivity⁹⁷. Catalytically active coordinately unsaturated metal sites can be introduced into MOFs in two ways, either as metal connecting points or as part of the linker⁹⁸ (Figure 6.1).

MOFs can be used as heterogenous catalysts, which offer many potential advantages in photocatalytic process, due to the fact that: (i) their band-gap values can be tuned to absorb visible light efficiently; (ii) their high surface area results in good contact with CO₂ and water; it is expected that MOFs will have a high affinity towards CO₂ molecules,⁹⁹ thus increasing the interaction between the photocatalyst and the reactant, and increasing the efficiency of photocatalytic reactions;¹⁰⁰ (iii) their particles can be easily synthesized with different sizes; (iv) their synthesis is very cost effective; (v) the crystals are stable and can be easily dispersed in water (Zr, Al, and Cu versions); (vi) their electrical properties can be tuned upon incorporation of different metal cations into their SBUs¹⁰¹ and (vii) only very few MOFs have been explored as photocatalysts for carbon dioxide reduction, water splitting, and their application towards solar fuels production. Because of the strong chemical bonding and higher coordination number, the Zr-based SBU, Zr₆O₄(OH)₄(CO₂)₁₂, found in UiO-66¹⁰² (Zr₆O₄(OH)₄(BDC)₆; BDC = terephthalate) is one of most stable inorganic clusters.¹⁰³ Thus, this inorganic SBU appears as a notable platform to construct the thermally and chemically stable MOFs that are critical for practical applications.

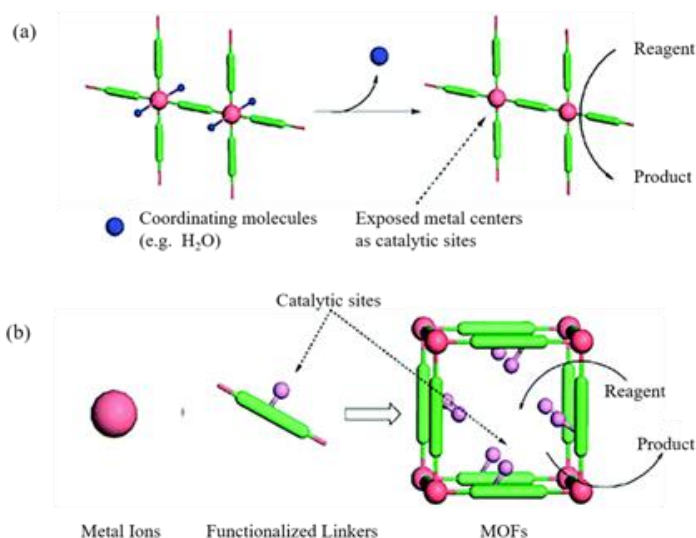


Figure 6.1. (a) Coordinatively unsaturated metal connecting points as active catalytic sites. (b) Incorporation of active catalytic sites into the bridging ligands of MOFs¹⁰⁴.

6.1. Photocatalytic CO₂ by metal organic framework (MOFs)

Due to the redundant emission of carbon dioxide (CO₂) that has greatly affected the global environment., effective capture and transformation of CO₂ has become a top priority from the point of sustainable development. Among several methods, one of the particularly attractive solutions is the photocatalytic reduction of CO₂ into useful and high value-added industrial chemicals such as formic acid, formaldehyde, methanol or methane¹⁰⁵⁻¹⁰⁶. The photocatalytic reduction of CO₂ can progress at a normal operation temperature and pressure. The development of efficient photocatalysts is of great importance. Traditional inorganic semiconductor materials, like TiO₂, have shown a certain photocatalytic activity for CO₂ reduction, while some of them are active under only UV light or display a high recombination rate of photoinduced electron–hole pairs, hence hinder the promotion of catalytic efficiency¹⁰⁷⁻¹⁰⁹. Thus, the design and development of a new photocatalyst is a promising method to realize efficient

photochemical transformation. The use of metal organic frameworks (MOFs) as new functional hybrid materials have shown excellent performance in the field of gas adsorption/separation, luminescence, sensing and catalysis due to their flexible structures and tunable porosity¹¹⁰. Photoactive MOFs have made outstanding progress in the field of photocatalysis, especially for CO₂ reduction¹¹¹⁻¹¹². By presenting appropriate optical functional organic or inorganic components, MOFs can adjust their own photochemical properties and realize light harvesting. The integration of new structures and functionalities makes MOFs tunable porous photocatalysts for CO₂ reduction. Among numerous MOFs, zirconium based MOFs have attracted general attention because of their high thermal and chemical stability where their robust nature could deal with complicated and harsh catalytic conditions¹¹³. Through the excited ligand to Zr clusters charge transfer process (LMCT) or the catalytic role of the ligand itself, Zr-MOFs show selective catalytic reduction of CO₂¹¹⁴⁻¹¹⁵. Moreover, due to the large band gap of Zr clusters, the visible light response of Zr-MOFs mainly depends on the functional ligand. Some strategies such as utilizing a precious metal complex ligand or highly conjugated ligand have been investigated while taking advantage of an amino group functionalized ligand, which is an easy and effective strategy to extend the light absorption of MOFs¹¹⁶.

The possibility of functionally altering MOFs, by post-synthetic modification (PSM), leads to the formation of advanced MOF materials that are suitable for more specialized applications¹¹⁷⁻¹²⁰. Following this route, free functional groups in a polytopic ligand constituting the MOF, can be modified after the MOF synthesis and isolation. An example of PSM is the work done by Farrusseng and his team that aimed at converting the amino group in MIL-53(Al)-NH₂ into isocyanate through a multiple-step process¹²¹. On the other hand, Cohen and his team managed to perform several approaches to utilize

the free functional group for catalysis; as in the case of post metalation of UIO-67-bpydc (a zirconium-based MOF) with manganese, thus achieving a photocatalyst for CO₂ reduction. In addition, Lin and coworkers have incorporated light-harvesting molecules, such as Ru(bpy)₃²⁺, into the backbones of MOFs to study the exciton transport in molecular solids and catalysis of light-driven organic transformations. Moreover, they included water oxidation and proton/carbon dioxide reduction catalysts into MOF structures to catalyze water oxidation and proton/CO₂ reduction half reactions, respectively¹²²⁻¹²⁵.

While the reported studies on Carbon dioxide reduction are interesting and informative, these works have raised a number of questions and produced a collection of uncertainties and confusions, relating to the difficulty of quantitatively analyzing and comparing the performance metrics of different kinds of photocatalysts. The concomitant challenge of evaluating and distinguishing a real effect from artifacts associated with adventitious carbon contamination pervasive on the surface of these photocatalysts can provide false positives of their real performance metrics. Indeed, integrated ¹³C and ²H isotope tracer capability to probe mechanistic details of photoactivity should be used in routine analysis.

Our work will focus on the design and synthesis of new MOF photocatalysts by combining molecular complexes linkers and zirconium-based clusters into highly stable frameworks.

CHAPTER II

A. Sensing properties of two lanthanides-based metal organic frameworks.

In this work, we targeted the development of new sensors based on MOF structures. For an efficient and successful MOFs sensor, the ligands should have both a binding site and possess luminescent properties. Our metals of choice were lanthanides due to their interesting binding and fluorescence properties. When synthesizing Ln-MOFs, the organic linkers are important for the structure because of the antenna effect that may occur in such structures.¹²⁶ Thereby, in agreement with the hard-soft acid base model, carboxylated ligands are convenient in building lanthanides MOFs. This is because lanthanide ions are hard acceptors, favoring the coordination with hard carboxylate oxygen. Moreover, the luminescence of the lanthanides can be enhanced and intensified upon choosing aromatic carboxylic groups, the latter being a fine luminescent chromophore.¹²⁷ Thus to obtain an effective lanthanides MOFs sensor,¹²⁸ the best approach is to select a conjugated aromatic organic linker with Lewis base sites where the luminescence can be improved along with a potential metal ion binding site.¹²⁹

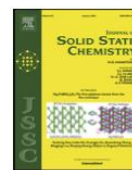
In this part 2,6-Naphthalenedicarboxylic and 1,5-dihydroxy 2,6-Naphthalenedicarboxylic were selected to react with Lanthanides cations where lanthanides are (La, Ce). After varying many experimental conditions such as reagent concentrations, solvent mixtures, temperature and pHs, we succeeded in synthesizing two sets of new lanthanides MOFs namely AUBM-2 and AUBM-3 using both linkers (NP and DNP). The synthesis and full characterization (e.g. SXRD analysis,

thermogravimetric analysis, and Fluorescence) of the MOFs are reported, in addition to their applications for heavy metal sensing and paraquat were investigated. The results of this work are presented in the form of a research paper published in the Solid-State Chemistry Journal in 2020.



Contents lists available at ScienceDirect

Journal of Solid State Chemistry

journal homepage: www.elsevier.com/locate/jssc

Lanthanides based metal organic frameworks for luminescence sensing of toxic metal ions



Mahmoud Elcheikh Mahmoud^a, Zeinab Moussa^a, Thirumurugan Prakasam^b, Liang Li^b,
Mohamad G. Abiad^c, Digambara Patra^{a,*}, Mohamad Hmadeh^{a,**}

^a Chemistry Department, American University of Beirut, PO Box 11-0236, Riad El Solh, Beirut, 1107-2020, Lebanon

^b New York University Abu Dhabi (NYUAD), Experimental Research Building, Building C1, Saadiyat Island, Abu Dhabi, United Arab Emirates

^c Department of Nutrition and Food Sciences, American University of Beirut, PO Box 11-0236, Riad El Solh, Beirut, 1107-2020, Lebanon

ARTICLE INFO

Keywords:

Metal organic frameworks (MOFs)
Sensing
Fluorescence
Mercury
Heavy metals
Paraquat

ABSTRACT

Two set of lanthanides-based metal organic framework structures incorporating 2,6-naphthalenedicarboxylic acids and 1,5 dihydroxy-2,6-naphthalenedicarboxylic have been successfully synthesized and fully characterized. Interestingly, when 1,5 dihydroxy-2,6-naphthalenedicarboxylic was employed as organic linker, the hydroxyl groups were not involved in the coordination to the lanthanide clusters and therefore hydroxyl-functionalized lanthanides MOFs (AUBM-3) were obtained. The photophysical properties of both set of MOFs were studied and their sensing properties for toxic elements Pb(II), Cr(III), As(III), Cd(II), and Hg(II) and for paraquat were investigated. The hydroxyl-functionalized structures have shown to be promising luminescent sensory materials with high selectivity and sensitivity to mercury.

1. Introduction

Metal organic frameworks (MOFs), are a novel class of crystalline materials comprised of metal containing nodes, either a metal cation or metal clusters, and organic linkers connected via coordination bonds organized in a 3D network with uniform pore size [1,2]. MOFs have been an active area of research for the past two decades due to their rich chemistry and unique characteristics, including high surface area [3,4] which may exceed 10,000 m²/g, good mechanical and thermal stabilities [5,6], along with their possibility of being post-modified to target special applications [7]. MOFs offer great potential applications in several fields including catalysis [8–10], gas storage [11], magnetism [12,13], sensing, adsorption [14] and luminescence [15,16], production of metal nanoparticles [17], in addition to drug delivery [18], biomedical imaging [19], antimicrobial activity [20], dye sensitized solar cells [21], storage, encapsulation of dyes and polymer chains [22], also pH sensitive molecules [23,24]. Among these applications, sensing is one that has not been extensively investigated until recently. Consequently, available literature on such applications have reported the use of MOFs as sensors for explosives [25], chemical vapors [26], ions and small organic molecules [26]. Luminescent MOFs, particularly lanthanides MOFs (Ln-MOFs) can be considered one of the promising group of materials designed for

sensing. Ln-MOFs have distinctive luminescence properties, such as, high color purity, long-lived emission, great luminescence quantum yield, strident line emission and large Stokes shift [27]. In addition to their emissive property, Ln-MOFs are characterized by their tuned coordination geometry, stability and magnetic properties [28]. These features qualify Ln-MOFs as efficient platform for sensing. For the development of an efficient and successful MOF sensor, both a binding site and a strong luminophore are required, thus, the importance of choosing a suitable ligand. When designing Ln-MOF, the organic linker is important for the structure, yet it can serve as antennae for the lanthanide ions [29]. Thereby, in agreement with the hard-soft acid base model, carboxylated ligands are a good option in building Ln-MOFs since the lanthanide ions are hard acceptors, thus, favoring the coordination with hard carboxylate groups [30]. The luminescence of the lanthanides can be enhanced and intensified upon choosing aromatic carboxylic groups, the latter being fine luminescent chromophores. Therefore, to obtain an effective Ln-MOF sensor, a promising approach is to select a conjugated aromatic organic linker with Lewis base sites, where the luminescence can be improved along with a potential metal ion binding site [19].

On the other hand, heavy metals are naturally occurring elements, and exist in varying concentrations in all ecosystems. Their density is greater than 5 g cm⁻³ [31]. Human activities (e.g. industrial processes, mining)

* Corresponding author.

** Corresponding author.

E-mail addresses: dp03@aub.edu.lb (D. Patra), mohamad.hmadeh@aub.edu.lb (M. Hmadeh).

<https://doi.org/10.1016/j.jssc.2019.121031>

Received 15 July 2019; Received in revised form 16 October 2019; Accepted 27 October 2019

Available online 2 November 2019

0022-4596/© 2019 Elsevier Inc. All rights reserved.

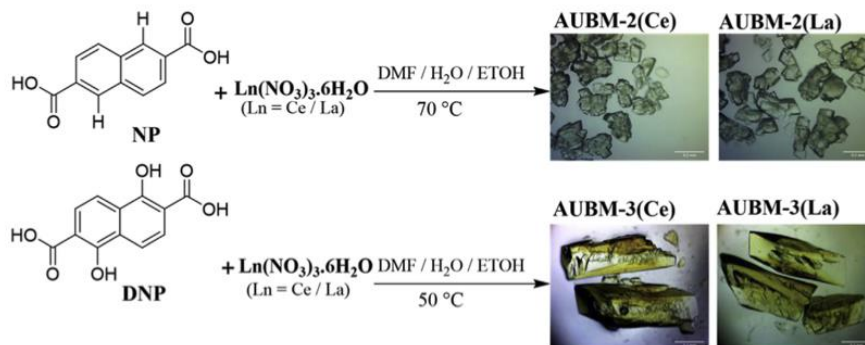
have drastically altered the biochemical cycles and balance of some heavy metals [32]. In low quantities, some heavy metals as iron, manganese, zinc and copper are nutritional necessities for a better life. On the other hand, heavy metals such as Cd, Pb, Cr, and Hg are poisonous and carcinogenic, even with trace amounts. Among various heavy metal ions, mercury is a very dangerous heavy metal that can induce many rigorous health problems such as damage to the nervous system and brain, kidney and the immune system [33]. Mercury exposure can provoke biochemical damage to tissues and genes via various mechanisms. It can interfere with the intracellular calcium homeostasis, alter membrane potential, disrupt protein synthesis, induce mitochondrial damage and cause lipid peroxidation [34]. With the mentioned risks that are related to mercury, a sensitive and selective detection of mercury can be considered as a priority. To detect mercury, several analytical techniques such as atomic absorption spectrometry [35], inductively coupled plasma atomic emission spectroscopy (ICP-AES) [36], gas chromatography-inductively coupled plasma-mass spectrometry [37], and atomic fluorescence spectroscopy (AFS) [38] are applied, however, these methods are often limited by the complex sample preparation, complicated devices and elevated cost [39]. Thus, it is of an importance to develop a non-demanding, sensitive and straightforward method for Hg²⁺ detection.

In this study, 2,6-naphthalenedicarboxylic acid (NP) and 1,5-dihydroxy-2,6-naphthalenedicarboxylic acid (DNP) (Scheme 1) were selected to react with lanthanides cations (La³⁺ and Ce³⁺) to produce new lanthanides MOF structures. After varying many experimental conditions such as reagent concentrations, solvent mixtures, temperature and pHs, we succeeded in synthesizing four lanthanides MOFs using both linkers (NP and DNP). Herein, the synthesis, structural investigations, thermal stability, luminescent and sensing properties of the four MOFs namely AUBM-2 (Ce) and AUBM-2(La) for MOFs with NP and AUBM-3(Ce) and AUBM-3(La) for MOFs with DNP, were examined and reported. The two sets of MOFs (AUBM-2 and AUBM-3) exhibited different fluorescent properties that were greatly dependent upon the linker properties. The linker did not channel the energy to excite the lanthanide metals, thus, the fluorescence emission spectra didn't show the lanthanide metals bands. Having an iso-structural nature that was evident in their photo-physical properties, Ce and La based MOFs were chosen to study their sensing behavior for different metal ions. Interestingly, AUBM-2 and AUBM-3 interacted with heavy metals and an intensive quenching of the AUBM-2 (Ce) luminescence in the presence of mercury was detected (K_{sv} value about 2000 M⁻¹). This high quenching effect was only evident in the case of mercury, therefore, the Ce MOF can be considered as a sensitive and selective detector for mercury ions.

2. Experimental section

2.1. Materials and methods

All reagents and solvents employed were commercially available



Scheme 1. Synthesis scheme of AUBM-2 and AUBM-3.

from Sigma-Aldrich and SUGAI chemical industry and used without further purification. The Infrared (IR) spectra were recorded on a FT-IR spectrometer Thermo-Nicolet working in the transmittance mode, in the 450-3950 cm⁻¹ range. Thermogravimetric Analysis (TGA) was performed with Netzsch TG 209 F1 Libra apparatus. Powder X-ray diffraction (PXRD) patterns were collected using a Bruker D8 advance X-ray diffractometer (Bruker AXS GmbH, Karlsruhe, Germany) at 40 kV, 40 mA (1600 W) using Cu K α radiation ($k = 1.5418 \text{ \AA}$). The absorption spectra were recorded at room temperature using JASCOV-570 UV-vis-NIR spectrophotometer. The steady state fluorescence measurements were recorded with resolution increment of 1 nm, slit 5 using a HORIBA Jobin Yvon Fluorolog-3 and the fluorescence program. The excitation source was 100 W xenon lamp, and the detector used was an R-928 operating at a voltage of 950 V. In order to regulate the temperature, a thermostat was coupled with the sample holder.

2.2. Synthesis of AUBM-2 and AUBM-3

Two novel Lanthanide MOFs were solvo-thermally synthesized by mixing 10 mg NP and 22 mg Ln(NO₃)₃·6H₂O (Ln = La and Ce) in a mixed solvent system DMF/H₂O/ETOH (10:1:1) at 70 °C in a closed cap vial for 72 h, large crystals were obtained (yield 76% based on NP ligand). Taking the DNP organic linker as a starting material along with the same previously mentioned metal salts, additional two new lanthanide MOFs were prepared in the same solvent mixture in an open cap at 50 °C for 3 days (yield 80% based on DNP ligand). The single crystals obtained were insoluble in DMF and acetone. Elemental analysis: calculated (%): [AUBM-2(Ce)]; C 46.67; H 3.39; Ce 24.20; N 3.63; O 22.10; [AUBM-2(La)] C 46.77; H 3.40; La 24.04; N 3.64; O 22.15; found (%): [AUBM-2(Ce)]; C 46.98; H 3.32; Ce 24.05; N 3.41; O 22.83; [AUBM-2(La)] C 47.47; H 3.42; La 24.36; N 3.78; O 23.42. FT-IR (KBr, $\nu = 3500\text{-}500 \text{ cm}^{-1}$): 3425(w), 1560(m), 1398(s), 1199(w), 1103(w), 800(m), 439(w). [AUBM-3(Ce)]; C 45.65; H 4.35; Ce 16.14; N 8.07; O 25.80; [AUBM-2(La)]; C 44.26; H 3.10; La 21.33; N 4.30; O 27.02; found (%): [AUBM-3(Ce)]; C 45.98; H 4.02; Ce 17.15; N 7.87; O 25.94; [AUBM-3(La)] C 45.25; H 3.31; La 22.14; N 4.13; O 26.42. FT-IR (KBr, $\nu = 3500\text{-}500 \text{ cm}^{-1}$): 2939(w), 1597(m), 1413(s), 1272(s), 1191(m), 889(w), 793(s), 668(w), 432(w).

3. Results and discussion

3.1. Description of crystal structures

Analysis of X-ray diffraction data: Single X ray diffraction data collected from the single crystals obtained from the NP revealed that the two AUBM-2 are isostructural frameworks, these MOFs crystallize in a triclinic P-1 space group and cell parameters of ($a = 12.524(6) \text{ \AA}$, $b = 12.570(6) \text{ \AA}$, $c = 16.507(7) \text{ \AA}$; $\alpha = 81.716(9)^\circ$, $\beta = 76.618(8)^\circ$, $\gamma = 60.47(2)^\circ$) with empirical formulas C₄₅ H₃₉ Ce₂ N₃ O₁₆ and C₄₅ H₃₉

$\text{La}_2\text{N}_3\text{O}_{16}$ for AUBM-2(Ce) and AUBM-3(La) respectively. Each metal (Ce and La) is coordinated to 5 NP ligands and each of the ligands is coordinated to 2 metal centers to form an extended porous framework. The lanthanides cations are nine-coordinated to oxygen atoms to form a distorted monocapped square antiprism. The two adjacent metal centers are sharing one of the edges. In the coordination sphere, two of the 9 oxygens are from solvent molecules (DMF and water), the rest are five monodentate carboxylate groups, one chelating carboxylate group and one monodentate carboxylate group of NP ligand (Fig. 1). The M–O bond lengths and O–M–O bond angles for the coordination spheres are within the ranges of 2.381–2.659 Å and 68.35–147.6° respectively. (See supporting information for more details Tables S1–S4). The structure represent 1D pore channels with dimension of about $8 \times 10 \text{ \AA}^2$ which is defined by the distances of the binuclear unit viewed along z axis. Nevertheless, the solvent molecules coordinated to the lanthanides centre limit the accessibility to these pores. Finally, it can be seen that adjacent NP linkers represent π - π interactions with distances of around 3.6 Å (see Fig. 1).

To introduce new coordination units within the organic backbone and to decrease the number of coordinating solvent on the metal clusters, the DNP linker was employed for the MOF synthesis. This linker incorporates OH groups in ortho positions that could potentially participate in the coordination of the lanthanides and hence the chemical stability of the framework would be enhanced. Crystals with different shapes and colors were obtained for Ce and La. SXR analysis of the two crystals showed 2 isostructural MOFs namely (AUBM-3) with the same topology but different from (AUBM-2). Interestingly, the OH groups in DNP, were not involved in the coordination of the Lanthanide cations. The obtained MOFs crystallize in a triclinic P-1 space group and cell parameters of ($a = 12.4869(15) \text{ \AA}$, $b = 12.5950(15) \text{ \AA}$, $c = 13.7583(17) \text{ \AA}$, $\alpha = 112.060(2)^\circ$, $\beta = 104.848(2)^\circ$, $\gamma = 102.417(2)^\circ$) with empirical formulas $\text{C}_{66}\text{H}_{75}\text{Ce}_2\text{N}_{10}\text{O}_{28}$ and $\text{C}_{24}\text{H}_{20}\text{La}_2\text{N}_2\text{O}_{11}$ for AUBM-3(Ce) and AUBM-3(La) respectively. The cluster is composed of 2 cations that are coordinated to 6 ligands to form the network. The lanthanides cations are nine coordinated to O atoms to form monocapped square antiprism that are sharing one of the edges. 2 solvents molecules (DMF and water) are also involved in the coordination spheres of the cations, the remaining are from the DNP linkers. The M–O bond lengths and O–M–O bond angles for the coordination spheres are within the ranges of 2.46–2.57 Å and 51.168–145.6°. The structure of AUBM-3 represent an open framework with pore aperture of about $12 \times 23 \text{ \AA}^2$ which represents M-M distance across the diagonal of the pore along a direction (Fig. 1). Again,

these MOFs were stable in DMF and acetone but not in aqueous solution. Due to the low number of ligands coordinating to the metals, the thermal stability of this set of MOFs (AUBM-3) was even lower than the AUBM-2 as evidenced by the TGA plots recorded for these two MOFs. The hydroxyl groups are free and not involved in the coordination of lanthanide which leave them available to interact with guest molecules and ions (see Fig. 1 and Fig. S1). In order to assess this porosity, the N_2 isotherm was performed on the activated for AUBM-2(Ce) and AUBM-3(Ce) and the Brunauer–Emmett–Teller (BET) surface area was determined to be 82 m^2/g and 190 m^2/g respectively (Fig. S2).

3.2. Powder X-ray diffraction and thermal gravimetric analyses

To verify the phase purity of the newly synthesized MOFs, the powder X-ray diffraction (PXRD) patterns were recorded and compared to the simulated patterns. As shown in Fig. S3 the diffraction peaks of the as-synthesized AUBM-2 and AUBM-3 are in agreement with the simulated data confirming the phase purity of the MOFs.

Thermal gravimetric analyses (TGA) of both series of lanthanide MOFs were carried between 30 and 1000 °C. The thermal profiles corresponding to AUBM-3(Ce) and AUBM-3(La) were analogous due to the isostructural character. A weight loss of 10% was obtained in the range of 77–140 °C corresponding to the loss of DMF molecules. The major mass loss of 30% occurred at 200 °C and is attributed to the decomposition of the organic framework and the discharge of the organic linker. The remaining residues are mainly the corresponding metal oxides. Similarly, the weight loss of AUBM-2 of both Ce and La-MOF was alike as a result of the isostructural nature. Compared to AUBM-3 MOFs this set showed a better thermal stability with the major weight loss (35%) corresponding to the burning of the framework occurred at 552 °C. Between 111 and 200 °C there is a 20% weight loss that is linked to the loss of the coordinated DMF molecules. The final residues are that of respective metal oxides Fig. S4.

3.3. FTIR spectral analysis

The FTIR spectrum of the synthesized AUBM-2 is shown in Fig. S5A. The spectrum indicates an up-field shift in the carbonyl stretches 1682 to 1682, 1659, 1650 and 1661 cm^{-1} for AUBM-2(La) and AUBM-2(Ce). Regarding AUBM-3, the two C=O groups for the ligand displays an up-field shifts from 1599 and 1656 to 1596 and 1653 cm^{-1} respectively for AUBM-3(La). Similar up-field shifts were observed for AUBM-3(Ce).

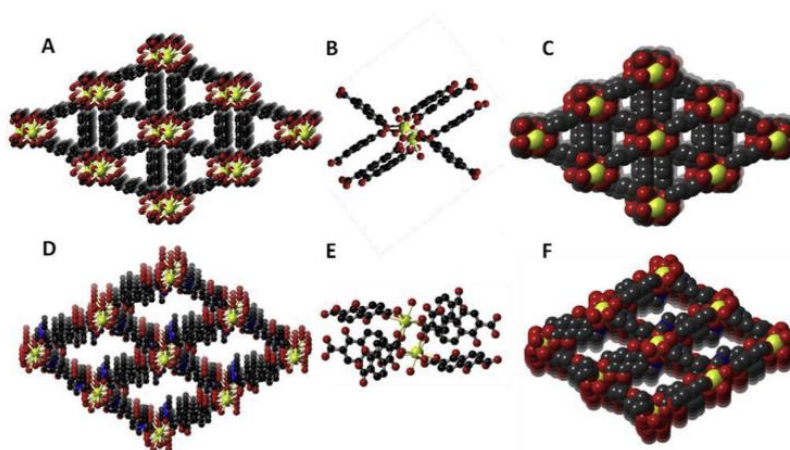


Fig. 1. Crystal structures of AUBM-2(Ce) (A), coordination mode in the cluster of AUBM-2 (B), space filling representation of AUBM-2 (C). Crystal structure of AUBM-3(Ce) (D), The coordination mode in AUBM-3 (E), space filling representation of AUBM-3 (F). Where Ce: yellow, O: red, N: blue, C: grey. (For interpretation of the references to color in this figure legend, the reader is referred to the Web version of this article.)

The characteristic broad band of the hydroxyl group within the solids were detected between 3200 and 3550 cm^{-1} designating the retention of the free OH groups as shown in Fig. S5B.

3.4. Photophysical properties

Luminescence in MOFs is usually dependent on the building components: the organic linker mainly conjugated one, metal ions or cluster and in few cases a result of adsorbed guest molecules that include to the emission. Organic linkers characterized by a rigid molecular backbone along with aromatic parts or extended π systems are commonly used in building MOFs. Luminescence generated mainly by the π electrons of the organic linker can be either linker based fluorescence or ligand-to-ligand charge transfer (LLCT) [28]. The photophysical properties of the linker are affected by the later arrangement in the framework thus resulting in different photoemission compared to that of the free form. In lanthanide MOFs, metal centered luminescence is dominant when an efficient intersystem crossing occurs between the organic linker and the metal. Linkers that allow the delivery of the excitation energy from their triplet excited states to the emissive states of the lanthanides result in the metal sensitization and the characteristic emission of the lanthanide metal is observed [28]. The photophysical properties of the synthesized MOFs and their linkers were investigated using UV-visible and fluorescence spectroscopy.

3.4.1. UV-vis spectroscopic measurements

The MOF crystals were washed and sonicated with DMF to have a homogeneous suspension and absorbance spectra were measured at room temperature. The isostructural property of AUBM-3 was reflected in the UV absorbance. In Fig. S6B, the absorbance spectrum of the organic linker shows an absorbance maximum at 346 nm in addition to another absorption peak at 296 nm . This is similar to one expects for NP linker. However, AUBM-2 shows an absorption maximum at 294 nm and a relatively weak absorption band at 420 nm . The changes in the absorption spectrum of the linker can be linked to the coordination between the organic linker and the metal ion in the framework. As for the DNP linker, the maximum absorbance is observed at 370 nm , with two other minor peaks similar to that of the NP linker at 314 and 297 nm . This red shift in the absorption spectrum of the DNP linker is a result of the presence of the hydroxyl groups which may further boost the conjugation in the parent ligand molecule and possibly form hydrogen bond with solvent molecules. The absorption spectra of AUBM-3 were similar with two maxima recorded at 399 nm and 300 nm along with shoulder bands at $370\text{--}380\text{ nm}$ Fig. S6A. This further shift in the absorption spectra is induced by the linker interaction in the organic framework. A deeper study of the absorption spectra of the linkers along with the MOFs where

the metal ions was cerium or lanthanum was performed. The UV-visible spectra were measured at different concentrations of the latter species Fig. S7 (A and B). Furthermore, it is clear from the figures that there was no change in the shape of the spectrum of both MOFs and the linkers at varying concentrations.

3.4.2. Fluorescence spectroscopic study

The washed MOFs and the dissolved linkers were excited at several wavelengths and the fluorescence spectra were measured at various concentrations in DMF at 298 K . As presented in Figs. S8A and S9A, at first the DNP linker alone was excited at three different wavelengths, such as at 300 , 370 and 400 nm at various concentrations. When excited at 370 and 400 nm , there is a significant red shift in the emission spectra from 436 nm to 500 nm along with a change in the shape of the emission spectra upon increasing the concentration of the linker. When excited at 300 nm , at higher concentration there is less red shift than the previously noted with the emission maximum shifting from 436 to 460 nm . This change at higher concentration is most likely caused by the formation of dimers or aggregates of the linkers. A similar outcome is also found for the NP linker with a red shift from 377 nm to 400 nm when excited at 300 nm given in Fig. S8. Those changes that are also observed when excited at 370 nm and 400 nm are a result of the aggregation free linker molecules at higher concentration.

The MOF crystals were diluted in DMF and the fluorescence spectra were measured at three different excitation wavelengths with varying concentrations of the MOFs in DMF. As shown in Figs. S8C and S9C, when excited at 300 nm , AUBM-3(Ce) gave a maximum fluorescence intensity centered at 436 nm , with another emission peak at 358 nm . Upon an excitation at 370 nm and 400 nm , AUBM-3(Ce) showed close emission spectra with the maximum emission occurring in both excitation conditions around 438 nm . Similar results were obtained for AUBM-3(La) Figs. S8D and S9D thus, it can be concluded that the lanthanide metal doesn't affect the emission properties, at least the photophysical behavior of the MOFs. However, when compared to the free linker, at high concentrations the new species emitting at higher concentrations is no longer evident when the linker is incorporated within the framework. Thus, the interaction between the metal and the linker hinders the interaction between the organic linker themselves. Moreover, when excited at 300 nm , the linker does not show a peak at 358 nm thus this outcome in the MOFs is an impact of the new arrangements and interactions the organic linker undergoes within the MOF. The fluorescence spectrum of AUBM-2(Ce) exhibited a maximum emission at 375 nm when excited at 300 nm (Figs. S8 and S9). When excited at 370 nm , this emission shifted to 415 nm . This suggests that there are two chromophores, which absorb and emit in two different wavelength regions. One of them primarily absorbs $\sim 290\text{--}300\text{ nm}$ and emits at $\sim 350\text{--}370\text{ nm}$

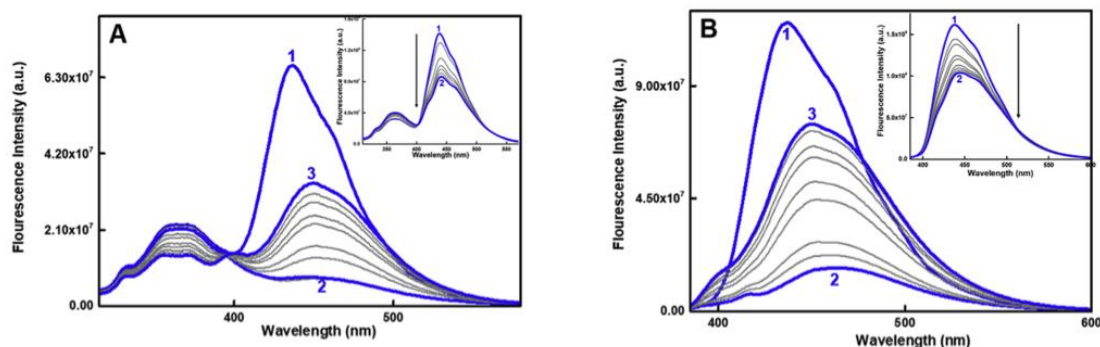


Fig. 2. Fluorescence spectra of the AUBM-3(Ce) excited at 300 nm (A) and 370 nm (B) in the presence of lead ions, where (1) $[\text{Pb}^{2+}] = 0.00\text{ }\mu\text{M}$, (2) $[\text{Pb}^{2+}] = 0.014\text{ }\mu\text{M}$, and (3) $[\text{Pb}^{2+}] = 0.189\text{ }\mu\text{M}$. Inset (A) and (B) fluorescence spectra of AUBM-3(Ce) at 300 nm , 370 nm respectively Where (1) $[\text{Pb}^{2+}] = 0.00\text{ }\mu\text{M}$, (2) $[\text{Pb}^{2+}] = 0.009\text{ }\mu\text{M}$.

whereas the other species absorbs at $\sim 360\text{--}400$ nm and emits at $\sim 400\text{--}450$ nm. However, there is also possibility of energy transfer such as FRET from species one to two, which influence the fluorescence spectral behavior [40].

3.5. Metal sensing

To study the ability of the synthesized lanthanides MOFs (AUBM-2 and AUBM-3) to detect and sense heavy metal ions, the MOFs were suspended in DMF and the heavy metal ion solution prepared in DMF were added in increasing concentrations to the MOF sample. The sensing potentials of the lanthanide's MOFs were tested with five ions (e.g. lead, cadmium, arsenic, mercury and chromium). From each set, samples were excited at two different wavelengths, 300 and 370 nm aiming to target two different fluorescent species present in MOFs. The outcome did not differ when the metal (La or Ce) was changed, thus, the interaction and sensing using cerium will only be reported and discussed here.

3.5.1. Interaction of lead ions with AUBM-2(Ce) and AUBM-3(Ce)

Fig. S10A and 2A show fluorescence spectra of AUBM-2(Ce) and AUBM-3(Ce) respectively, with increasing concentrations of lead ion upon exciting at 300 nm. For the AUBM-2(Ce), with increasing concentrations of the Pb^{2+} ion, there is an increase in the fluorescence intensity at 374 nm, whereas in case of AUBM-3(Ce) addition of 5 μL of the Pb ion stock (8.3 μM) red shifted the emission maximum from 436 nm (in the

absence of Pb^{2+}) to 452 nm with seven folds decrease in the fluorescence intensity Fig. 2A. As it can be seen in the inset of Fig. 2A, this quenching was monitored gradually by using a 5 times diluted stock solution of Pb ions. Further increase in Pb^{2+} concentration increased the fluorescence intensity centered at 452 nm. Nevertheless, the overall fluorescence intensity at 452 nm was still less than that in the absence of Pb^{2+} ion. This observation could be due to the fact that binding of Pb^{2+} ion with hydroxyl group of the linker forms a completely new complex with an emission peak at 452 nm and the population of this complex increased with increase in concentration of Pb^{2+} ion in solution, thus, boosting fluorescence intensity at 452 nm. This indicates that at low concentration of Pb^{2+} ion (below 0.014 μM), a quenching of the fluorescence peak at 452 nm was observed, however, at higher Pb^{2+} concentrations, an enhancement of the MOF fluorescence centered at the same peak was obtained.

A minor emission peak at 365 nm is also relevant at 300 nm excitation for AUBM-3(Ce), which was quenched with lead concentration. The quenching rate was calculated from the Stern Volmer plot with a Ksv value of 747 M^{-1} Fig. S11. This quenching was absent in the AUBM-2(Ce). When excited at 370 nm, as shown in Fig. S10B, the fluorescence of AUBM-2(Ce) at 436 nm decreased with increasing concentration of lead ions. Similarly, for AUBM-3(Ce), the increase in the lead concentrations quenched the fluorescence emission at 451 nm along with a red shift in the emission maximum, which was identical to that obtained at 300 nm excitation. Similar data were obtained for the AUBM-3(La)

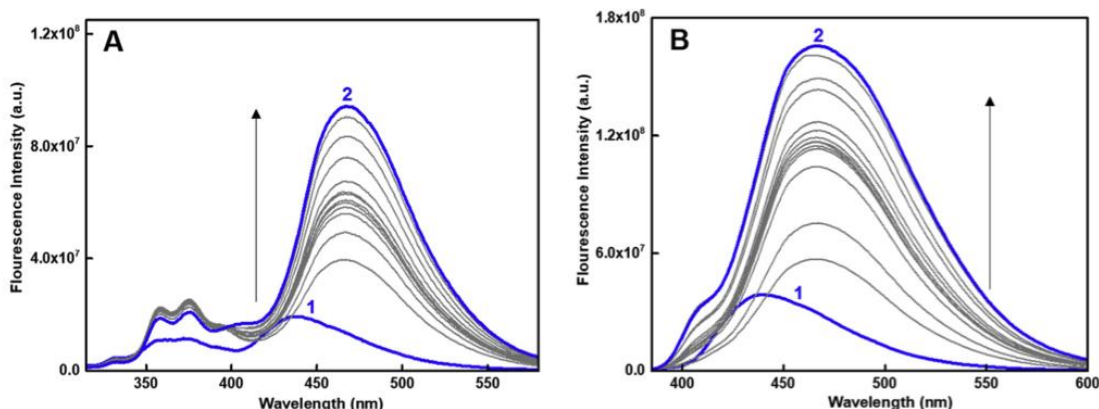


Fig. 3. Fluorescence spectra of the AUBM-3(Ce) excited at 300 nm (A) and 370 nm, (B) in the presence of chromium, where (1) $[\text{Cr}^{3+}] = 0.00\ \mu\text{M}$, (2) $[\text{Cr}^{3+}] = 0.215\ \mu\text{M}$.

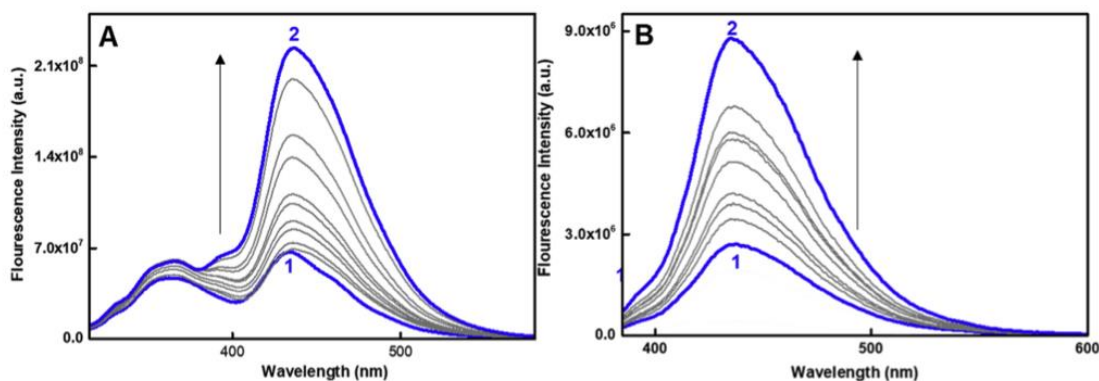


Fig. 4. Fluorescence spectra of the AUBM-2(Ce) excited at 300 nm (A) and 370 nm (B) in the presence of arsenic ions, where (1) $[\text{As}^{3+}] = 0.00\ \mu\text{M}$, (2) $[\text{As}^{3+}] = 0.123\ \mu\text{M}$.

when excited at 300 nm, with a higher Ksv value 908 M^{-1} . Thus, the best approach to estimate the presence of lead would be to monitor the emission at 365 nm for the AUBM-3(Ce) excited at 300 nm.

3.5.2. Interaction of chromium ions with AUBM-2(Ce) and AUBM-3(Ce)

As shown in Fig. S12 (A and B), interaction between AUBM-2(Ce) with increasing concentration of chromium ion resulted in an enhancement in fluorescence intensity while exciting at 300 nm or 370 nm. However, the emission maximum was affected to a small extent in the presence of the chromium ions and the emission was more sensitive to the chromium ions at 300 nm excitation than that induced when excited

at 370 nm. In the case of AUBM-3(Ce) (see Fig. 3), enhancement of fluorescence intensity was also observed with increasing concentrations of the chromium ions except that a 30 nm red shift in the emission maximum (from 437 to 467) was observed. Similar, results were obtained at 370 nm. This indicates chromium may not specifically bind the hydroxyl group of the ligand rather it gets buried/adsorbed on the MOFs which influence the fluorescence properties of MOFs.

3.5.3. Interaction of arsenic and cadmium ions with AUBM-2(Ce) and AUBM-3(Ce)

AUBM-2(Ce) and AUBM-3(Ce) were excited at 300 nm and 370 nm in

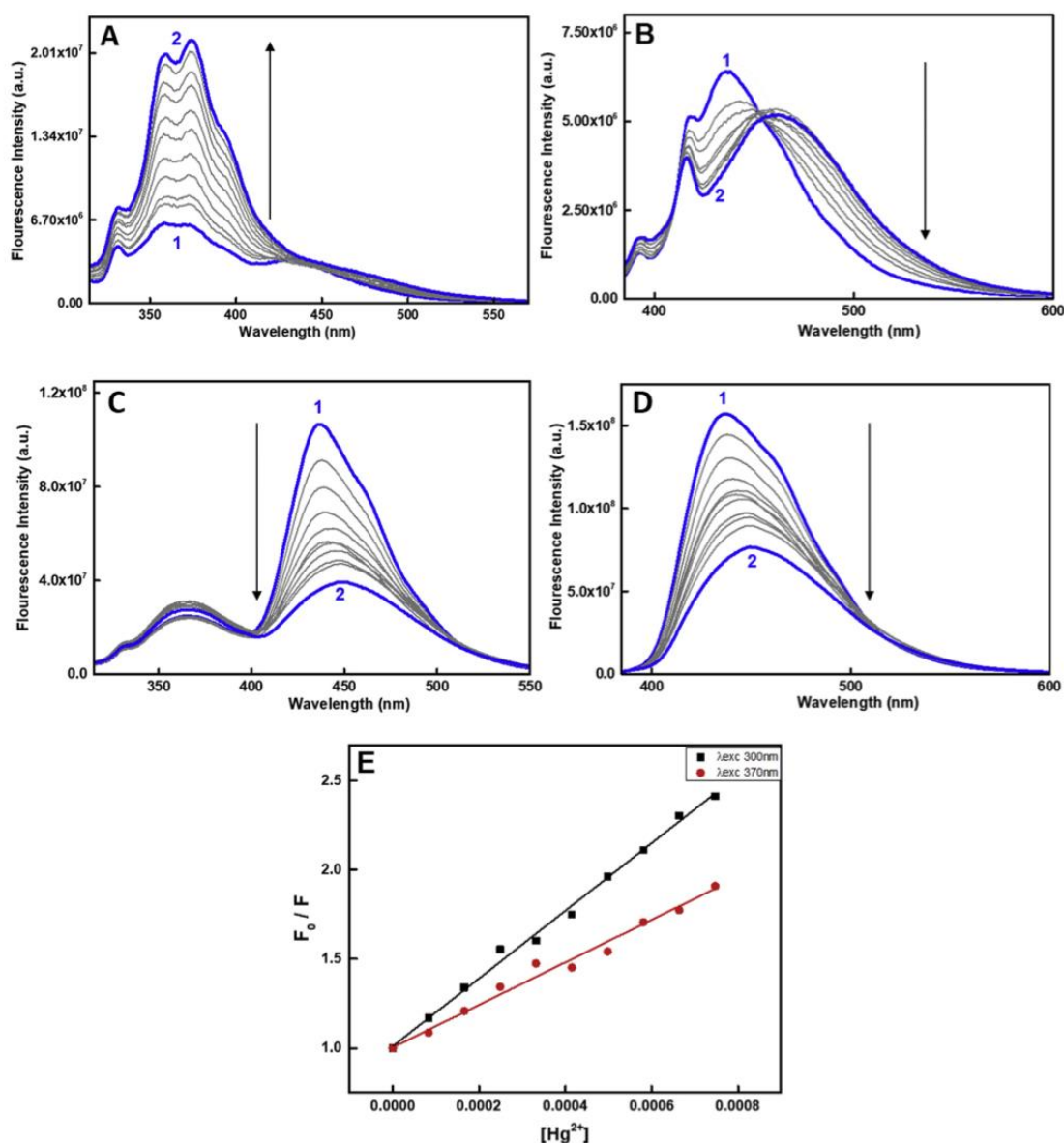


Fig. 5. Fluorescence spectra of the AUBM-2(Ce) excited at 300 nm (A) and 370 nm (B) in the presence of mercury ions in addition to the spectra obtained for AUBM-3(Ce) under same condition upon exciting at 300 nm (C) and 370 nm (D). Stern-volmer Plots for AUBM-3(Ce) in the presence of mercury ions (E), where (1) $[\text{Hg}^{2+}] = 0.00 \mu\text{M}$, (2) $[\text{Hg}^{2+}] = 0.136 \mu\text{M}$.

the presence of increasing concentrations of metal ions (arsenic and cadmium). As shown in Fig. 4 and S13, the increase in the concentration of the arsenic ion resulted in mild enhancement in the fluorescence emission without any changes or shifts in the spectrum as in the case of the previously discussed metals. Similar results were also obtained with cadmium (Fig. S14). Indeed, the strongest enhancement after the addition of Cd ions to a total concentration of 830 μM by a factor of 21 was observed for AUBM-2(Ce) when excited at 370 nm compared to a 1.5-fold of enhancement when excited at 300 nm. The fluorescence was enhanced by 3 times when AUBM-3(Ce) was excited at 300 nm and about 2-fold increase in the emission when AUBM-3(Ce) was excited at 370 nm (Fig. S14).

3.5.4. Interaction of mercury ions with AUBM-2(Ce) and AUBM-3(Ce)

The interaction between the cerium-based MOFs and the mercury metal ions was the most interesting data among the five heavy metals. When excited at 300 nm in the presence of increasing concentrations of Hg ions, the emission intensity of the AUBM-2(Ce) at 375 nm was enhanced. However, when excited at 370 nm under the same conditions, the Hg ions induced a quenching effect with a gradual red shift in the emission spectra (~30 nm red shift) with increasing concentrations of mercury. In the case of AUBM-3(Ce), the fluorescence emission after excitation at 300 nm was quenched with a small red shift of the emission maximum at higher concentration of mercury ions (Fig. 5). The corresponding Ksv value obtained from the Stern-volmer plot was remarkable, ~1899.6 M^{-1} . Contrary to its behavior in the presence of lead, the emission intensity at 364 nm was enhanced. When excited at 370 nm, the maximum emission at 436 nm was quenched in addition to a red shift of 14 nm in the emission maximum. The Ksv value was estimated as 1192.6 M^{-1} less than that was found when exciting at 300 nm. This quenching is linked to the hydroxyl groups of the DNP. As shown from the single XRD data, the OH groups are not involved in the coordination of the lanthanide clusters of AUBM-3 thus providing an interaction site with metals. The recyclability of AUBM-3(Ce) was investigated by washing the resulting MOF with acetone several times. Interestingly, the recovered MOF crystals were efficiently used to detect and sense mercury ions with no obvious change in the fluorescence spectrum (Fig. S15). Also, the regeneration of the crystals doesn't affect the crystallinity of the MOF structure as evidenced in the PXRD pattern (Fig. S16).

Based on the reported experimental data, the newly fluorescent synthesized MOFs showed interaction with heavy metals however, it showed selective quenching for Hg at 436 nm after excitation at 300 nm and selective quenching in the case of the lead metal ions in the 365 nm emission after excitation at 300 nm. Similarly, the fluorescence of AUBM-3(Ce) at 370 nm excitation was quenched only in the case of mercury ions. The quenching effect induced by the mercury metals was appreciable with Ksv values of 1899.6 and 1192.6 M^{-1} after exciting at 300 nm and 370 nm respectively, a table of comparison of different luminescent MOFs for detecting Hg(II) is given in the SI (Table S5). And shows that the detection limit of Hg and the calculated Ksv are within the range of the best reported MOF structures. Thus, we can say that the AUBM-3(Ce) can be used as a selective sensor for mercury among 5 common heavy metals. The selectivity towards metal ions of four different kinds of MOFs under investigation is summarized in Fig. 6.

Two different trends were observed during luminescent titrations. As found in the UV-visible absorption and fluorescence spectra, both the MOFs (AUBM-2 and AUBM-3) have two absorbing/emitting species depending on the excitation wavelengths (300 or 370 nm). In literature where MOFs were employed in metal sensing applications [41], several explanations regarding their luminescence behavior (quenching or enhancement) have been investigated such as: (i) the ion exchange between the guest ions and the metal ions of the MOF clusters [42,43], (ii) the resonance energy transfer [44], (iii) the collapse of the framework upon addition of the metal ions [45] and (iv) the weak interactions between guest metal ions and the functional group within the organic linkers of the MOFs [46]. In order to understand the mechanism behind

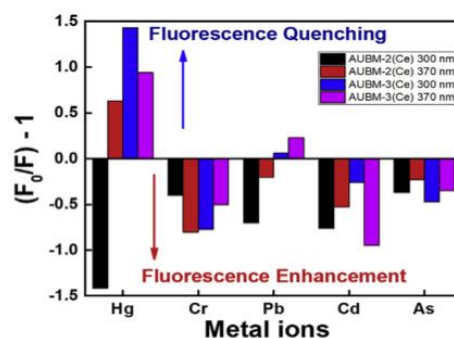
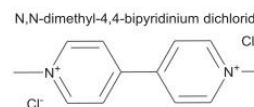


Fig. 6. Influence of fluorescence change of different MOFs in the presence of various metal ions during optical sensing. The concentrations of metal ions were fixed at 8.33 mM. F_0 and F are the fluorescence intensity in the absence and presence of metal ion, respectively.

the spectral changes observed throughout the sensing studies in the present case, several experiments were performed. The PXRD patterns of the MOFs after sensing were recorded and showed that the crystallinity of the frameworks was not affected (Fig. S16), which exclude the collapse of the framework upon addition of the cations. Furthermore, no Pb, As, Cd or Hg was observed in the SEM-EDX analysis performed on the MOFs crystals after sensing (Fig. S17). Finally, UV-vis absorption spectra for the metal ions and AUBM-3(Ce) were recorded, a spectral overlap between the absorption spectrum of Hg^{2+} solution and the absorption peaks of AUBM-3(Ce) was observed (Fig. S20) while other metal ion solutions do not. This overlapping suggests that the fluorescence quenching by Hg^{2+} ion may be attributed to the absorption competition at the excitation wavelength (300 and 370 nm) between Hg^{2+} solution and AUBM-3(Ce). Moreover, as shown from the single XRD data, the OH groups are not involved in the coordination of the lanthanide clusters of AUBM-3 which provides an interaction site for the metal ions during sensing. A significant red shift (30 nm) was observed by increasing Hg^{2+} concentration for AUBM-2(Ce) at 370 nm, which may be caused by the solvatochromism effect [47] suggesting a more polar environment for the chromophore in the presence of Hg^{2+} . This can be possible only when some exposed free carboxylate units from the organic linkers resulted from the defects in the crystals (a very common phenomenon in MOFs structures) or free OH group could be involved in the weak interactions with the studied cations. Such adsorption enhances the fluorescence of the MOFs, as observed for AUBM-2(Ce) at 300 nm and other metal ions.

3.6. Paraquat sensing



Paraquat (Methyl viologen, MV) is a poisonous bipyridinium compound used as contact herbicide. Paraquat binds strongly to soil particles and tends to remain strongly bound for a long time in an inactive state, although it can also desorb again and become biologically active. Half-life in soil can be up to 20 years. Therefore, developing a sensing technique for such compound is particularly interesting. Since our AUBM-2 and AUBM-3 incorporate Naphthalene based linkers which are known to be electron rich species, we believe that these MOFs could interact with electron acceptor units such as viologen. Indeed, charge transfer (CT) complexes have been reported based on the interaction between DNP or NP units and MV^{2+} [48]. Interestingly, the fluorescence of AUBM-2(La) and AUBM-2(Ce) were completely quenched (see Fig. 7)

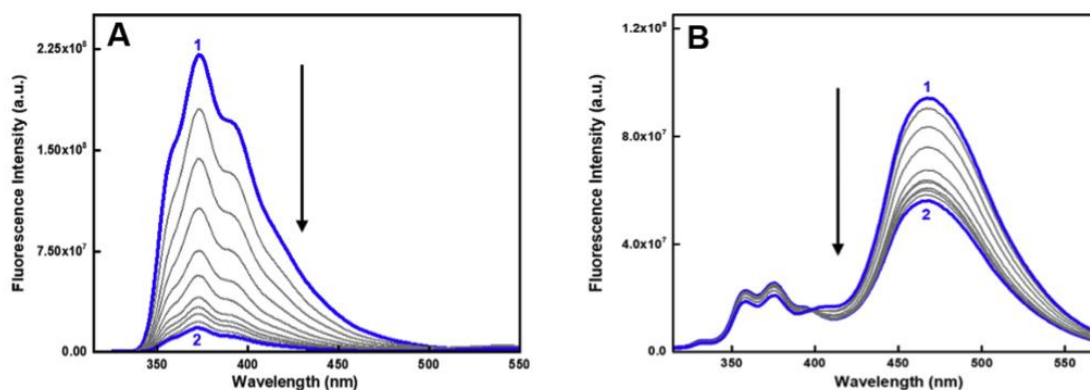


Fig. 7. Fluorescence spectra of the AUBM-2(La) (A) and AUBM-2(Ce) (B) excited at 300 nm, where (1) $[MV^{2+}] = 0.0$ mg/mL and (2) $[MV^{2+}] = 50$ mg/mL at ambient temperature.

upon addition of MV^{2+} with K_{sv} values $21 M^{-1}$ and $9 M^{-1}$ respectively. Especially, AUBM-2 (La) fluorescence was remarkably quenched as shown in Fig. 7A. It can be noted that initially till 80 mM of MV^{2+} , the quenching rate for F_0/F of AUBM-3(La) vs. $[MV^{2+}]$ was linear as given in inset of Fig. S18 and it obeys Stern-Volmer equation with a K_{sv} value $\sim 21 M^{-1}$. However, as the concentration increased, the trend showed an upward curvature. Since AUBM-2(La) can form charge transfer complex with MV^{2+} , it is expected that initially the quenching rate follows a dynamic quenching mechanism till ~ 20 mM and afterwards at higher concentration of MV^{2+} both static and dynamic quenching mechanisms are operative giving an upward curvature in the Stern-Volmer plot. It was found that this quenching trend of AUBM-2(La) by MV^{2+} continued till up to 50 mg/mL, thus, it can be useful for the determination of MV^{2+} in environmental samples.

4. Conclusion

Four highly luminescent lanthanides-based metal-organic frameworks were successfully synthesized using solvothermal processes. All the four lanthanides-based MOFs were thoroughly characterized using single crystal and powder X-ray diffraction, TGA, IR, UV-Vis, fluorescence studies. The luminescent properties of the all four MOFs were explored and their ability for heavy metal sensing such as Pb (II), Cr (III), As (III), Cd (II) and Hg (II) and paraquat were tested in solution. Among the tested MOFs, cerium-based MOF (AUBM-3(Ce)) was found to be highly selective for mercury sensing in solution. Highly selective and stable luminescent lanthanides design and synthesis using our current knowledge for selective detection of heavy metal in aqueous solution is underway in our laboratory.

The structural information of AUBM-2(La), AUBM-2(Ce), AUBM-3(La) and AUBM-3(Ce) are available free of charge from the Cambridge Crystallographic Data Centre under the reference numbers: CCDC 1,841,240, CCDC 1,841,235, CCDC 1,841,198 and CCDC 1,841,199, respectively.

Declaration of competing interest

The authors declare that they have no known competing financial interests or personal relationships that could have appeared to influence the work reported in this paper.

Acknowledgment

This research work was funded by the American University of Beirut (AUB) University Research Board (URB) and the Lebanese National

Council for Scientific Research (#103496 and #103487) and the Masri Institute (#103214). The authors would like to thank the personnel at the Kamal A. Shair Central Research Science Laboratory (CRSL) for their support and assistance. T.P. and L.L. thank NYUAD for its generous support for the research program at NYUAD and the authors also thank the Core Technology Platforms at NYUAD.

Appendix A. Supplementary data

Supplementary data to this article can be found online at <https://doi.org/10.1016/j.jssc.2019.121031>.

References

- [1] S. Yuan, L. Feng, K. Wang, J. Pang, M. Bosch, C. Lollar, Y. Sun, J. Qin, X. Yang, P. Zhang, Q. Wang, L. Zou, Y. Zhang, L. Zhang, Y. Fang, J. Li, H.-C. Zhou, *Adv. Mater.* 30 (2018) 1704303.
- [2] Q.-G. Zhai, X. Bu, X. Zhao, D.-S. Li, P. Feng, *Acc. Chem. Res.* 50 (2017) 407–417.
- [3] H. Furukawa, K.E. Cordova, M. O'Keefe, O.M. Yaghi, *Science* 341 (2013) 1230444.
- [4] D. Saliba, M. Ammar, M. Rammal, M. Al-Ghoul, M. Hmadeh, *J. Am. Chem. Soc.* 140 (2018) 1812–1823.
- [5] H. Wu, T. Yildirim, W. Zhou, *J. Phys. Chem. Lett.* 4 (2013) 925–930.
- [6] K.S. Park, Z. Ni, A.P. Côté, J.Y. Choi, R. Huang, F.J. Uribe-Romo, H.K. Chae, M. O'Keefe, O.M. Yaghi, *Proc. Natl. Acad. Sci. U.S.A.* 103 (2006) 10186–10191.
- [7] K.K. Tanabe, S.M. Cohen, *Chem. Soc. Rev.* 40 (2011) 498–519.
- [8] S. Horike, M. Dincă, K. Tamaki, J.R. Long, *J. Am. Chem. Soc.* 130 (2008) 5854–5855.
- [9] D.-S. Liu, Z.-J. Qiu, X. Fu, Y.-Z. Liu, P. Ding, Y.-X. Zhu, Y. Sui, *J. Solid State Chem.* 278 (2019) 120879.
- [10] D.-S. Liu, Y. Sui, G.-M. Ye, H.-y. Wang, J.-Q. Liu, W.-T. Chen, *J. Solid State Chem.* 263 (2018) 182–189.
- [11] R. Matsuda, R. Kitaura, S. Kitagawa, Y. Kubota, R.V. Belosludov, T.C. Kobayashi, H. Sakamoto, T. Chiiba, M. Takata, Y. Kawazoe, Y. Mita, *Nature* 436 (2005) 238–241.
- [12] P. Dechambenoit, J.R. Long, *Chem. Soc. Rev.* 40 (2011) 3249–3265.
- [13] W.-W. Xiong, E.U. Athresh, Y.T. Ng, J. Ding, T. Wu, Q. Zhang, *J. Am. Chem. Soc.* 135 (2013) 1256–1259.
- [14] H. Atallah, M. Elcheikh Mahmoud, A. Jelle, A. Lough, M. Hmadeh, *Dalton Trans.* 47 (2018) 799–806.
- [15] H.R. Moon, D.-W. Lim, M.P. Suh, *Chem. Soc. Rev.* 42 (2013) 1807–1824.
- [16] D.-S. Liu, Y. Sui, W.-T. Chen, P. Feng, *Cryst. Growth Des.* 15 (2015) 4020–4025.
- [17] P. Horcajada, R. Gref, T. Baati, P.K. Allan, G. Maurin, P. Couvreur, G. Férey, R.E. Morris, C. Serre, *Chem. Rev.* 112 (2012) 1232–1268.
- [18] S. Keskin, S. Kizilel, *Ind. Eng. Chem. Res.* 50 (2011) 1799–1812.
- [19] H. Deng, S. Grunder, K.E. Cordova, C. Valente, H. Furukawa, M. Hmadeh, F. Gandara, A.C. Whalley, Z. Liu, S. Asahina, H. Kazumori, M. O'Keefe, O. Terasaki, J.F. Stoddart, O.M. Yaghi, *Science* 336 (2012) 1018–1023.
- [20] B. Mortada, T.A. Matar, A. Sakaya, H. Atallah, Z. Kara Ali, P. Karam, M. Hmadeh, *Inorg. Chem.* 56 (2017) 4739–4744.
- [21] V. Nevruzoglu, S. Demir, G. Karaca, M. Tomakin, N. Bilgin, F. Yilmaz, *J. Mater. Chem.* 4 (2016) 7930–7935.
- [22] W.-W. Xiong, J. Miao, K. Ye, Y. Wang, B. Liu, Q. Zhang, *Angew. Chem. Int. Ed.* 54 (2015) 546–550.
- [23] Z. Moussa, M. Hmadeh, M.G. Abiad, O.H. Dib, D. Patra, *Food Chem.* 212 (2016) 485–494.

- [24] S.S. Nagarkar, B. Joarder, A.K. Chaudhari, S. Mukherjee, S.K. Ghosh, *Angew. Chem. Int. Ed.* 52 (2013) 2881–2885.
- [25] Z. Xie, L. Ma, K.E. deKrafft, A. Jin, W. Lin, *J. Am. Chem. Soc.* 132 (2010) 922–923.
- [26] P. Deria, J.E. Mondloch, O. Karagiari, W. Bury, J.T. Hupp, O.K. Farha, *Chem. Soc. Rev.* 43 (2014) 5896–5912.
- [27] B.V. Harbuzaru, A. Corma, F. Rey, P. Atienzar, J.L. Jordá, H. García, D. Ananias, L.D. Carlos, J. Rocha, *Angew. Chem. Int. Ed.* 47 (2008) 1080–1083.
- [28] H. Zhang, L. Zhou, J. Wei, Z. Li, P. Lin, S. Du, *J. Mater. Chem.* 22 (2012) 21210–21217.
- [29] J.-M. Zhou, W. Shi, N. Xu, P. Cheng, *Inorg. Chem.* 52 (2013) 8082–8090.
- [30] S.J. Hawkes, *J. Chem. Educ.* 74 (1997) 1374.
- [31] L. Pari, P. Murugavel, S.L. Sitasawad, K.S. Kumar, *Life Sci.* 80 (2007) 650–658.
- [32] K. Jomova, M. Valko, *Toxicology* 283 (2011) 65–87.
- [33] F. Zahir, S.J. Rizwi, S.K. Haq, R.H. Khan, *Environ. Toxicol. Pharmacol.* 20 (2005) 351–360.
- [34] L. Patrick, *Mercury Toxicity and Antioxidants: Part I: Role of Glutathione and Alpha-Lipoic Acid in the Treatment of Mercury Toxicity*, 2003.
- [35] H.N. Chou, C.A. Naleway, *Anal. Chem.* 56 (1984) 1737–1738.
- [36] A. Elkady, F. Abdelmonem, Highly Sensitive and Selective Spectrophotometric Detection of Trace Amounts of Hg 2+ in Environmental and Biological Samples Based on 2,4,7-Triamino-6-Phenylpteridine, 2013.
- [37] D. Karunasagar, J. Arunachalam, S. Gangadharan, *J. Anal. Atomic Spectrom.* 13 (1998) 679–682.
- [38] X.-P. Yan, X.-B. Yin, X.-W. He, Y. Jiang, *Anal. Chem.* 74 (2002) 2162–2166.
- [39] M. Rex, F.E. Hernandez, A.D. Campiglia, *Anal. Chem.* 78 (2006) 445–451.
- [40] J.W. Taraska, W.N. Zagotta, *Neuron* 66 (2010) 170–189.
- [41] M. Feng, P. Zhang, H.-C. Zhou, V.K. Sharma, *Chemosphere* 209 (2018) 783–800.
- [42] C.-X. Yang, H.-B. Ren, X.-P. Yan, *Anal. Chem.* 85 (2013) 7441–7446.
- [43] Y. Zhou, H.-H. Chen, B. Yan, *J. Mater. Chem.* 2 (2014) 13691–13697.
- [44] S. Pramanik, C. Zheng, X. Zhang, T.J. Emge, J. Li, *J. Am. Chem. Soc.* 133 (2011) 4153–4155.
- [45] X.-Y. Xu, B. Yan, *ACS Appl. Mater. Interfaces* 7 (2015) 721–729.
- [46] Q. Tang, S. Liu, Y. Liu, J. Miao, S. Li, L. Zhang, Z. Shi, Z. Zheng, *Inorg. Chem.* 52 (2013) 2799–2801.
- [47] A. Barba-Bon, A.M. Costero, S. Gil, M. Parra, J. Soto, R. Martínez-Máñez, F. Sancenón, *Chem. Commun.* 48 (2012) 3000–3002.
- [48] M. Hmadeh, A.C. Fahrenbach, S. Basu, A. Trabolsi, D. Benítez, H. Li, A.-M. Albrecht-Gary, M. Elhabiri, J.F. Stoddart, *Chem. Eur J.* 17 (2011) 6076–6087.

B. Supporting information: Sensing properties of two lanthanides-based metal organic framework

Supporting Information

Lanthanides Based Metal Organic Frameworks for Luminescence Sensing of Toxic Metal Ions

Mahmoud Elcheikh Mahmoud^a, Zeinab Moussa^a, Thirumurugan Prakasam,^b Liang Li, Mohamad G. Abiad,^c Digambara Patra^{a*}, Mohamad Hmadeh^{a*}

^aChemistry Department, American University of Beirut, PO Box 11-0236, Riad El Solh, Beirut 1107-2020, Lebanon

^bNew York University Abu Dhabi (NYUAD), Experimental Research Building, Building C1, Saadiyat Island, Abu Dhabi, UAE.

^cDepartment of Nutrition and Food Sciences, American University of Beirut, PO Box 11-0236, Riad El Solh, Beirut 1107-2020, Lebanon

*Corresponding Authors: E-mail: dp03@aub.edu.lb

*Corresponding Authors: E-mail: mohamad.hmadeh@aub.edu.lb

Table S1: Crystallographic data and structural refinement summary for **AUBM-2(Ce)**

| Compound | AUBM-2(Ce) |
|--|--|
| Empirical formula | C ₄₅ H ₃₉ Ce ₂ N ₃ O ₁₆ |
| Formula weight | 1158.03 |
| Crystal system | Triclinic |
| Space group | P -1 |
| a/ Å | 12.524(6) |
| b/ Å | 12.570(6) |
| c/ Å | 16.507(7) |
| V/Å ³ | 2198.3(18) |
| T/K | 173(2) |
| Dc/Mg m ⁻³ | 1.749 |
| Z | 2 |
| m(Mo-Kα)/mm ⁻¹ | 2.122 |
| No. unique data (R _{int}) | 11904 |
| Final R indices [I > 2σ(I)] ^a | R ₁ = 0.0680, wR ₂ = 0.1527 |
| R indices (all data) | R ₁ = 0.0992, wR ₂ = 0.1609 |

Table S2: Crystallographic data and structural refinement summary for **AUBM-2(La)**

| Compound | AUBM-2(La) |
|--|--|
| Empirical formula | C ₄₅ H ₃₉ La ₂ N ₃ O ₁₆ |
| Formula weight | 1155.61 |
| Crystal system | Triclinic |
| Space group | P -1 |
| a/ Å | 12.55(1) |
| b/ Å | 12.556(10) |
| c/ Å | 16.571(13) |
| V/Å ³ | 2200(3) |
| T/K | 173 |
| Dc/Mg m ⁻³ | 1.744 |
| Z | 2 |
| m(Mo-Kα)/mm ⁻¹ | 1.992 |
| No. unique data (Rint) | 11084 |
| Final R indices [<i>I</i> > 2 <i>s</i> (<i>I</i>)] _a | R ₁ = 0.1103, wR ₂ = 0.1367 |
| R indices (all data) | R ₁ = 0.0701, wR ₂ = 0.2093 |

Table S3: Crystallographic data and structural refinement summary for **AUBM-3(Ce)**

| Compound | AUBM-3(Ce) |
|--|---|
| Empirical formula | C ₆₆ H ₇₅ Ce ₂ N ₁₀ O ₂₈ |
| Formula weight | 1736.37 |
| Crystal system | Triclinic |
| Space group | P -1 |
| a/ Å | 12.4869(15) |
| b/ Å | 12.5950(15) |
| c/ Å | 13.7583(17) |
| V/Å ³ | 1817.7(4) |
| T/K | 100 |
| Dc/Mg m ⁻³ | 1.586 |
| Z | 1 |
| m(Mo-Kα)/mm ⁻¹ | 1.327 |
| No. unique data (Rint) | 9034 |
| Final R indices [<i>I</i> > 2 <i>s</i> (<i>I</i>)] _a | R ₁ = 0.0454, wR ₂ = 0.1205 |
| R indices (all data) | R ₁ = 0.0510, wR ₂ = 0.1250 |

Table S4: Crystallographic data and structural refinement summary for **AUBM-3(La)**

| Compound | AUBM-3(La) |
|--|---|
| Empirical formula | C ₂₄ H ₂₀ La N ₂ O ₁₁ |
| Formula weight | 615.33 |
| Crystal system | Triclinic |
| Space group | P -1 |
| a/ Å | 12.489(2) |
| b/ Å | 12.747(2) |
| c/ Å | 13.791(2) |
| V/Å ³ | 1881.5(5) |
| T/K | 173 |
| D _c /Mg m ⁻³ | 1.150 |
| Z | 2 |
| m(Mo-Kα)/mm ⁻¹ | 1.178 |
| No. unique data (<i>R</i> _{int}) | 9589 |
| Final <i>R</i> indices [<i>I</i> > 2σ(<i>I</i>)] _a | <i>R</i> ₁ = 0.0454, w <i>R</i> ₂ = 0.1205 |
| <i>R</i> indices (all data) | <i>R</i> ₁ = 0.0510, w <i>R</i> ₂ = 0.1250 |

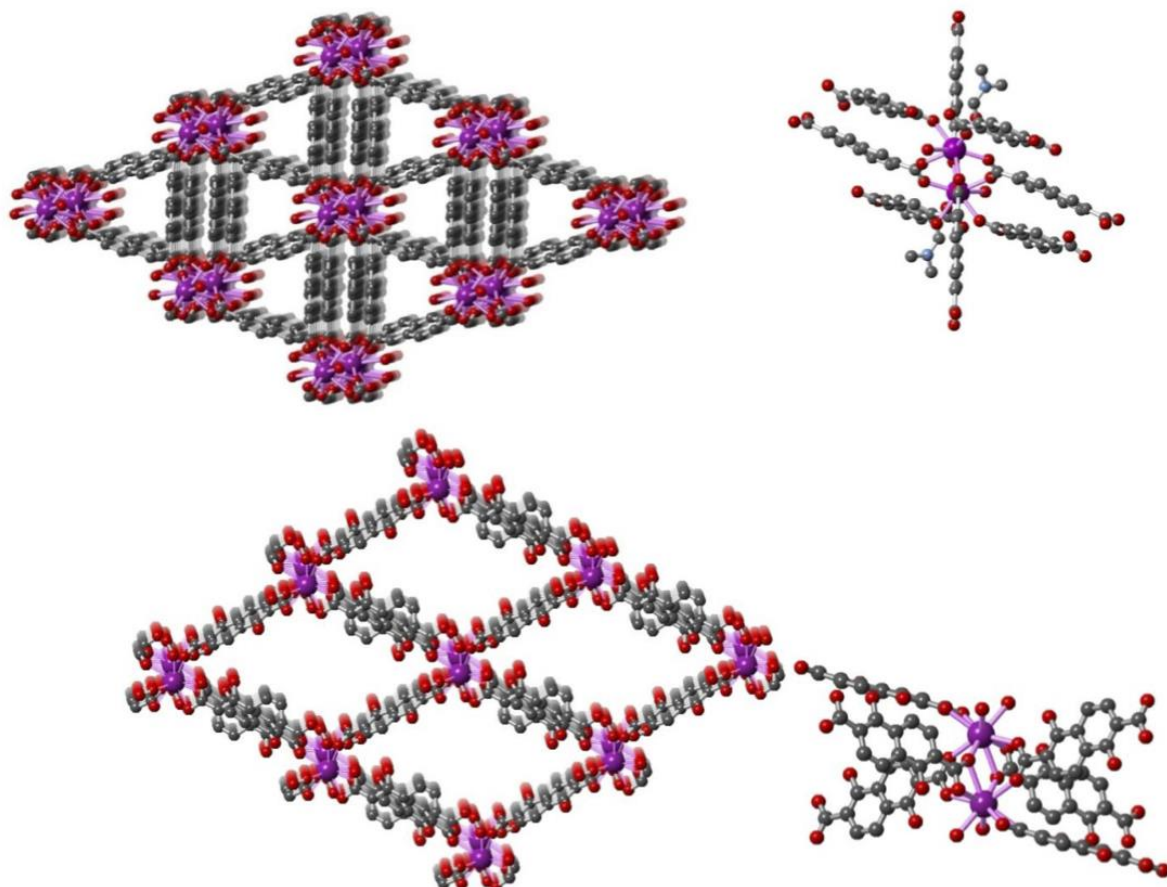


Figure S1. Crystal structures of AUBM-2(La) (top) and AUBM-3(La) (bottom); La: purple, O: red, N: blue, C: grey.

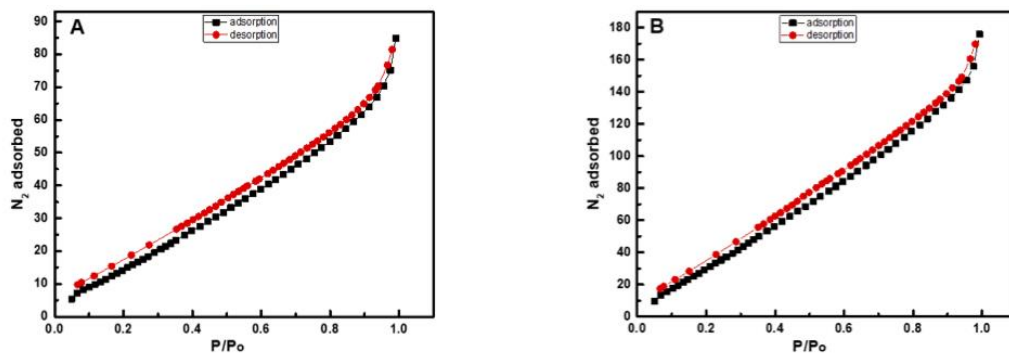


Figure S2. N₂ uptake by AUBM-2(Ce) (A) and AUBM-3(Ce) (B), BET surface area are calculated to be 82 and 190 m²/g for AUBM-2(Ce) and AUBM-3(Ce) respectively.

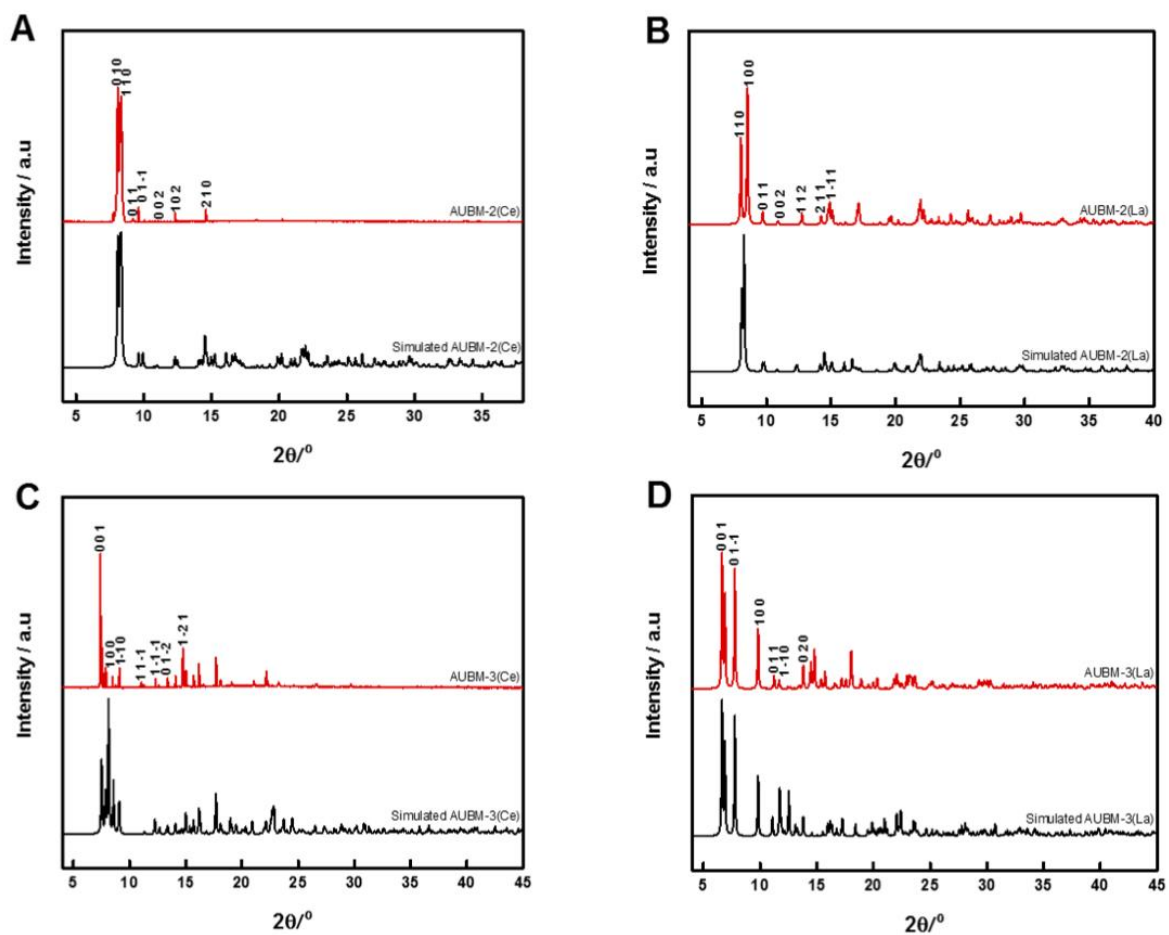


Figure S3. The Powder X-ray diffraction of different AUBM-2(Ce) (A), AUBM-2(La) (B), AUBM-3(Ce) (C), AUBM-3(La) (D).

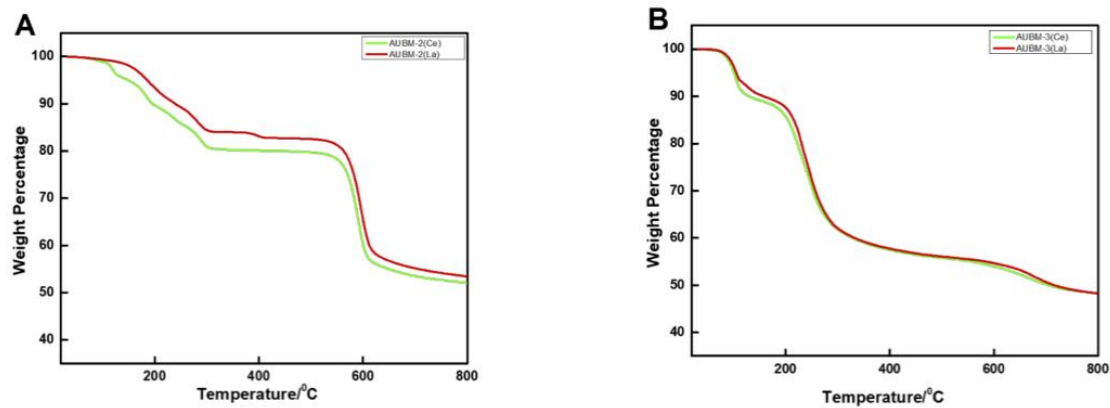


Figure S4. Thermal Gravimetric Analyses of different AUBM-2 (A) and AUBM-3 (B).

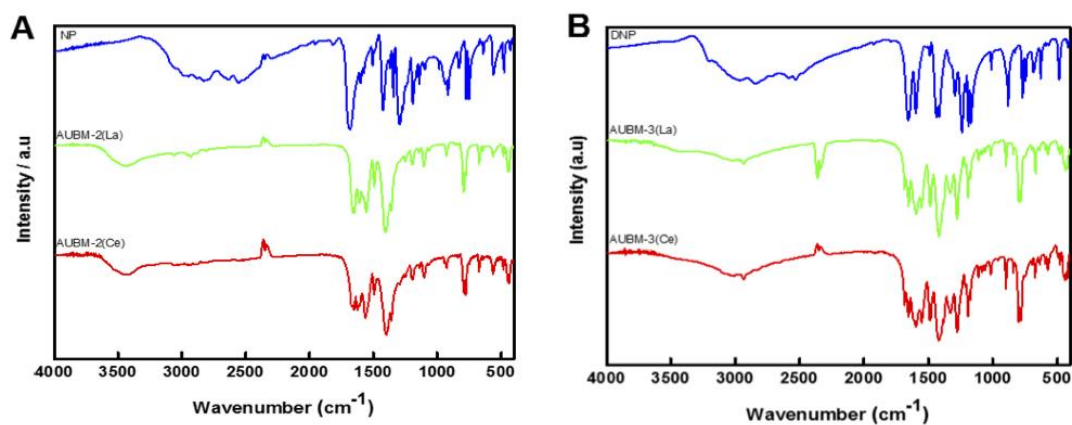


Figure S5. FTIR analysis for AUBM-2 (A) and AUBM-3 (B)

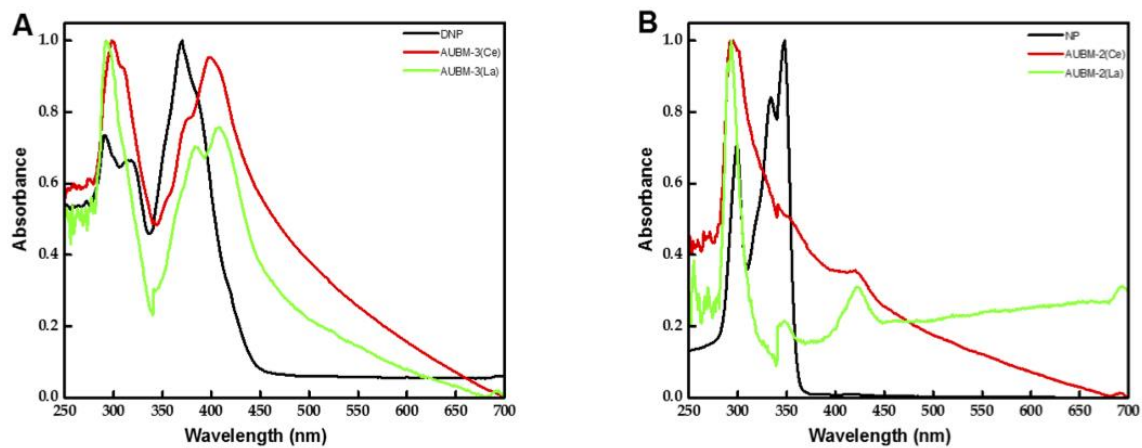


Figure S6. Absorption spectrum of the DNP linker and AUBM-3 MOFs (A) also for the NP linker and AUBM-2 MOFs (B).

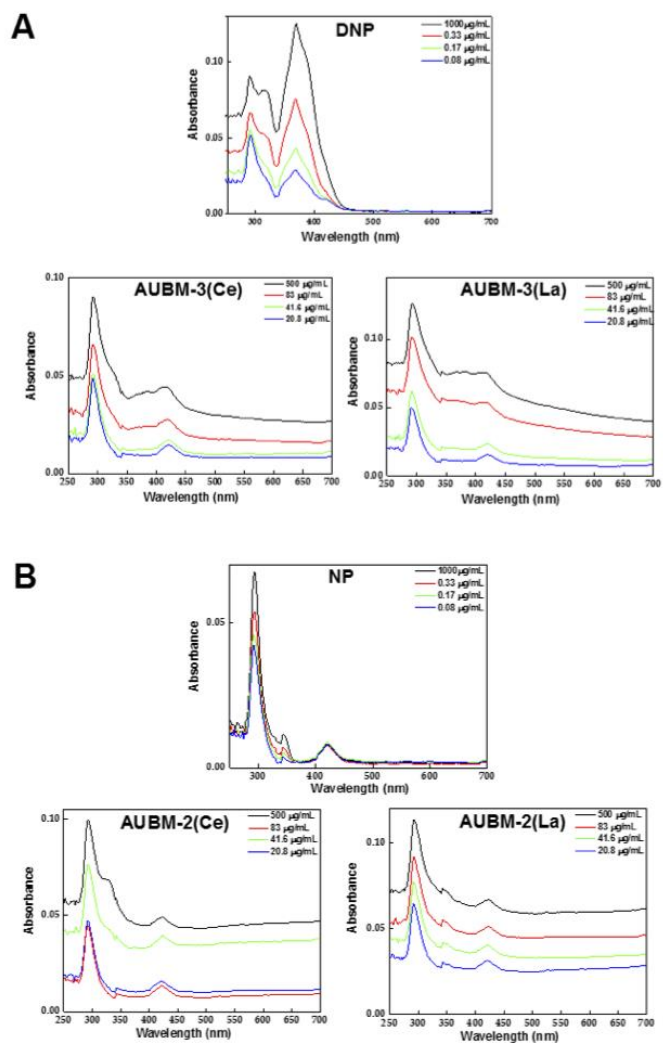


Figure S7. The absorbance measurements at different concentrations for the DNP linker and AUBM-3 (A), also NP linker and AUBM-2 (B).

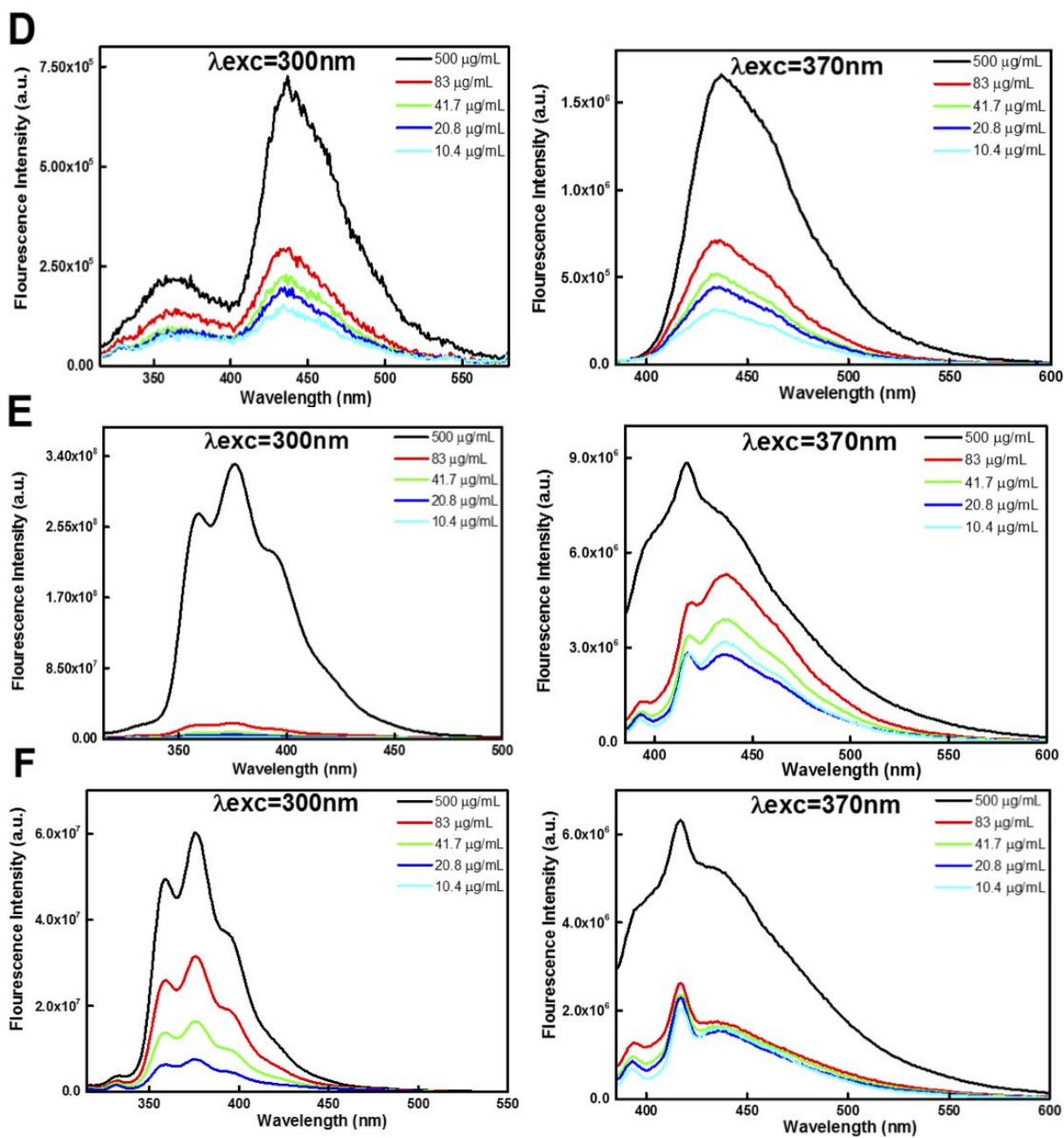


Figure S8. Fluorescence spectra for *DNP linker* (A), *NP linker* (B), *AUBM-3(Ce)* (C), *AUBM-3(La)* (D), *AUBM-2(Ce)* (E) and *AUBM-2(La)* (F) *AUBM-2(Ce)* excited at 300nm (left) and 370nm (right) in various concentrations.

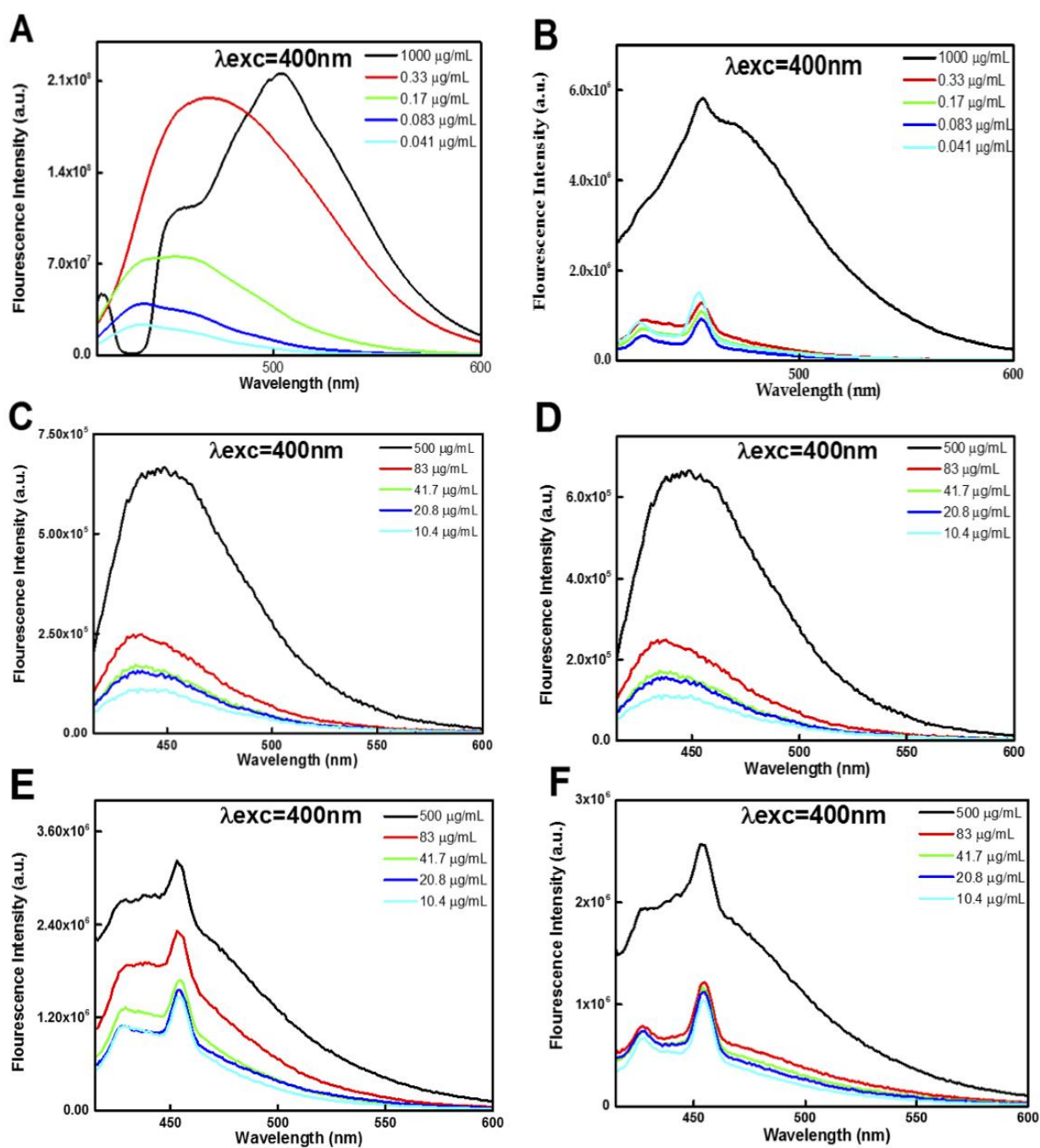


Figure S9. Fluorescence spectra for DNP linker (**A**), NP linker (**B**), AUBM-3(Ce) (**C**), AUBM-3(La) (**D**), AUBM-2(Ce) (**E**) and AUBM-2(La) (**F**) excited at 400nm in various concentrations.

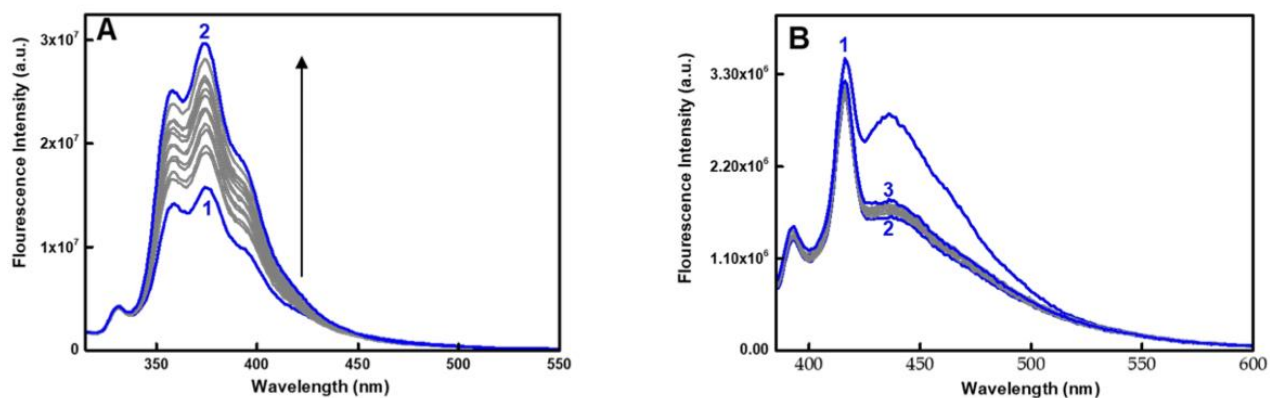


Figure S10. Fluorescence spectra of the AUBM-2(Ce) excited at 300nm (A) and 370nm (B) in the presence of lead ions. Where (1) $[\text{Pb}^{2+}] = 0.00 \mu\text{M}$, (2) $[\text{Pb}^{2+}] = 0.014 \mu\text{M}$, and (3) $[\text{Pb}^{2+}] = 0.189 \mu\text{M}$.

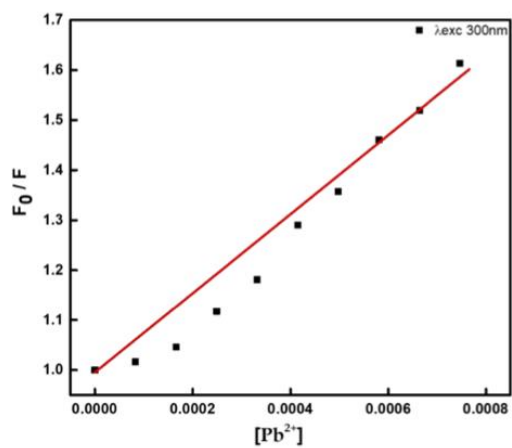


Figure S11. Stern-Volmer plot for the quenching of the AUBM-3(Ce) with lead ions.

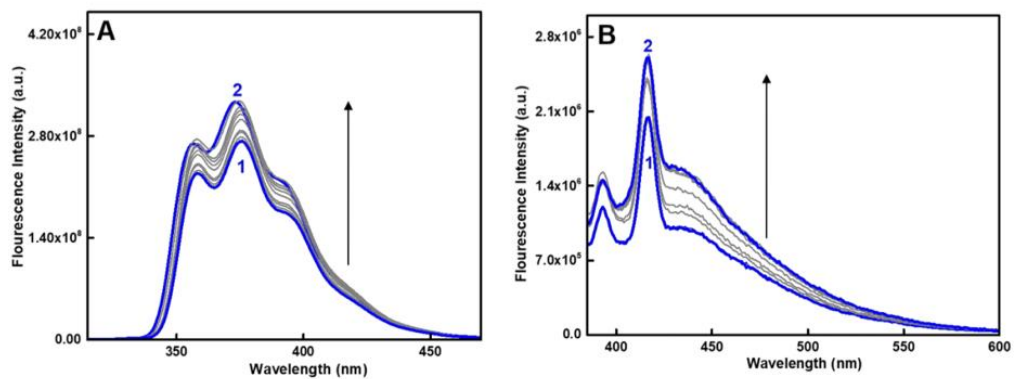


Figure S12. Fluorescence spectra of the AUBM-2(Ce) excited at 300 nm (A) and 370 nm (B) in the presence of chromium ions. Where (1) $[Cr^{4+}] = 0.00 \mu M$, (2) $[Cr^{4+}] = 0.215 \mu M$.

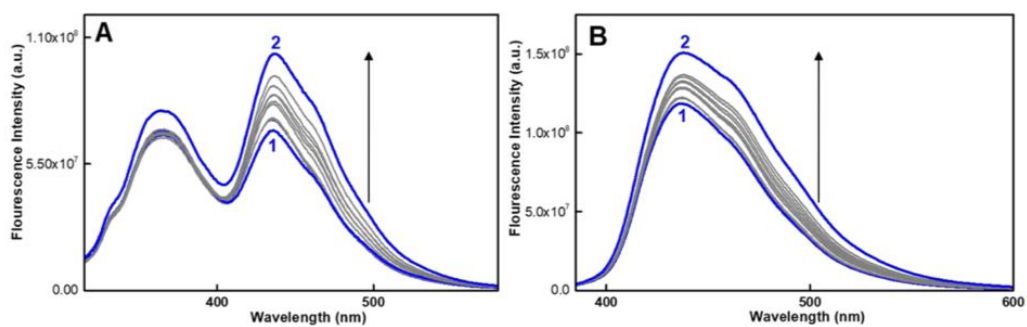


Figure S13. Fluorescence spectra of the AUBM-3(Ce) excited at 300nm (A) and 370nm (B) in the presence of arsenic ions. Where (1) $[As^{3+}] = 0.00 \mu M$, (2) $[As^{3+}] = 0.123 \mu M$.

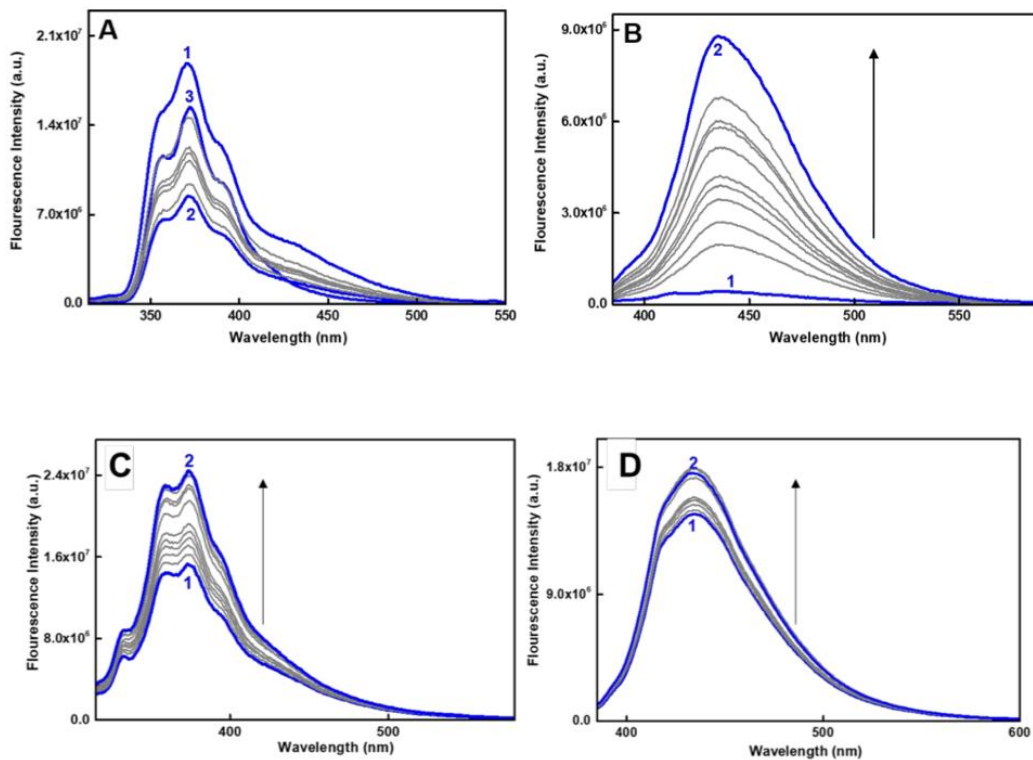


Figure S14. Fluorescence spectra of the AUBM-2(Ce) excited at 300 nm (A) and 370 nm (B) in the presence of cadmium ions. Where (1) $[Cd_{2+}] = 0.00 \mu M$, (2) $[Cd_{2+}] = 0.014 \mu M$, and (3) $[Cd_{2+}] = 0.136 \mu M$. Fluorescence spectra of the AUBM-3(Ce) excited at 300 nm (C) and 370 nm (D) in the presence of cadmium ions. Where (1) $[Cd_{2+}] = 0.00 \mu M$, (2) $[Cd_{2+}] = 0.136 \mu M$.

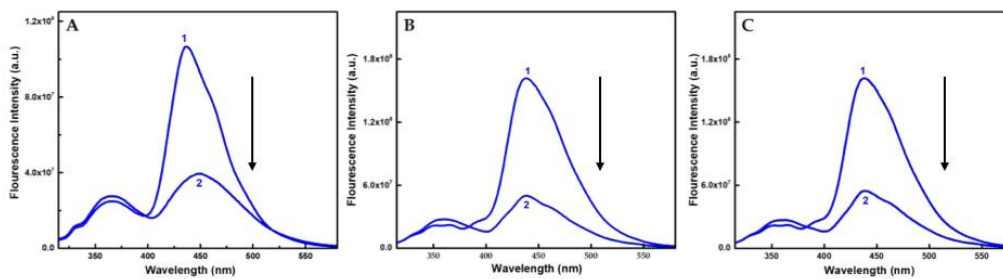


Figure S15: Fluorescence spectra of the AUBM-3(Ce) excited at 300nm (recycled three times via acetone washing) in the presence of mercury ions. Where (1) $[Hg_{2+}] = 0.00 \mu M$, (2) $[Hg_{2+}] = 0.136 \mu M$

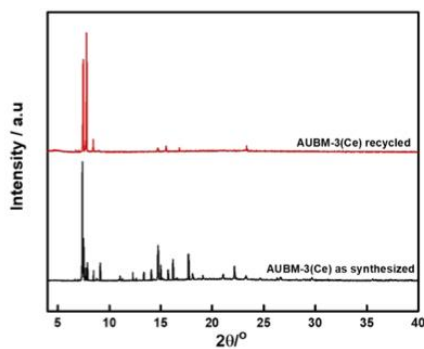
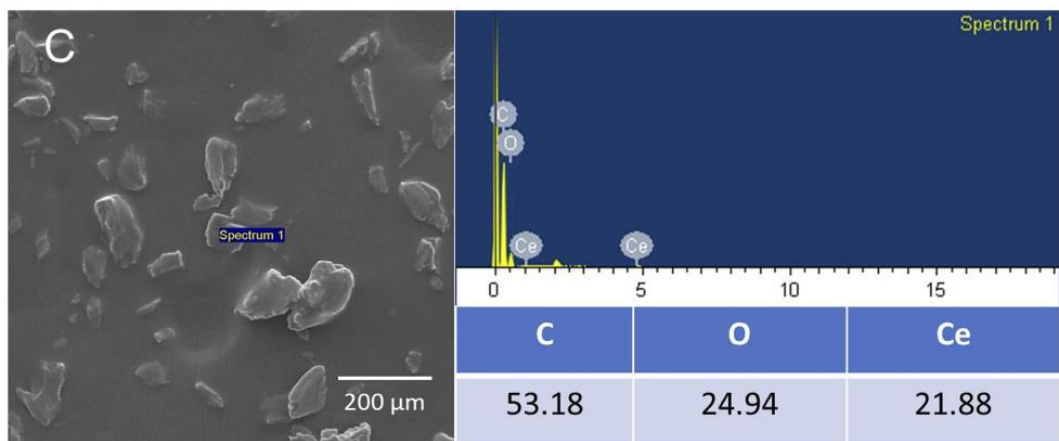
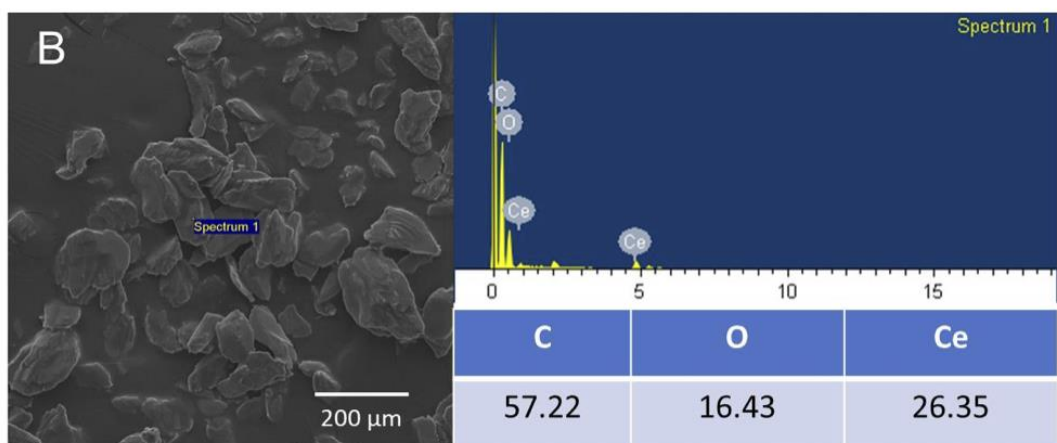
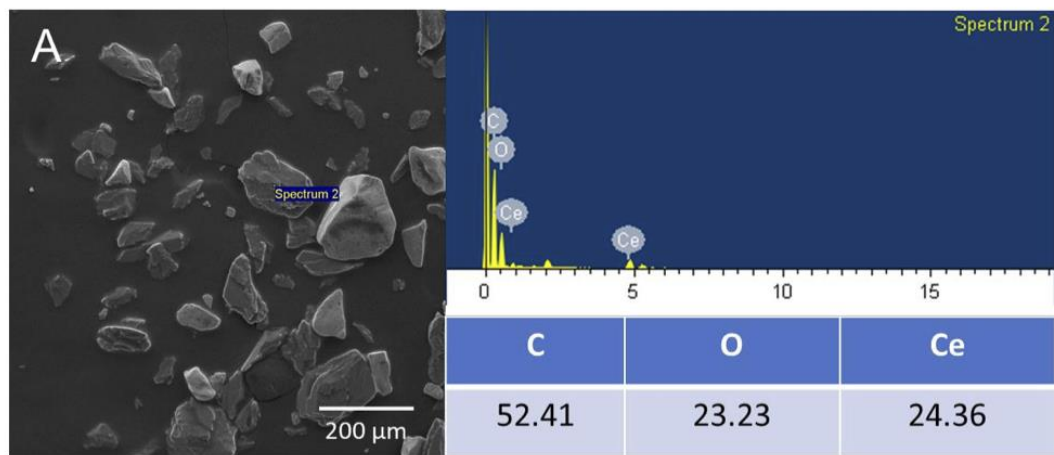


Figure S16: The Powder X-ray diffraction of AUBM-3(Ce) after three cycles.

Table S5: A comparison between luminescent MOFs for the detection of Hg metal ions

| <i>Luminescent MOFs</i> | <i>Analyte</i> | <i>Detection Limits (M)</i> | <i>K_{sv} value (M⁻¹)</i> | <i>Ref.</i> |
|---|------------------|------------------------------|--|------------------|
| [Zn(μ 2-1Hade)(μ 2-SO ₄)] | Hg ²⁺ | 7X10 ⁻⁸ | 7700 | [1] |
| TbTATAB | Hg ²⁺ | 4.4 X 10 ⁻⁹ | 4851 | [2] |
| PCN-224 | Hg ²⁺ | 6 X 10 ⁻⁹ | 640000 | [3] |
| UiO-66 | Hg ²⁺ | 5.2 X 10 ⁻¹⁰ | - | [4] |
| UiO-66-NH ₂ | Hg ²⁺ | 1.76 X 10 ⁻⁸ | - | [5] |
| Bio-MOF-1 | Hg ²⁺ | 5.3 X 10 ⁻¹³ | - | [6] |
| Eu/IPA | Hg ²⁺ | 2 X 10 ⁻⁹ | - | [7] |
| AUBM-3(Ce) | Hg ²⁺ | 1.8 X 10⁻⁹ | 1899.6 | This work |



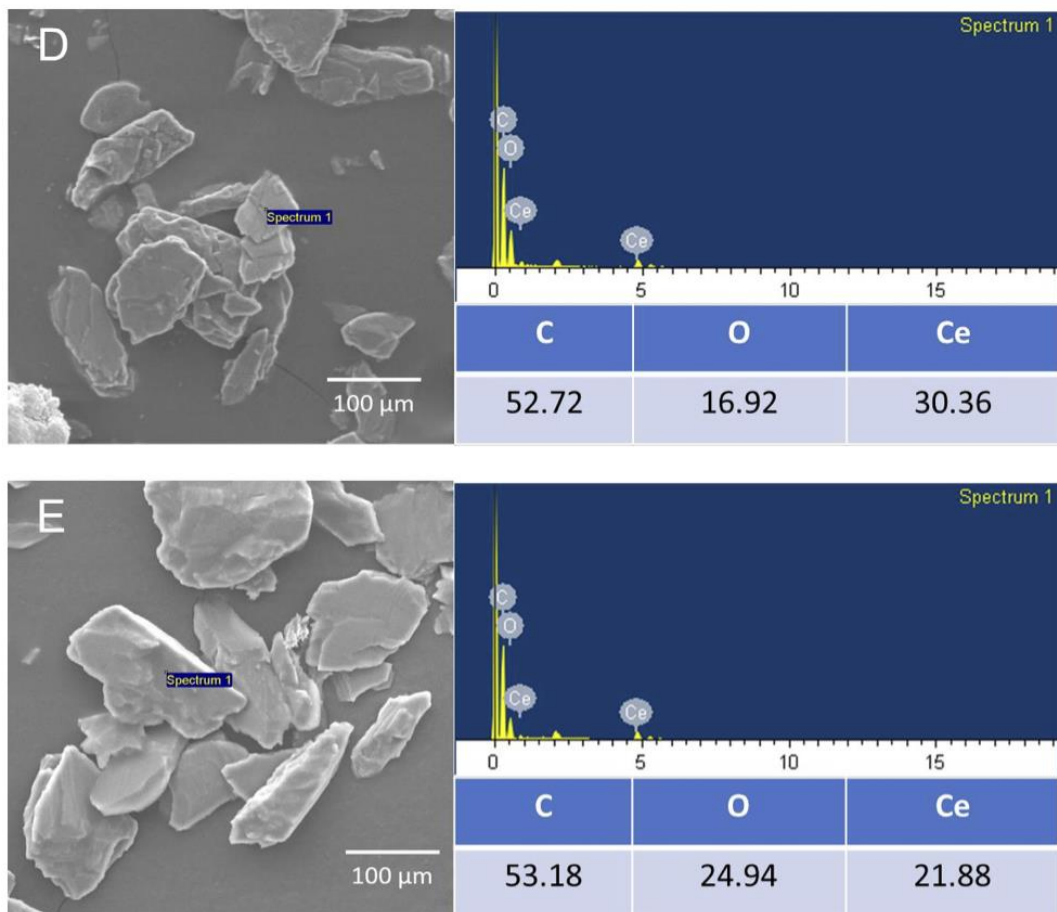


Figure S17: SEM-EDX analysis for AUBM-3(Ce) after treatment with As(III) (A), Hg(II) (B), Pb(II) (C), Cr(III) (D), and Cd(II) (E).

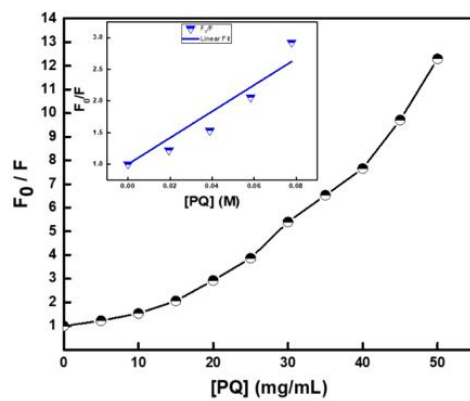


Figure S18. Stern-Volmer Plot for AUBM-2(La) in the presence of paraquat.

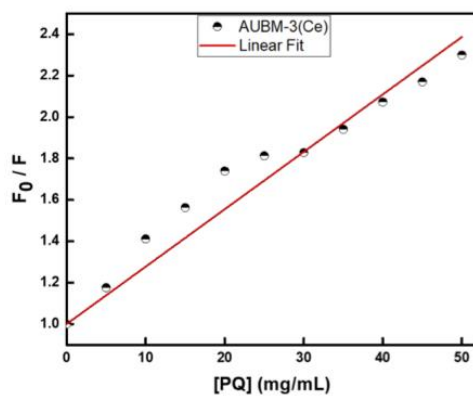


Figure S19. Stern-Volmer Plot for AUBM-2(Ce) in the presence of paraquat.

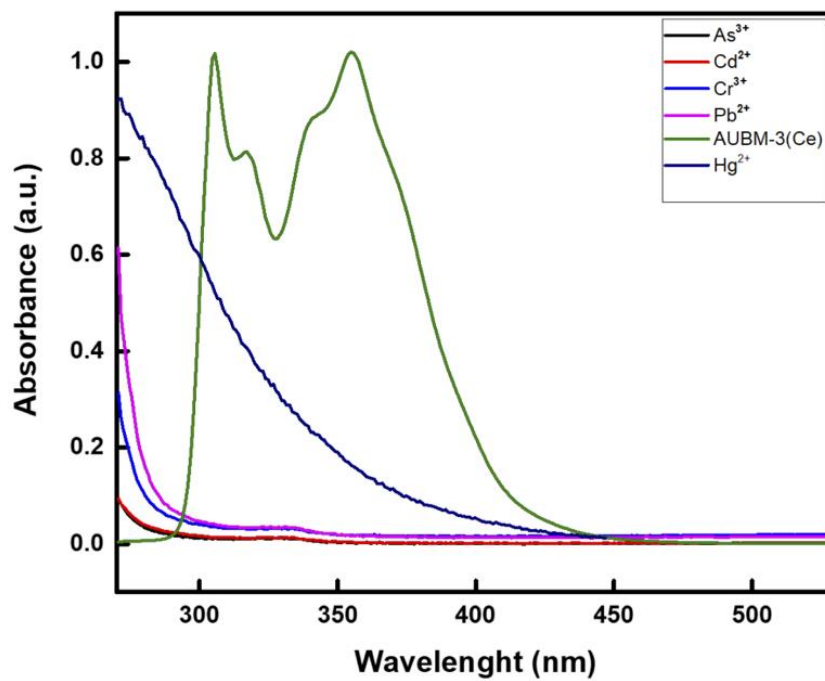


Figure S20. UV-Vis adsorption spectra of solutions of different metal ions (10^{-6} mol/L) compared to the absorbance spectrum of AUBM-3(Ce) dispersed in DMF.

References.

- [1] X. Cui, K. Chen, H. Xing, Q. Yang, R. Krishna, Z. Bao, H. Wu, W. Zhou, X. Dong, Y. Han, B. Li, Q. Ren, M.J. Zaworotko, B. Chen, Pore chemistry and size control in hybrid porous materials for acetylene capture from ethylene, *Science*, 353 (2016) 141-144.
- [2] F. Barrionuevo, A. Naumann, S. Bagheri-Fam, V. Speth, M.M. Taketo, G. Scherer, A. Neubüser, Sox9 is required for invagination of the otic placode in mice, *Developmental Biology*, 317 (2008) 213-224.
- [3] V. Stavila, A.A. Talin, M.D. Allendorf, MOF-based electronic and opto-electronic devices, *Chemical Society Reviews*, 43 (2014) 5994-6010.
- [4] X. Fang, J. Liu, J. Wang, H. Zhao, H. Ren, Z. Li, Dual signal amplification strategy of Au nanoparticles/ZnO nanorods hybridized reduced graphene nanosheet and multienzyme functionalized Au@ZnO composites for ultrasensitive electrochemical detection of tumor biomarker, *Biosens Bioelectron*, 97 (2017) 218-225.
- [5] Y. Wang, C. Hou, Y. Zhang, F. He, M. Liu, X. Li, Preparation of graphene nano-sheet bonded PDA/MOF microcapsules with immobilized glucose oxidase as a mimetic multi-enzyme system for electrochemical sensing of glucose, *Journal of Materials Chemistry B*, 4 (2016) 3695-3702.
- [6] X. Lin, F. Luo, L. Zheng, G. Gao, Y. Chi, Fast, Sensitive, and Selective Ion-Triggered Disassembly and Release Based on Tris(bipyridine)ruthenium(II)-Functionalized Metal–Organic Frameworks, *Analytical Chemistry*, 87 (2015) 4864-4870.
- [7] X. Fang, B. Zong, S. Mao, Metal–Organic Framework-Based Sensors for Environmental Contaminant Sensing, *Nano-Micro Letters*, 10 (2018) 64.

CHAPTER III

A. Metal Organic Framework-Photocatalyst Incorporating Bis(4'-(4-Carboxyphenyl)-Terpyridine)Ruthenium(II) for Visible Light-Driven Carbon Dioxide Reduction.

In this part of our research work, our focus was on the development of new MOFs for photocatalysis applications. Our new approach is to construct metal organic frameworks (MOF) from multiple photoactive secondary building units (SBUs) to be used as photocatalysts. Initially, chemically and thermally stable molecular complexes (Ru and Os based complexes) are synthesized using heterotopic linkers (Bis(4'-(4-Carboxyphenyl)-Terpyridine)Ruthenium(II)). This molecular complex incorporating a secondary binding unit will be employed to construct the new photoactive MOFs. Finally, the ability of the frameworks to act as photocatalysts will be tested. Notably, pre-incorporation of the catalytic metal units into molecular building blocks (such as inorganic coordination clusters) can significantly increase the number of gas molecules on the surfaces of the frameworks without mitigating the specific surface area. As a proof of concept, we synthesized Ru-terpyridine based complex with carboxylate ends to be used as linkers for the MOFs synthesis. After trying different experimental conditions, we finally succeeded in growing single crystals of the Zr-Ru-Ext-Terpy-MOFs. Interestingly, the obtained structure is 1D structure namely (AUBM-4) with an unusual Zr cluster that is composed of only one Zirconium atom coordinated to 2 linkers and the rest of the coordination sphere is occupied by solvent molecules. Our strategy of using the Ru-terpyridine based complex as a linker to construct the MOF catalyst appears to be

very promising in artificial photosynthesis. The results of this work are presented in the form of a research paper published in Journal of American Chemical Society (JACS) in 2019.

Metal–Organic Framework Photocatalyst Incorporating Bis(4'-(4-carboxyphenyl)-terpyridine)ruthenium(II) for Visible-Light-Driven Carbon Dioxide Reduction

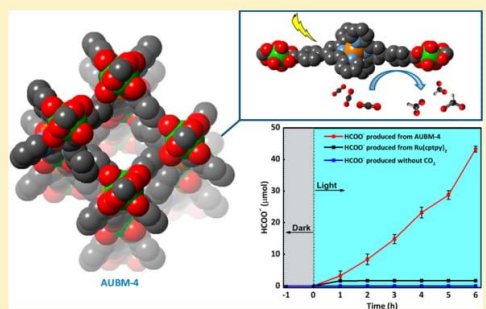
Mahmoud Elcheikh Mahmoud,[†] Hassib Audi,[†] Abdeljalil Assoud,[‡] Tarek H. Ghaddar,^{*,†} and Mohamad Hmadeh^{*,†}

[†]Department of Chemistry, American University of Beirut, P.O. Box 11-0236, Riad El-Solh 1107 2020, Beirut, Lebanon

[‡]Department of Chemistry, University of Waterloo, Waterloo, Ontario, Canada, N2L 3G1

S Supporting Information

ABSTRACT: In this study, we report the successful incorporation of the photoactive bis(4'-(4-carboxyphenyl)-terpyridine)ruthenium(II) ($\text{Ru}(\text{cptpy})_2$) strut into a robust metal–organic framework (MOF), AUBM-4. The single crystal X-ray analysis revealed the formation of a new one-dimensional structure of $\text{Ru}(\text{cptpy})_2$ complexes linked together by Zr atoms that are eight coordinated with O atoms. The chemically stable MOF structure was employed as an efficient photocatalyst for carbon dioxide conversion to formate under visible light irradiation. To the best of our knowledge, the obtained conversion rate is among the highest reported in the literature for similar systems. Our strategy of using the $\text{Ru}(\text{cptpy})_2$ complex as a linker to construct the MOF catalyst appears to be very promising in artificial photosynthesis.



1. INTRODUCTION

Metal–organic frameworks (MOFs) are hybrid crystalline structures^{1–4} that have recently emerged as promising materials in artificial photosynthesis⁵ and photocatalysis.⁶ Their high versatility, attributed to their synthetic tunability and exceptional structural properties, allows the incorporation of photoactive components (organo or metal-organo complexes) in the MOF's structures to enhance their photocatalytic properties.⁷ Moreover, MOFs have been tested as photocatalysts for many applications, such as water oxidation,^{8–10} hydrogen production,¹¹ carbon dioxide reduction,¹² and organic transformations,¹³ where specific parts of the framework had been designed to be the catalytic center, through the metal moiety, the organic linker, molecules or both.¹⁴ Therefore, the selection of the organic linkers and metal clusters is critical for the design and synthesis of MOF photocatalysts.¹⁵ The integration of photoactive centers into the MOF structures can be achieved either directly^{12,16} or via post-synthetic modifications,^{12,17} in order to improve their photocatalytic performance as compared with their homogeneous counterparts. By tuning the functionalities on the linker, it should be possible to engineer the electronic structure of the MOF photocatalysts.^{18,19} In addition, the use of MOFs in photocatalysis have been proven to be advantageous over traditional semiconductor photocatalysts due to their ability to localize electrons on distinct constituents which limits the electron–hole recombination rate.²⁰ Most of the reported MOF photocatalysts are based on Zr–O and Ti–O

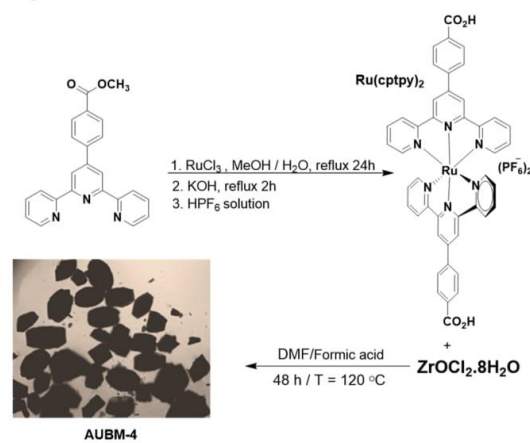
clusters^{21–23} because of their high chemical stability, low toxicity, and the variable redox states of the metal center (e.g., Ti(IV)/Ti(III), Zr(IV)/Zr(III)). The Zr–O and Ti–O based secondary building units (SBUs) appear as a robust platform for the construction of thermally and chemically stable MOF-based photocatalysts working under complicated and harsh catalytic conditions. The charge transfer process (e.g., LMCT) has been demonstrated for many of these MOF photocatalysts through the charge transfer from the excited ligand to Zr- or Ti-oxoclusters. In addition to metal clusters, functionalized organic linkers have been shown to contribute to the enhancement of the photocatalytic activity of the MOF catalysts.^{20,24,25} In fact, the amino-modified, electron-rich conjugated, and photosensitizer-functionalized linkers have been employed in the construction of highly active MOFs¹⁷ such as MIL-125, NH_2 -UiO-66, and UiO-67 doped with photoactive complexes and porphyrin-MOFs.^{26–32} The choice of these structures is due to their great visible light absorption, excess electron density, and strong interaction with CO_2 and/or water molecules. Particularly, the incorporation of Ru-polypyridine complexes (e.g., $\text{Ru}(5,5'\text{-dcbpy}$ and $\text{Ru}(4,4'\text{-dcbpy}))$, in the backbone of the frameworks, has been shown to be an effective strategy to enhance the photocatalytic properties of the MOF structures³³ due to their high oxidation and reduction power and long lifetime of their excited

Received: February 26, 2019

Published: April 11, 2019

states.^{34–36} Although the robust and highly photoactive Ru-(terpyridine)₂ complexes and their derivatives have been widely used in homogeneous photocatalysis,³⁷ their integration into MOF structures to produce new photoactive materials is not well exploited.¹¹ Herein, we report the first structure of a photoactive Zr-MOF incorporating bis(4'-(4-carboxyphenyl)-terpyridine)Ru(II) complex (Ru(cptpy)₂) in its backbone (Scheme 1). Interestingly, the obtained Zr cluster was based on the simple ZrO₈ cluster and not the conventional Zr₆O₄(OH)₄(CO₂)₁₂, found in UiO-66 topology. The new MOF structure was found to be highly stable and highly efficient for the visible light driven conversion of CO₂ to formate.¹³ CO₂ was used to confirm the origin of the formate ions produced throughout the photochemical reaction. Finally, a mechanism of the CO₂ photoreduction was discussed based on the experimental analysis and the Density Functional Theory (DFT) calculations.

Scheme 1. Synthesis of Ru(cptpy)₂ Linker and AUBM-4 Crystals



2. EXPERIMENTAL METHODS

2.1. Material and Methods. RuCl₃·3H₂O, 4-methoxycarbonylbenzaldehyde, 2-acetylpyridine, and all other chemicals and solvents were purchased from Sigma-Aldrich and used without any further purification. Infrared (IR) spectra were recorded on an FT-IR spectrometer Thermo-Nicolet working in the transmittance mode, in the 450–3950 cm⁻¹ range. Thermogravimetric Analysis (TGA) was performed with Netzsch TG 209 F1 Libra apparatus. Powder X-ray diffraction (PXRD) patterns were collected using a Bruker D8 advance X-ray diffractometer (Bruker AXS GmbH, Karlsruhe, Germany) at 40 kV, 40 mA (1600 W) using Cu K α radiation ($k = 1.5418 \text{ \AA}$). Absorption spectra were recorded at room temperature using a JASCOV-570 UV–vis–NIR spectrophotometer. The steady state fluorescence measurements were recorded with a resolution increment of 1 nm, slit 5 using a HORIBA Jobin Yvon Fluorolog-3 and fluorescence program. The excitation source was a 100 W xenon lamp, and the detector used was an R-928 operating at a voltage of 950 V. The formate ions were detected by 850 professional ion chromatography (Metrohm) with a Metrosep A supp 7- 250/4.0 column. NMR spectra were acquired on an AC500 Bruker spectrometer (¹H and ¹³C NMR at 500 MHz). Chemical shifts were recorded in delta (δ) units and expressed as ppm values relatively to the internal standard TMS.

2.2. Synthesis of (Ru(cptpy)₂). 4'-(4-Methoxycarbonylphenyl)-2,2':6',2''terpyridine was synthesized according to a published

procedure.³⁸ Synthesis of the [(4'-(4-carboxyphenyl)tpy)₂Ru](PF₆)₂ was performed according to a modified procedure.³⁹ RuCl₃·3H₂O (130 mg, 0.5 mmol) and 4'-(4-Methoxycarbonylphenyl)-2,2':6',2''terpyridine (366 mg, 0.99 mmol) were added to a mixture of ethanol/water 1/1 (10 mL) in a round-bottom flask. The solution was refluxed overnight under an argon pressure, and then KOH (190 mg) was added and the obtained mixture was refluxed for 2 h. After cooling at room temperature, the solvents were evaporated. The crude product was washed with acetone and dissolved in few milliliters of DMF, and then ammonium hexafluorophosphate solution was added followed by HPF₆ solution. The precipitate was filtered and washed with water. Yield: 451.5 mg, 95%. Crystals of Ru(cptpy)₂ were produced by slow evaporation of a dimethylformamide solution of Ru(cptpy)₂ in the presence of urea. A summary of crystal data and refinement results is given in Table S1.

2.3. Synthesis of AUBM-4. In a 4 mL scintillation vial, 10 mg (0.01 mmol) of the complex (Ru(cptpy)₂) were dissolved in 2.5 mL of DMF and sonicated for 5 min, and then ZrOCl₂·H₂O (30 mg, 0.09 mmol) was added. After 10 min of further sonication, 700 μ L of formic acid were added and the reaction mixture was sonicated for a couple of minutes. The mixture was placed in a preheated oven at 120 °C for 48 h. Red crystals of suitable size for single X-ray analysis were obtained (yield 73% based on (Ru(cptpy)₂)). The crystals were washed with DMF for 2 d, and the solution was exchanged with fresh DMF three times per day. This was followed by washing with acetonitrile (MeCN) for 2 d, and the solvent was exchanged with fresh MeCN three times per day. The crystals were collected and dried under dynamic vacuum at 70 °C for 6 h.

2.4. Single X-ray Analysis. The single-crystal X-ray diffraction study was performed using a Bruker Kappa Apex II CCD,⁴⁰ with Mo K α radiation at room temperature. Several red block-like single crystals were tested, and they were heavily twinned. The best crystal was chosen for data collection using the APEX II suite search strategy by scanning ω - and ϕ in different sets of frames for full data coverage. The exposure time was 30 s per frame. The data were corrected for Lorentz and polarization effects, and a multiscan absorption correction was applied using the SADABS part of the APEX II software. The structure solution was obtained by direct method and refined using the least-square method incorporated into the SHELXTL package.⁴¹ All the non-hydrogen atoms were refined anisotropically, and all the hydrogen atoms were refined in the idealized geometrically positions using a rigid model with C–H = 0.93 \AA and isotropic displacement parameters $U_{\text{iso}}(\text{H}) = 1.2U_{\text{eq}}(\text{C})$. At the end of the refinement, the SQUEEZE function part of PLATON⁴² program was used to check for a potential solvent accessible void by removing the electron density from a highly disordered solvent; the structure model was refined again and reached a reasonable R -value. A summary of crystal data, experimental details, and refinement results is given in Table S2.

2.5. Photocatalytic Reaction. 40 mL of acetonitrile (MeCN) and 10 mL of triethanolamine (TEOA) previously purged with argon gas were added into a 100 mL enclosed two-necked pear-shaped flask containing 20 mg of AUBM-4, and then the mixture was purged again with argon gas to remove dissolved oxygen. The mixture was placed at 20 cm irradiated with a 150 W xenon lamp through an AM 1.5 filter at room temperature with continuous stirring. After the reaction, the HCOO⁻ ions formed were detected by 850 professional ion chromatography (Metrohm) instrument with a Metrosep A supp 7- 250/4.0 column. The eluent is a solution of 3.6 mM of Na₂CO₃ and 2.5 mM HNO₃.

3. RESULTS AND DISCUSSION

3.1. Structural Characterization. The synthesis of the Ru(cptpy)₂ and the subsequent preparation of AUBM-4 (AUBM = American University of Beirut Materials) crystals employing this strut are summarized in Scheme 1 (NMR spectra are shown in Figures S1 and S2). Dark red crystals of Ru(cptpy)₂ were obtained by slow evaporation of the DMF in the presence of urea at 120 °C. The crystal structure is

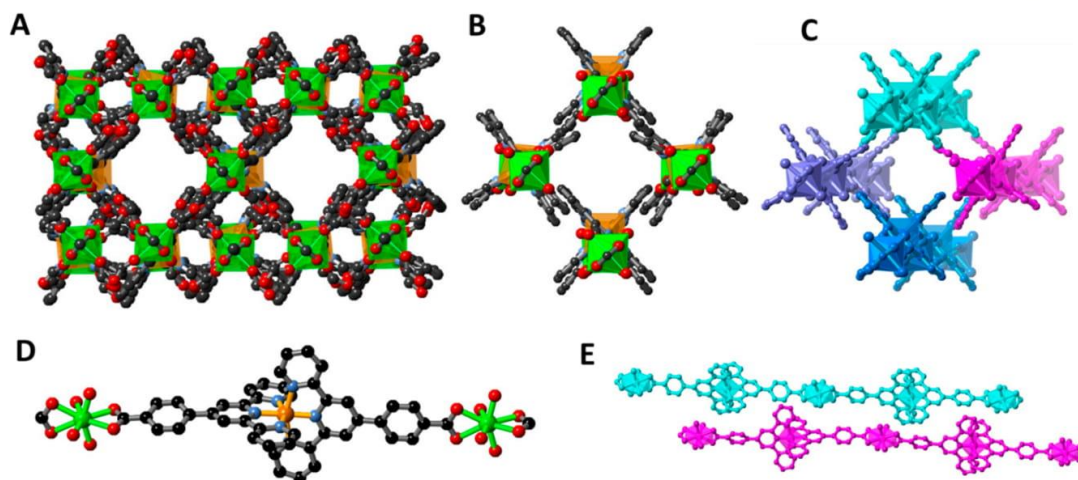


Figure 1. Crystal structure of AUBM-4: view along x axis (A), selected adjacent chains showing the π - π interactions (B), the four chains are in different colors (C), Zr-Ru-Zr chain of AUBM-4 (color scheme: Ru, gold; Zr, green; C, black; O, red; N, blue) (D), and side view of two of the adjacent linear chains presented in cyan and turquoise (E). Hydrogen atoms are omitted for clarity.

presented in Figure S3, and the crystallographic parameters are given in Table S1. It exhibits structural parameters related to the $\text{Ru}(\text{tpy})_2$ core that are typical of such compounds and shows that the Ru-N bonds are within the expected values with slight distortion in the N-Ru-N angles from ideal octahedral geometry. Mixing $\text{Ru}(\text{cptpy})_2$ and $\text{ZrOCl}_2 \cdot 8\text{H}_2\text{O}$ in DMF in the presence of a small amount formic acid at 120 °C in a capped vial for 48 h resulted in the formation of red crystals of AUBM-4. The crystal structure of AUBM-4 adopts the monoclinic space group $C2/c$ with 8 molecules per unit cell. All the atoms are located on general positions 8f except for Ru1A and Ru1B which are at Wyckoff position 4e with point symmetry 2. The crystal structure contains two crystallographically independent molecules connected through (Ru1A, Zr1A, and Ru1B) and (Ru2A, Zr2B, Ru2B, and Zr2C), respectively (Figure S4 and Table S2). These molecules form an infinite one-dimensional network along the large a -axis as shown in Figure 1. These infinite chains could be described as a link between the inorganic ZrO_8 secondary building units (SBUs) and the two $\text{Ru}(\text{cptpy})_2$ complex struts, producing one-dimensional chains of $\text{Zr-Ru}(\text{cptpy})_2$ running parallel to one another. The coordination sphere around the Zr atoms is completed by oxygen atoms from the solvent molecules to form ZrO_8 polyhedra, which are one of the five to date known Zr-based clusters in Zr-MOFs. Nevertheless, this coordination was found only in two phenolic Zr-MOFs where the polyhedra share edges to form rodlike SBUs.⁴³ The chains are linked together through secondary interactions such as π - π interactions and hydrogen bonds.

To verify the phase purity of the AUBM-4 crystals, the powder X-ray diffraction (PXRD) pattern was recorded and compared to the simulated pattern obtained from single crystal data. As shown in Figure 2, the diffraction peaks of the as-synthesized AUBM-4 are in agreement with the simulated data, thus confirming the high crystallinity and phase purity of the MOF. This was further confirmed by the scanning electron microscopy (SEM) images and by energy-dispersive X-ray (EDX) mapping analyses which were conducted on the obtained crystals and revealed their homogeneity and the

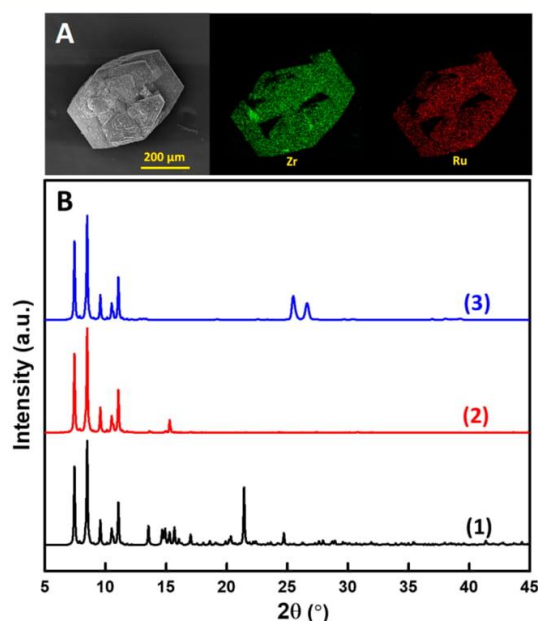


Figure 2. SEM image of AUBM-4 crystal and its mapping elements (Zr and Ru) (A); powder X-ray diffraction patterns of simulated (1), as synthesized AUBM-4 crystals (2), and after suspension in water for 1 week (3) (B).

coexistence of the elements Zr and Ru in all crystals (Figure 2 and Figure S5A). Chemical stability is of significant importance for catalysis applications, since catalysts should remain robust throughout the reaction and regeneration phases. Zr-based MOFs incorporating the octahedral and cubic clusters are reported to be highly stable; however, our AUBM-4 is composed of simple ZrO_8 cores with only two bidentate carboxylate groups and four O from the solvent, which could potentially lead to a fragile framework. Thus, we tested the

framework structural stability by soaking the crystals in aqueous solution and in organic solvents, for 1 week. PXRD patterns of the samples were collected after the stability test. As shown in Figure 2 and Figure S5B, the high crystallinity was retained even after soaking them in these solutions for 1 week. Although AUBM-4 is a one-dimensional structure, the packing of the chains of Zr-Ru(cptpy)₂ shows the existence of a porous network. In order to assess this porosity, the N₂ isotherm was performed on the activated MOF samples and the Brunauer–Emmett–Teller (BET) surface area was determined to be 50 m²/g (Figure S6A). The thermal stability was also investigated by thermogravimetric analysis (TGA), and the weight loss profile of the activated MOF revealed several steps for the degradation of the framework starting at 300 °C where about 20% of the initial weight was lost rapidly. This was followed by two small steps of weight loss between 300 and 750 °C to reach 35% of weight loss, indicating the complete degradation of the framework (Figure S6B).

3.2. Optical Properties. To quantify the light absorption ability of AUBM-4 crystals, the diffuse reflectance of AUBM-4 powder was measured and the optical band gap was calculated to be 1.88 eV using the Tauc plot (Figure S7A). The absorption band could be attributed to the singlet metal-to-ligand charge transfer (¹MLCT) of ruthenium metalloligands within the MOF structure (Figure S7B). This was further observed in the luminescence spectra for both Ru(cptpy)₂ and AUBM-4 where the MLCT state luminescence of Ru²⁺-based complexes was detected (Figure 3). Furthermore, the

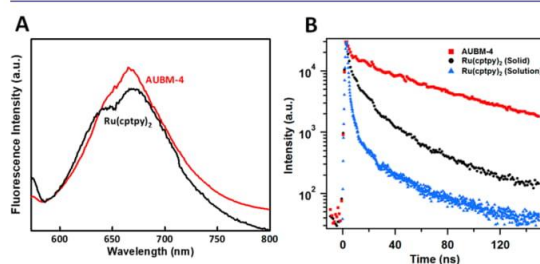


Figure 3. Photoluminescence spectra of Ru(cptpy)₂ and AUBM-4 (A). Time resolved luminescence traces at 520 nm of AUBM-4 crystals suspended in acetonitrile (red) and for Ru(cptpy)₂ suspended in chloroform (black) or dissolved in acetonitrile (blue) (B).

luminescence decays for Ru(cptpy)₂ and AUBM-4 show that AUBM-4 has a longer lifetime [$\tau = 3.6$ ns (27%) and 54.1 ns (63%)] when compared to the Ru(cptpy)₂ complex [2.7 ns (37%) and 18.4 ns (63%)] in their solid forms.

3.3. Photocatalytic CO₂ Reduction. To evaluate the potential of AUBM-4 in photocatalytic applications, we examined its photochemical properties by visible light driven catalytic reduction of CO₂. The CO₂ photoreduction reaction was conducted using AUBM-4 crystals as a heterogeneous photocatalyst with triethanolamine (TEOA) as a sacrificial agent and acetonitrile (MeCN) as the solvent saturated with CO₂. The amount of the photocatalytic product (HCOO⁻ anion) was quantified by ion chromatography (IC) analysis of the solution (Figure S8), and the obtained results are shown in Figure 4. The formate production increases linearly with time to reach 44 μ mol in 6 h with an average formation rate of 7.3 μ mol/h. Interestingly, the obtained rate was much higher than those obtained using previously reported MOF catalysts such

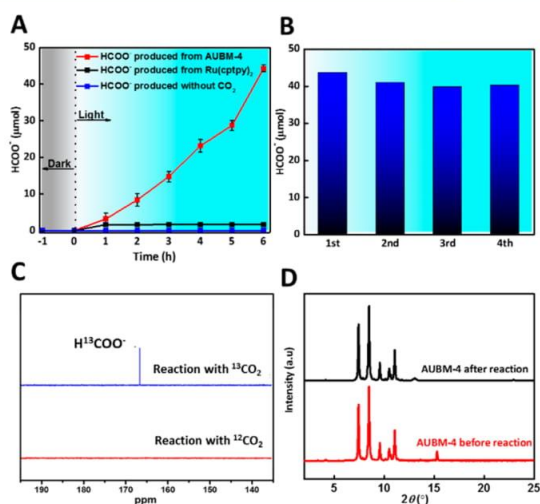


Figure 4. Amount of HCOO⁻ generated from CO₂ as a function of the time of irradiation over AUBM-4, Ru(cptpy)₂, and in the absence of CO₂ source (A), recyclability of AUBM-4 photocatalyst (B), ¹³C NMR showing the carbon source of the produced formate (C), and PXRD patterns of the catalyst recorded before and after the reaction (D).

as PCN-222, UIO-66-NH₂, and MIL-125-NH₂ under similar conditions (Table 1).^{12,32,44,49}

Table 1. Conversion Rates for CO₂ Reduction to Formate Using Common MOF Photocatalysts under Similar Experimental Conditions (MeCN/TEOA)

| Catalyst | Rate of HCOO ⁻ [μ mol·g ⁻¹ ·h ⁻¹] | Irradiation range (nm) and Lamp intensity | ref |
|---|--|---|-----------|
| PCN-222 | 60 | 420–800 (300 W) | 44 |
| NH ₂ -UIO-66(Zr) | 26.4 | 420–800 (500 W) | 32 |
| NH ₂ -MIL-53(Fe) | 116.25 | 420–800 (300 W) | 45 |
| 253-Ru(5,5'-dcbpy)(CO) ₂ Cl ₂ | 205.8 | 420–800 (300 W) | 46 |
| MIL-101(Fe) | 147.5 | 420–800 (300 W) | 45 |
| Zr-SDCA-NH ₂ | 40.8 | 400–600 (300 W) | 47 |
| NNU-28 | 52.8 | 420–800 (300 W) | 25 |
| Ir-CP | 158.3 | 420–800 (500 W) | 48 |
| Eu-Ru(phen) ₃ -MOF | 94 | 420–800 (300 W) | 12 |
| AUBM-4 | 366 | 420–800 (150 W) | This work |

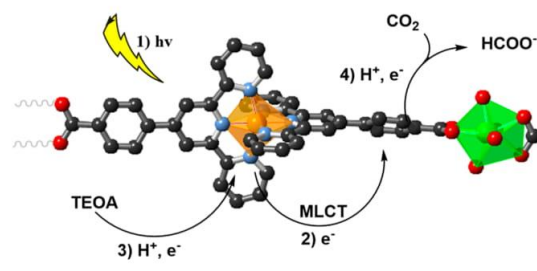
The higher production rate was attributed to the integration of photosensitizing and light harvesting complexes in the backbone of the framework. Furthermore, a small amount of formate was produced when the linker was used as a homogeneous photocatalyst (2 μ mol), while no formate was detected in the absence of catalyst, light, or CO₂. It is noteworthy that no significant amount of methane or other

hydrocarbon gas products were detected in the gas phase after 6 h of irradiation, as evidenced by the GC-MS analysis of the product in the head space of the reactor under our experimental conditions (Figure S9). In addition, we performed the photocatalytic production of CO₂ over AUBM-4 under a monochromatic 532 ± 5 nm light irradiation where only the ruthenium center absorbs, and again we detected the formation of formate in the solution (Figure S10). To investigate the photochemical stability of our photocatalyst, AUBM-4 was recycled and reused for four consecutive cycles, and the conversion of CO₂ to formate was monitored in each cycle. As shown in Figure 4B, there is no significant change in the amount of HCOO⁻ anions produced from one cycle to another. Moreover, PXRD, SEM imaging, IR spectra, and BET measurements of the recycled MOF catalyst have been assessed and the results appear to be in good agreement with those of the as-synthesized sample, which demonstrates the high stability of the catalyst (Figure 4D and Figures S11–S13). The previously reported studies are interesting and informative considering the insight they provide regarding the generation of solar fuels. Unfortunately, only a small fraction of these studies have highlighted the effect of adventitious carbon contamination pervasive on the surface and the pores of these photocatalysts, which can provide false positives of their real performance metrics. The control of the reaction using ¹³CO₂ as a reactant was performed to verify the source of the obtained product HCOO⁻ in our reaction. After 6 h of photocatalytic reaction, the H¹³COO⁻ produced was analyzed by ¹³C NMR spectroscopy and a peak at 167.7 ppm was observed and assigned to H¹³COO⁻ (Figure 4C and Figures S14–S15), which clearly demonstrates that AUBM-4 is able to convert CO₂ to HCOO⁻ through a photocatalytic reaction.

3.4. Density Functional Theory Calculations. In order to gain some insight into the mechanism of this photocatalytic reaction, we performed Density Functional Theory (DFT) calculations using the B3LYP/6-311G(d,p) exchange correlation functional with the Los Alamos effective core potential LanL2DZ⁵⁰ as implemented in the Gaussian03 program package.⁵¹ We optimized the geometry of a small unit of AUBM-4 (without fixing atoms) containing one ruthenium and two zirconium centers in acetonitrile medium using the C-PCM algorithm⁴⁹ (Figure S16). The HOMO, HOMO–1, and HOMO–2 have a ruthenium t_{2g} character and small contribution from the π-bonding orbitals of the ctpy ligand, but with no contribution from the zirconium centers. Similarly, the LUMO to LUMO+3 are π* orbitals delocalized on the ctpy ligands with no contribution from the zirconium units. We also performed Time-Dependent DFT calculations (TD-DFT) on the same unit in acetonitrile (Table S3 and Figures S17–S18) and showed that all transitions in the visible region (to the red of 350 nm) involve the above-mentioned molecular orbitals. These results suggest that there is no electronic transition from the ruthenium center to the zirconium ones (MMCT) upon visible light excitation as expected due to the high energy of the 4d orbitals of Zr. The lowest energy calculated for an electronic transition that involves the 4d orbitals of Zr is from the HOMO to LUMO+4, and it is calculated to be at 330 nm. These results are consistent with the emission data in Figure 3, where the emission lifetime of AUBM-4 is longer than the linker alone and therefore the MMCT is absent. These results in addition to the fact that the Ru(ctpy)₂ shows some CO₂ photoreduction suggest that the photocatalytic reduction reaction most probably takes place at

the ctpy center. We speculate that, upon photoexcitation and the fast ruthenium-to-ctpy MLCT, the ruthenium center becomes reduced by TEOA and the ctpy^{•-} radical anion transfers the electron to CO₂ whether in its vicinity or coordinated to the zirconium metal, since the latter has exposed sites that can coordinate CO₂ (Scheme 2).

Scheme 2. Proposed Mechanism for CO₂ Photoreduction over AUBM-4 under Visible Light Irradiation



Finally, we attribute the high efficiency of this catalytic photoreduction to the following facts: (i) the long emission lifetime of the visible light harvesting Ru(ctpy)₂ linker in AUBM-4; (ii) the high surface that is accessible to CO₂ in AUBM-4; and (iii) the possibility of CO₂ coordinating to the zirconium center and thus facilitating the CT reaction from the terpyridine radical anion to the coordinated carbon dioxide. Even though dual mechanistic CO₂ photoreduction in MOFs at ligand and metal sites has been reported previously,^{25,29} we speculate that the latter reaction is a direct reduction of coordinated carbon dioxide on the metal center by the linker radical anion rather than a reduction reaction by the metal center.

4. CONCLUSIONS

In conclusion, we have successfully synthesized and fully characterized a new chemically stable zirconium-based metal-organic framework, namely AUBM-4 assembled from a Ru metallo-ligand and ZrO₈ cluster. The AUBM-4 crystals display not only notable chemical stability but also high photostability and were employed as a photocatalyst for the reduction of carbon dioxide to formate under visible light irradiation. The obtained conversion rate (366 μmol·g⁻¹·h⁻¹) was among the highest reported in the literature. Recyclability of the MOF catalyst was further investigated and showed that our MOF catalyst was highly stable and was successfully regenerated. Finally, DFT calculations were performed and a mechanism for CO₂ reduction over AUBM-4 was proposed.

■ ASSOCIATED CONTENT

Supporting Information

The Supporting Information is available free of charge on the ACS Publications website at DOI: 10.1021/jacs.9b01920.

Crystallographic data for AUBM-4 (CIF)

Synthesis and characterization of the Ru(ctpy)₂ linker; synthesis and single X-ray details of AUBM-4 crystals in addition to SEMs, BET, TGAs, PXRDs after the chemical stability tests; details of the photocatalytic reduction of CO₂ including ¹³C NMR and characterization of the MOF after the reaction; DFT calculations (PDF)

Crystallographic data for Ru(cptpy)₂ (CIF)

AUTHOR INFORMATION

Corresponding Authors

*tarek.ghaddar@aub.edu.lb

*mohamad.hmadeh@aub.edu.lb

ORCID

Mahmoud Elcheikh Mahmoud: 0000-0002-0990-9128

Tarek H. Ghaddar: 0000-0002-7748-0597

Mohamad Hmadeh: 0000-0003-3027-3192

Notes

The authors declare no competing financial interest.

ACKNOWLEDGMENTS

We gratefully acknowledge the funding provided by the American University of Beirut Research Board and the K. Shair Central Research Science Laboratory. M.H. acknowledges funds from The Third World Academy of Science (TWAS) Grant No. 103277. We gratefully thank Dr. Faraj Hasanayn and Mr. Mohamad Ataya for their assistance with the DFT calculations.

REFERENCES

- (1) Furukawa, H.; Cordova, K. E.; O'Keeffe, M.; Yaghi, O. M. *Science* **2013**, *341* (6149), 1230444.
- (2) Férey, G. *Chem. Soc. Rev.* **2008**, *37* (1), 191–214.
- (3) Adil, K.; Belmabkhout, Y.; Pillai, R. S.; Cadiau, A.; Bhatt, P. M.; Assen, A. H.; Maurin, G.; Eddaoudi, M. *Chem. Soc. Rev.* **2017**, *46* (11), 3402–3430.
- (4) Mason, J. A.; Veenstra, M.; Long, J. R. *Chem. Sci.* **2014**, *5* (1), 32–51.
- (5) Zhang, T.; Lin, W. *Chem. Soc. Rev.* **2014**, *43* (16), 5982–5993.
- (6) Diercks, C. S.; Liu, Y.; Cordova, K. E.; Yaghi, O. M. *Nat. Mater.* **2018**, *17* (4), 301–307.
- (7) Li, R.; Zhang, W.; Zhou, K. *Adv. Mater.* **2018**, *30* (35), 1705512.
- (8) Wang, C.; Xie, Z.; deKrafft, K. E.; Lin, W. *J. Am. Chem. Soc.* **2011**, *133* (34), 13445–13454.
- (9) Xin-PingWu; Gagliardi, L.; Truhlar, D. G. *J. Chem. Phys.* **2019**, *150* (4), No. 041701.
- (10) Wu, X.-P.; Gagliardi, L.; Truhlar, D. G. *J. Am. Chem. Soc.* **2018**, *140* (25), 7904–7912.
- (11) Toyao, T.; Saito, M.; Dohshi, S.; Mochizuki, K.; Iwata, M.; Higashimura, H.; Horiuchi, Y.; Matsuoka, M. *Chem. Commun.* **2014**, *50* (51), 6779–6781.
- (12) Yan, Z.-H.; Du, M.-H.; Liu, J.; Jin, S.; Wang, C.; Zhuang, G.-L.; Kong, X.-J.; Long, L.-S.; Zheng, L.-S. *Nat. Commun.* **2018**, *9* (1), 3353.
- (13) Deng, X.; Li, Z.; García, H. *Chem. - Eur. J.* **2017**, *23* (47), 11189–11209.
- (14) Yuan, S.; Qin, J.-S.; Li, J.; Huang, L.; Feng, L.; Fang, Y.; Lollar, C.; Pang, J.; Zhang, L.; Sun, D.; Alsalmeh, A.; Cagin, T.; Zhou, H.-C. *Nat. Commun.* **2018**, *9* (1), 808.
- (15) Wang, J.-L.; Wang, C.; Lin, W. *ACS Catal.* **2012**, *2* (12), 2630–2640.
- (16) Zhang, Z.-M.; Zhang, T.; Wang, C.; Lin, Z.; Long, L.-S.; Lin, W. *J. Am. Chem. Soc.* **2015**, *137* (9), 3197–3200.
- (17) Cohen, S. M. *Chem. Rev.* **2012**, *112* (2), 970–1000.
- (18) Hendrickx, K.; Joos, J. J.; De Vos, A.; Poelman, D.; Smet, P. F.; Van Speybroeck, V.; Van Der Voort, P.; Lejaeghere, K. *Inorg. Chem.* **2018**, *57* (9), 5463–5474.
- (19) Hendrickx, K.; Vanpoucke, D. E. P.; Leus, K.; Lejaeghere, K.; Van Yperen-De Deyne, A.; Van Speybroeck, V.; Van Der Voort, P.; Hemelsoet, K. *Inorg. Chem.* **2015**, *54* (22), 10701–10710.
- (20) Grau-Crespo, R.; Aziz, A.; Collins, A. W.; Crespo-Otero, R.; Hernández, N. C.; Rodríguez-Albelo, L. M.; Ruiz-Salvador, A. R.; Calero, S.; Hamad, S. *Angew. Chem., Int. Ed.* **2016**, *55* (52), 16012–16016.
- (21) Yuan, S.; Qin, J.-S.; Xu, H.-Q.; Su, J.; Rossi, D.; Chen, Y.; Zhang, L.; Lollar, C.; Wang, Q.; Jiang, H.-L.; Son, D. H.; Xu, H.; Huang, Z.; Zou, X.; Zhou, H.-C. *ACS Cent. Sci.* **2018**, *4* (1), 105–111.
- (22) Logan, M. W.; Ayad, S.; Adamson, J. D.; Dilbeck, T.; Hanson, K.; Uribe-Romo, F. J. *J. Mater. Chem. A* **2017**, *5* (23), 11854–11863.
- (23) Nasalevich, M. A.; Hendon, C. H.; Santaclara, J. G.; Svane, K.; van der Linden, B.; Veber, S. L.; Fedin, M. V.; Houtepen, A. J.; van der Veen, M. A.; Kapteijn, F.; Walsh, A.; Gascon, J. *Sci. Rep.* **2016**, *6*, 23676.
- (24) Chambers, M. B.; Wang, X.; Ellezam, L.; Ersen, O.; Fontecave, M.; Sanchez, C.; Rozes, L. *J. Am. Chem. Soc.* **2017**, *139* (24), 8222–8228.
- (25) Chen, D.; Xing, H.; Wang, C.; Su, Z. *J. Mater. Chem. A* **2016**, *4* (7), 2657–2662.
- (26) Huh, S.; Kim, S.-J.; Kim, Y. *CrystEngComm* **2016**, *18* (3), 345–368.
- (27) Choi, K. M.; Kim, D.; Rungtaweivoranit, B.; Trickett, C. A.; Barmanbek, J. T. D.; Alshammari, A. S.; Yang, P.; Yaghi, O. M. *J. Am. Chem. Soc.* **2017**, *139* (1), 356–362.
- (28) Fu, Y.; Yang, H.; Du, R.; Tu, G.; Xu, C.; Zhang, F.; Fan, M.; Zhu, W. *RSC Adv.* **2017**, *7* (68), 42819–42825.
- (29) Sun, D.; Fu, Y.; Liu, W.; Ye, L.; Wang, D.; Yang, L.; Fu, X.; Li, Z. *Chem. - Eur. J.* **2013**, *19* (42), 14279–85.
- (30) Hassan, G. F.; El Hoda Saad, N.; Hmadeh, M.; Karam, P. *Dalton Trans.* **2018**, *47* (44), 15765–15771.
- (31) Majewski, M. B.; Peters, A. W.; Wasielewski, M. R.; Hupp, J. T.; Farha, O. K. *ACS Energy Lett.* **2018**, *3* (3), 598–611.
- (32) Sun, D.; Fu, Y.; Liu, W.; Ye, L.; Wang, D.; Yang, L.; Fu, X.; Li, Z. *Chem. - Eur. J.* **2013**, *19* (42), 14279–14285.
- (33) Hou, C.-C.; Li, T.-T.; Cao, S.; Chen, Y.; Fu, W.-F. *J. Mater. Chem. A* **2015**, *3* (19), 10386–10394.
- (34) Cai, M.; Loague, Q. R.; Zhu, J.; Lin, S.; Usov, P. M.; Morris, A. J. *Dalton Trans.* **2018**, *47* (46), 16807–16812.
- (35) Lan, G.; Li, Z.; Veroneau, S. S.; Zhu, Y.-Y.; Xu, Z.; Wang, C.; Lin, W. *J. Am. Chem. Soc.* **2018**, *140* (39), 12369–12373.
- (36) Liao, W.-M.; Zhang, J.-H.; Wang, Z.; Yin, S.-Y.; Pan, M.; Wang, H.-P.; Su, C.-Y. *J. Mater. Chem. A* **2018**, *6* (24), 11337–11345.
- (37) Lv, H.; Rudd, J. A.; Zhuk, P. F.; Lee, J. Y.; Constable, E. C.; Housecroft, C. E.; Hill, C. L.; Musaev, D. G.; Geletii, Y. V. *RSC Adv.* **2013**, *3* (43), 20647–20654.
- (38) Constable, E. C.; Dunphy, E. L.; Housecroft, C. E.; Neuburger, M.; Schaffner, S.; Schaper, F.; Batten, S. R. *Dalton trans.* **2007**, No. 38, 4323–32.
- (39) Cooke, M. W.; Tremblay, P.; Hanan, G. S. *Inorg. Chim. Acta* **2008**, *361* (8), 2259–2269.
- (40) Assoud, A.; Guo, Q.; Sankar, C. R.; Kleinke, H. *Inorg. Chem. Front.* **2017**, *4* (2), 315–323.
- (41) Sheldrick, G. *Acta Crystallogr., Sect. C: Struct. Chem.* **2015**, *71* (1), 3–8.
- (42) Spek, A. *Acta Crystallogr., Sect. C: Struct. Chem.* **2015**, *71* (1), 9–18.
- (43) Bai, Y.; Dou, Y.; Xie, L.-H.; Rutledge, W.; Li, J.-R.; Zhou, H.-C. *Chem. Soc. Rev.* **2016**, *45* (8), 2327–2367.
- (44) Xu, H.-Q.; Hu, J.; Wang, D.; Li, Z.; Zhang, Q.; Luo, Y.; Yu, S.-H.; Jiang, H.-L. *J. Am. Chem. Soc.* **2015**, *137* (42), 13440–13443.
- (45) Wang, D.; Huang, R.; Liu, W.; Sun, D.; Li, Z. *ACS Catal.* **2014**, *4* (12), 4254–4260.
- (46) Sun, D.; Gao, Y.; Fu, J.; Zeng, X.; Chen, Z.; Li, Z. *Chem. Commun.* **2015**, *51* (13), 2645–2648.
- (47) Sun, M.; Yan, S.; Sun, Y.; Yang, X.; Guo, Z.; Du, J.; Chen, D.; Chen, P.; Xing, H. *Dalton Trans.* **2018**, *47* (3), 909–915.
- (48) Li, L.; Zhang, S.; Xu, L.; Wang, J.; Shi, L.-X.; Chen, Z.-N.; Hong, M.; Luo, J. *Chem. Sci.* **2014**, *5* (10), 3808–3813.
- (49) Fu, Y.; Sun, D.; Chen, Y.; Huang, R.; Ding, Z.; Fu, X.; Li, Z. *Angew. Chem., Int. Ed.* **2012**, *51* (14), 3364–7.
- (50) Hay, P. J.; Wadt, W. R. *J. Chem. Phys.* **1985**, *82* (1), 270–283.

(51) Xu, H. Q.; Hu, J.; Wang, D.; Li, Z.; Zhang, Q.; Luo, Y.; Yu, S. H.; Jiang, H. L. *J. Am. Chem. Soc.* **2015**, *137* (42), 13440–13443.

B. Supporting information: Metal Organic Framework-Photocatalyst

SUPPORTING INFORMATION

Metal Organic Framework-Photocatalyst Incorporating Bis(4'-(4-Carboxyphenyl)-Terpyridine)Ruthenium(II) for Visible Light-Driven Carbon Dioxide Reduction

Mahmoud Elcheikh Mahmoud[†], Hassib Audi[†], Abdeljalil Assoud[‡], Tarek H. Ghaddar^{*†},
Mohamad Hmadeh^{*†}

[†]Department of Chemistry, American University of Beirut, P.O.Box 11-0236, Riad El-Solh 1107 2020, Beirut, Lebanon.

[‡]Department of Chemistry University of Waterloo, Waterloo, Ontario, Canada N2L 3G1.

E-mail: tg02@aub.edu.lb

E-mail: mohamad.hmadeh@aub.edu.lb

^1H NMR (d_6 -dmsO 500 MHz): δ = 9.54 (s, 4H), 9.13-9.11 (d, J = 10 Hz, 4H), 8.59-8.57 (d, J = 10 Hz, 4H), 8.31-8.29 (d, J = 10 Hz, 4H), 8.08 (t, 4H), 7.56-7.57 (d, J = 10 Hz, 2H), 7.29 (t, 4H).

^{13}C NMR (d_6 -dmsO 500 MHz): 167, 158, 155, 152, 146, 140, 138, 132, 130, 128, 128, 125, 122.

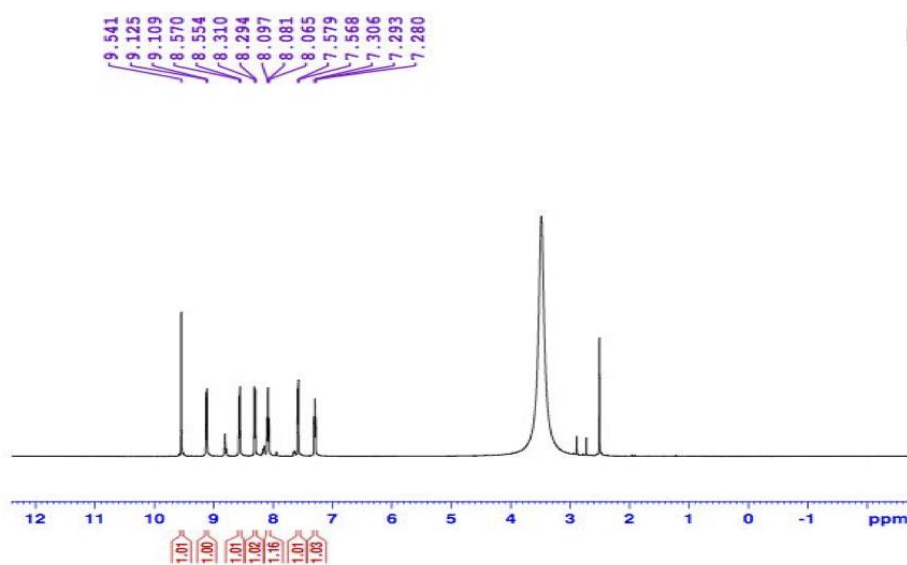


Figure S1: ^1H NMR of (1) in d_6 -dmsO at 500 MHz).

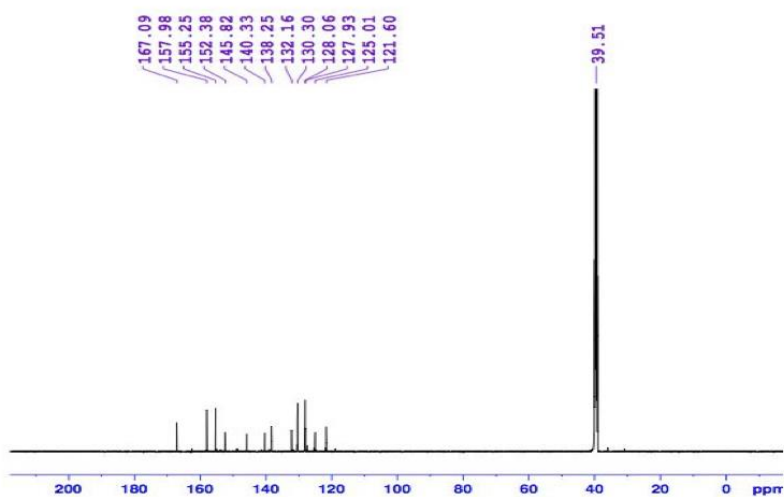


Figure S2: ^{13}C NMR of (1) in d_6 -dmsO at 500 MHz).

Table S1. Crystallographic data and structural refinement summary for Ru(cptpy)₂.

| | |
|---|--|
| Empirical formula | C ₄₄ H ₂₈ N ₆ O ₄ Ru.C ₄ H ₄ N ₂ O, 5H ₂ O |
| Formula weight | 805.79 |
| Temperature | 200 K |
| Wavelength | 0.71073 Å |
| Crystal system | Triclinic |
| Space group | <i>P</i> -1 |
| Unit cell dimensions | <i>a</i> = 9.0259(4) Å, <i>b</i> = 13.1063(5) Å, <i>c</i> = 17.2862(6) Å <i>γ</i> = 78.761(3) Å, <i>β</i> = 76.926(3) Å, <i>δ</i> = 89.888(4) Å |
| Volume | 1951.79(14) Å ³ |
| <i>Z</i> | 2 |
| Density (calculated) | 1.371 g/cm ³ |
| Absorption coefficient | 0.452 mm ⁻¹ |
| F(000) | 820.0 |
| <i>h</i> , <i>k</i> , <i>l</i> max | 11, 16, 21 |
| <i>N</i> _{ref} | 7251 |
| <i>T</i> _{min} , <i>T</i> _{max} | 0.685, 0.746 |
| <i>T</i> _{min} | 0.964 |
| Data completeness | 0.945 |
| Theta (max) | 26 |
| R (reflections) | 0.0662 (4027) |
| wR2 (reflections) | 0.1014 (7251) |
| <i>S</i> | 1.099 |

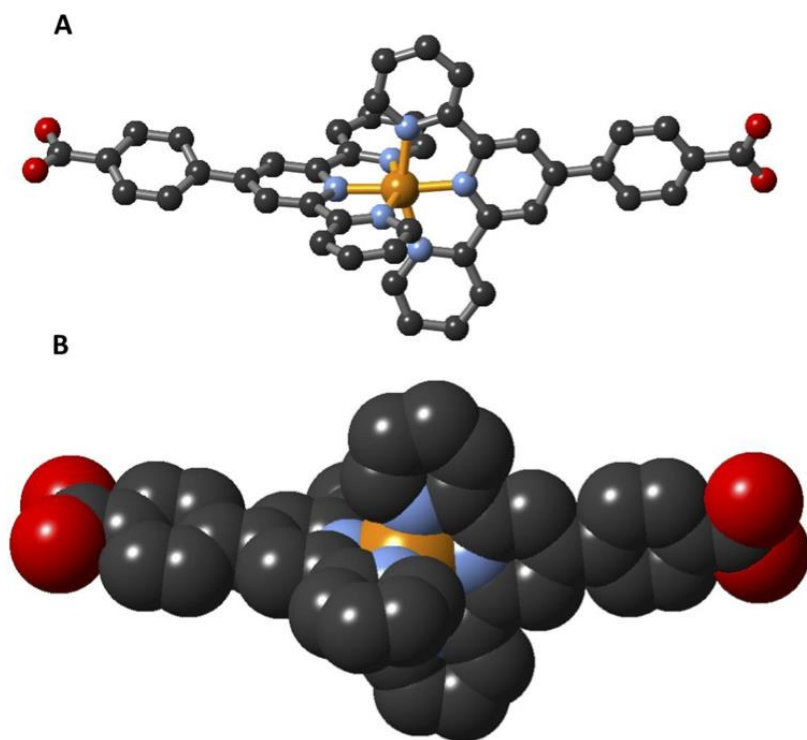
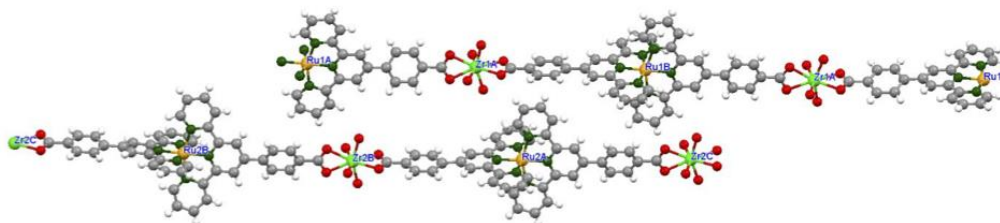


Figure S3. Crystal structure of Ru(cptpy)₂, (A) ball-and-stick, (B) space-filling representations. Color scheme: Ru, gold; C, gray; O, red; N, blue. Hydrogen atoms are omitted for clarity.

Table S2. Crystallographic data and structural refinement summary for AUBM-4.

| | |
|-----------------------------------|---|
| Empirical formula | C ₂₈₈ H ₁₉₂ N ₃₆ O ₇₂ Ru ₆ Zr ₆ |
| Formula weight | 6462.50 |
| Temperature | 296(2) K |
| Wavelength | 0.71073 Å |
| Crystal system | Monoclinic |
| Space group | <i>C2/c</i> |
| Unit cell dimensions | $a = 52.5621(8)$ Å, $b = 23.1563(4)$ Å, $c = 23.8286(4)$ Å, $\beta = 95.3350(10)$ Å. |
| Volume | 28877.2(8) Å ³ |
| Z | 4 |
| Density (calculated) | 1.486 g/cm ³ |
| Absorption coefficient | 0.598 mm ⁻¹ |
| F(000) | 13008 |
| Crystal size | 0.150 x 0.110 x 0.040 mm ³ |
| Theta range for data collection | 0.778 to 28.000°. |
| Index ranges | -69 ≤ h ≤ 69, -30 ≤ k ≤ 30, 0 ≤ l ≤ 31 |
| Reflections collected | 68270 |
| Independent reflections | 34855 [R(int) = 0.1040] |
| Completeness to theta = 25.242° | 100.0 % |
| Absorption correction | Semi-empirical from equivalents |
| Max. and min. transmission | 0.745986 and 0.645100 |
| Refinement method | Full-matrix least-squares on F ² |
| Data / restraints / parameters | 34855 / 0 / 1838 |
| Goodness-of-fit on F ² | 1.022 |
| Final R indices [I > 2σ(I)] | R1 = 0.0725, wR2 = 0.1558 |
| R indices (all data) | R1 = 0.2229, wR2 = 0.1791 |
| Largest diff. peak and hole | 1.032 and -0.692 e.Å ⁻³ |

**Figure S4.** Crystal structure of AUBM-4. The crystal structure contains two crystallographically independent molecules connected through (Ru1A, Zr1A and Ru1B) and (Ru2A, Zr2B, Ru2B and Zr2c) respectively.

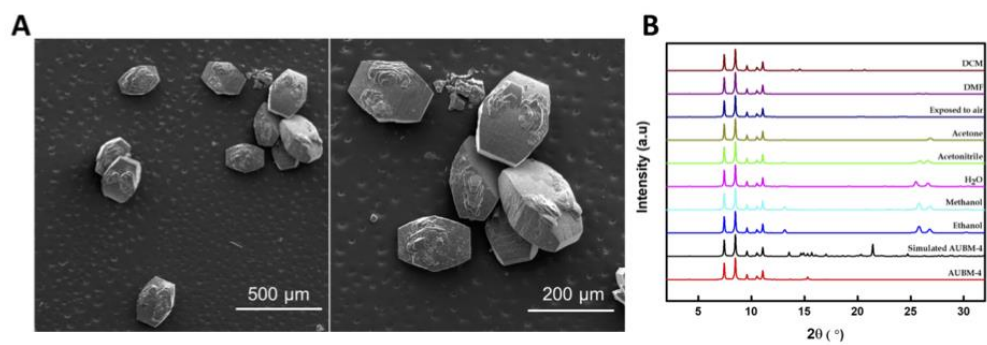


Figure S5. SEM images of AUBM-4 crystals (A), the Powder X-ray diffraction patterns of AUBM-4 after stability test (B).

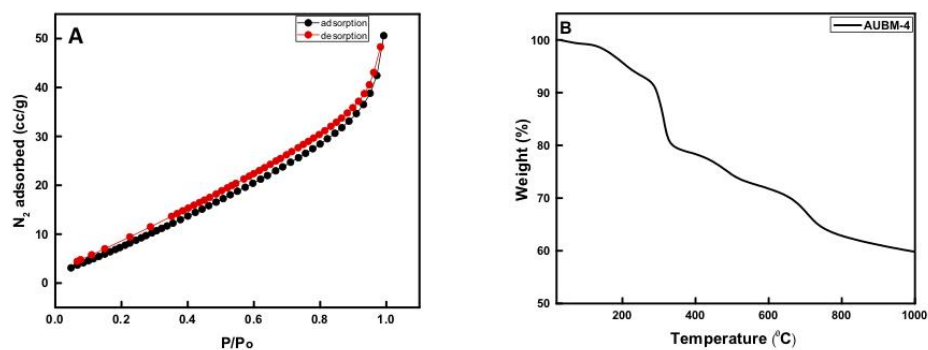


Figure S6. N_2 Adsorption-desorption of AUBM-4 (A), TGA analysis of AUBM-4 (B).

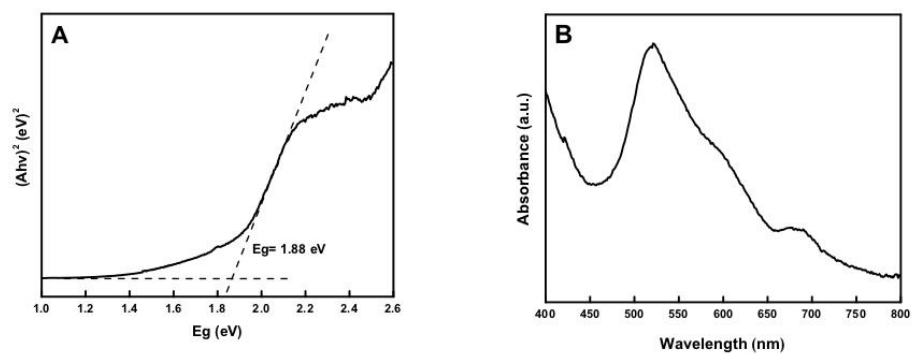


Figure S7. Tauc Plot from diffuse reflectance of AUBM-4 powder showing a band gap of 1.88 eV (A) and UV-visible absorbance spectrum of the suspended crystal in acetonitrile (B).

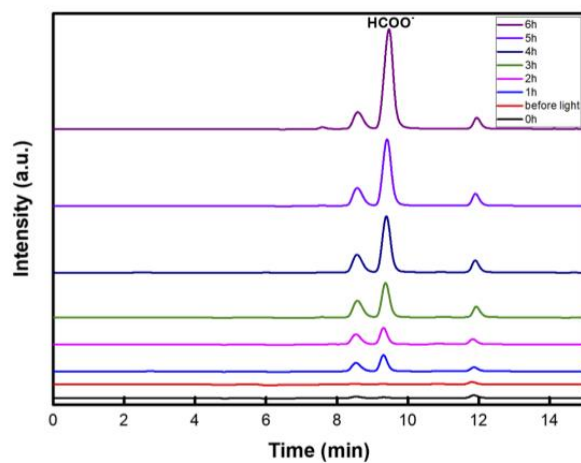


Figure S8. Ionic chromatography analyses of HCOO^- produced after different photocatalytic reaction time.

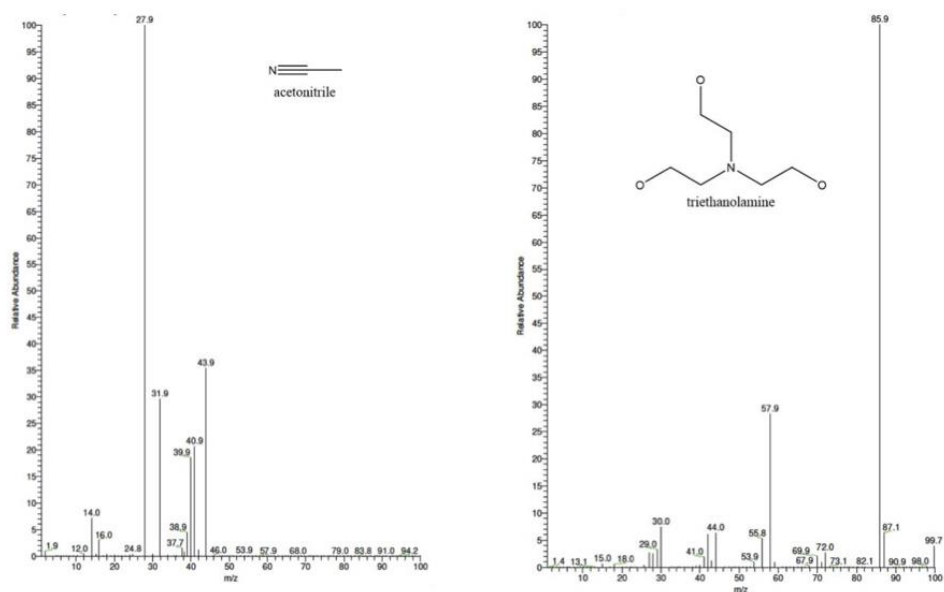


Figure S9. GC-MS of the head space product, only acetonitrile and triethanolamine vapors were detected under our experimental conditions.

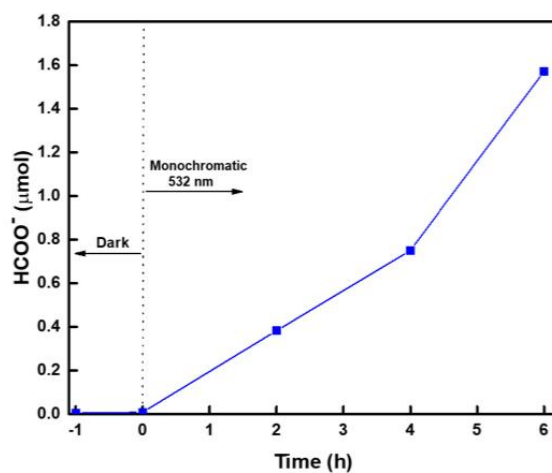
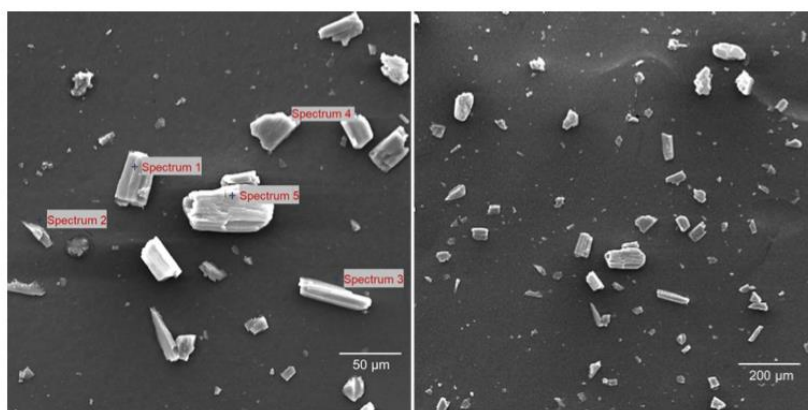


Figure S10. Photocatalytic production of CO₂ over AUBM-4 under a monochromatic light irradiation of 532 nm.



| Spectrums | O | Zr | Ru | Total % |
|-----------|-------|-------|-------|---------|
| 1 | 31.85 | 32.58 | 35.57 | 100.00 |
| 2 | 37.77 | 31.41 | 30.82 | 100.00 |
| 3 | 21.19 | 37.86 | 40.94 | 100.00 |
| 4 | 24.36 | 37.75 | 40.89 | 100.00 |
| 5 | 28.22 | 33.16 | 38.62 | 100.00 |

Figure S11. SEM images and EDX of AUBM-4 after the photocatalytic reaction showing homogenous metal compositions, indicating the stability of the catalysts throughout the photoreduction reaction.

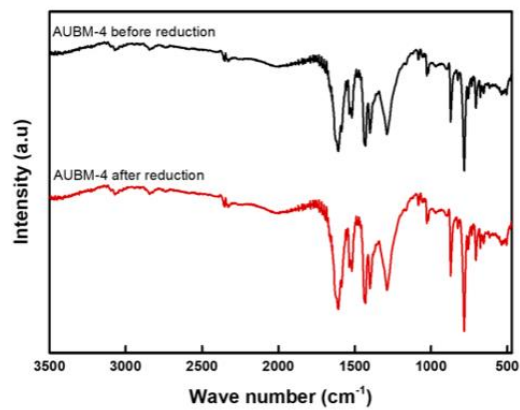


Figure S12. Infra-red spectra of AUBM-4 before and after photocatalytic reaction.

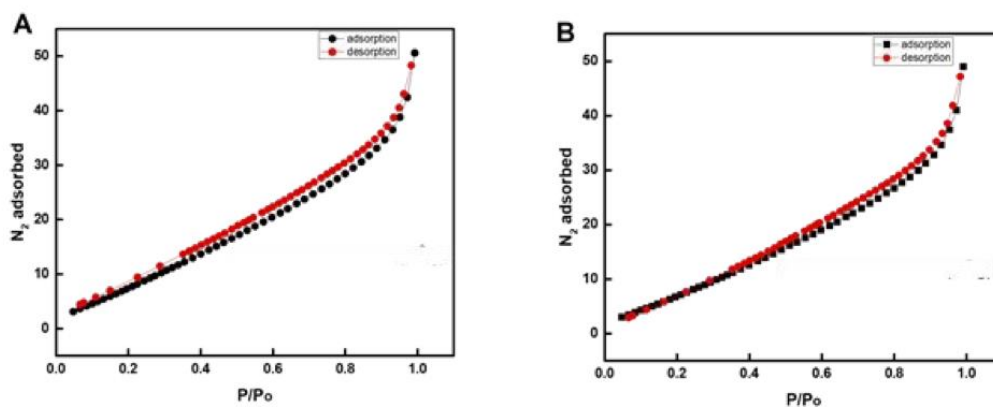


Figure S13. N_2 uptake by AUBM-4 crystals before (A) and after (B) the reaction, BET surface area are calculated to be 50 and 40 m^2/g for AUBM-4 before and after photocatalytic reaction respectively.

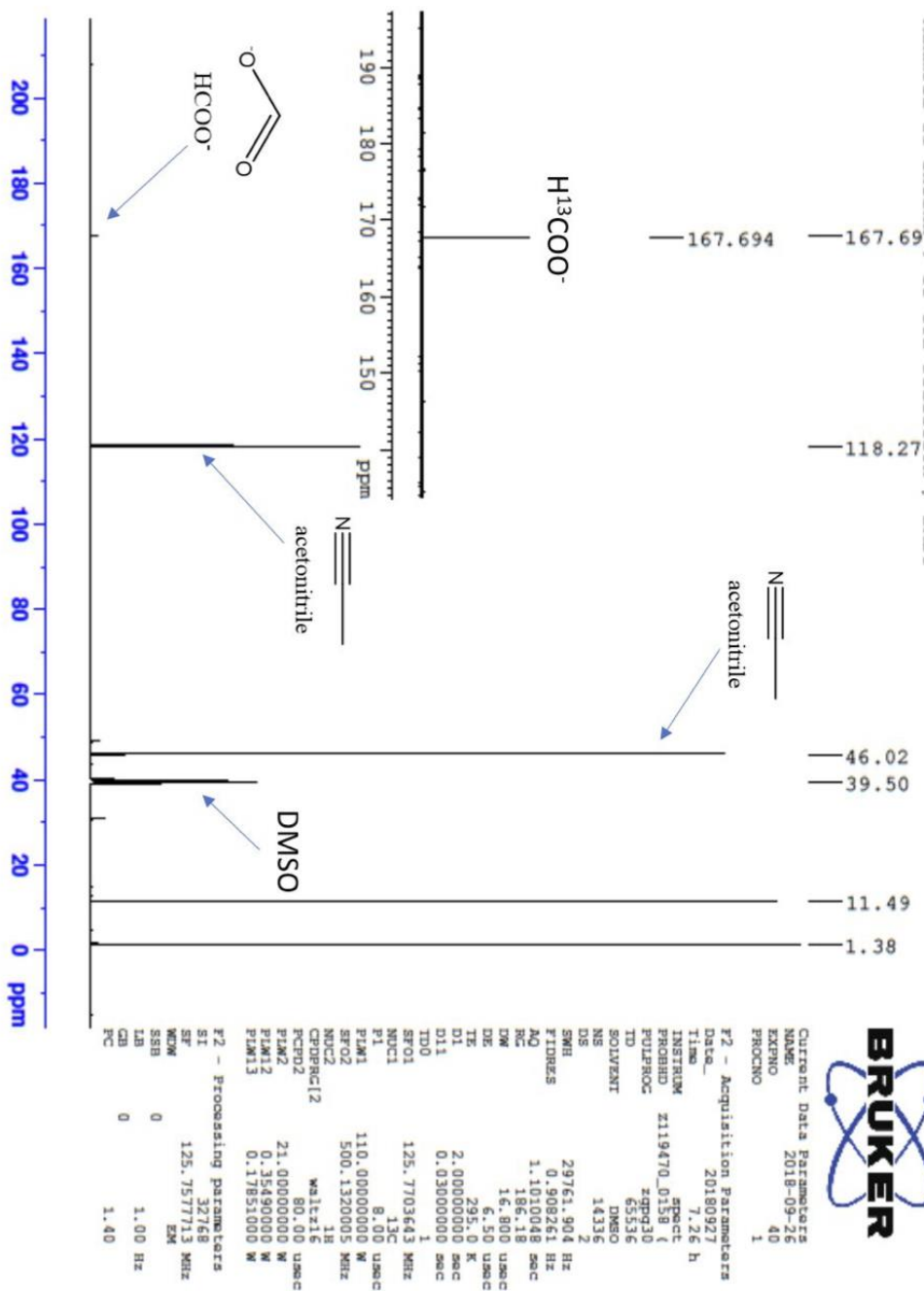


Figure S14. The ¹³C NMR spectra for the obtained product.

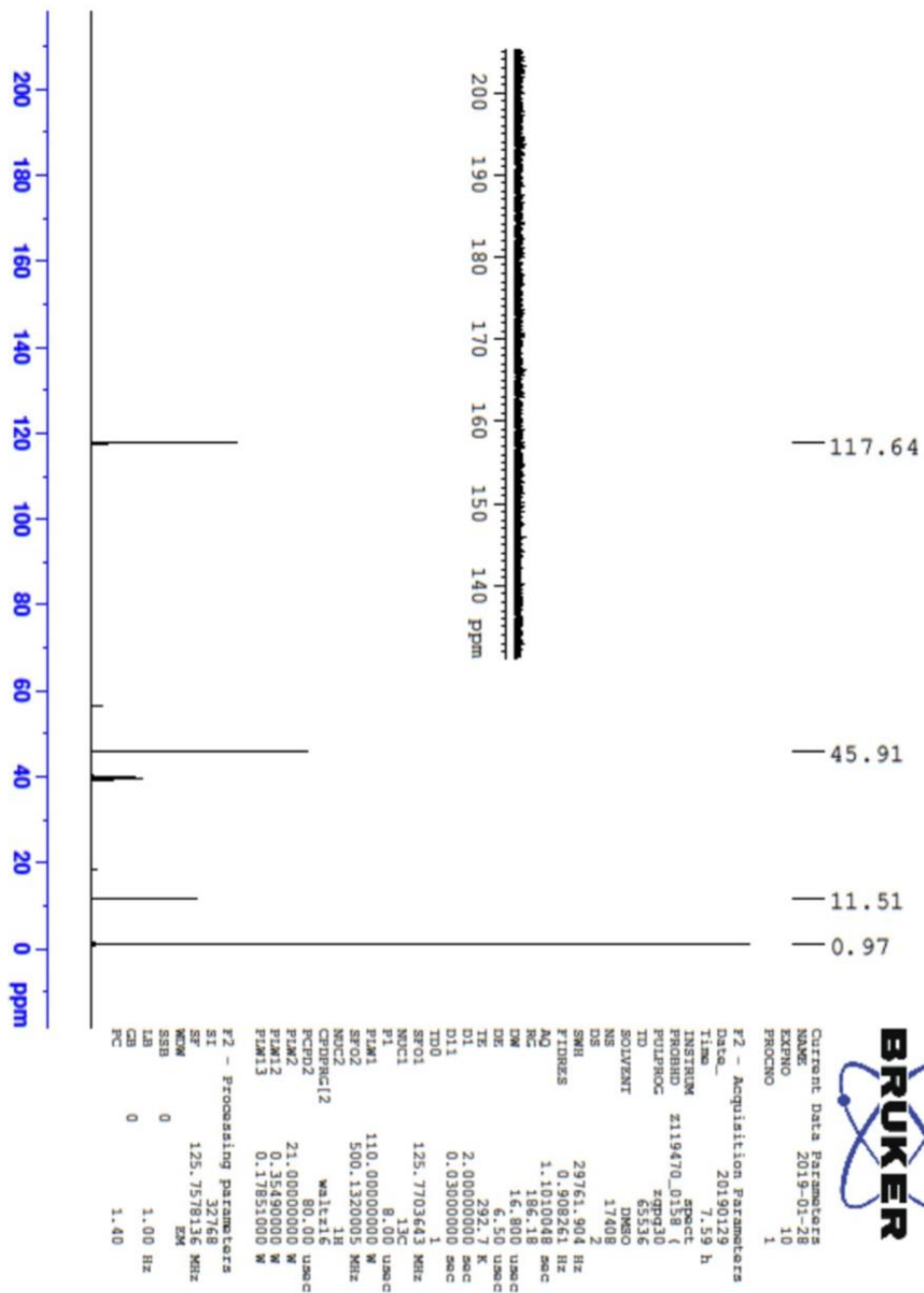


Figure S15. The ^{13}C NMR spectra for the obtained product using $^{12}\text{CO}_2$ as a source.

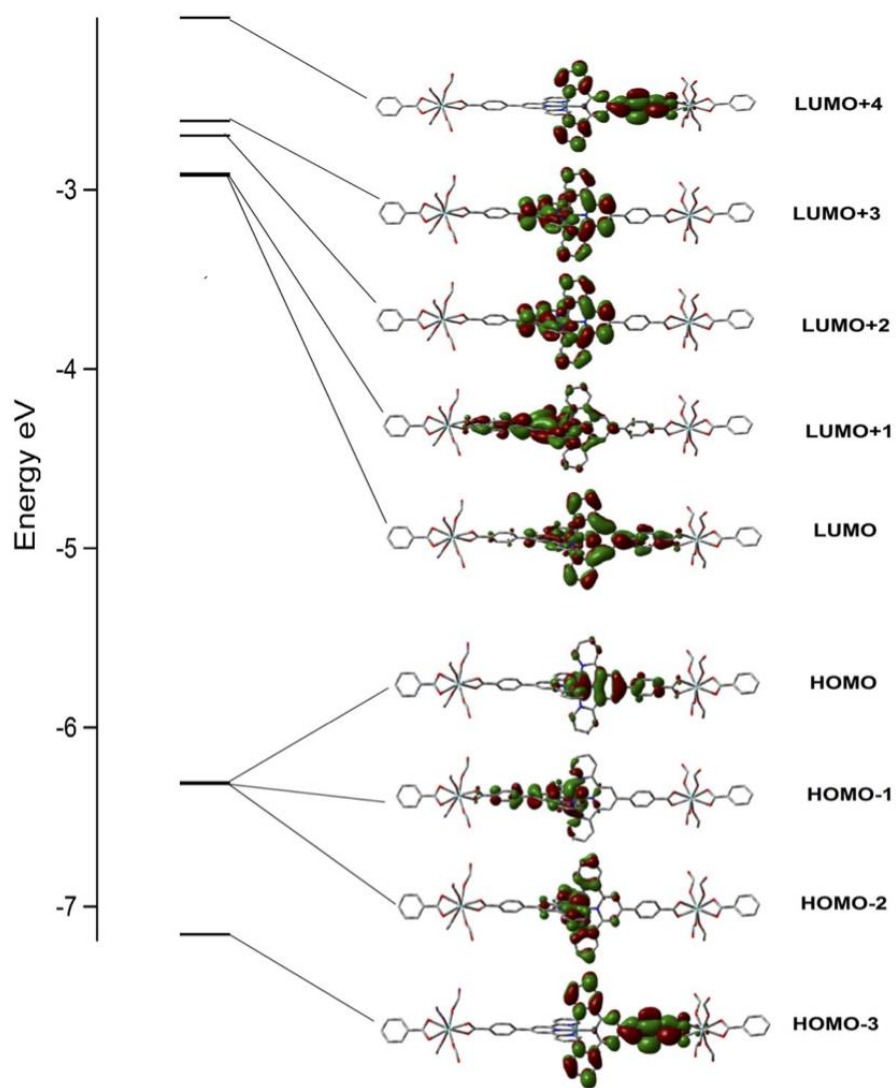


Figure S16. Molecular orbital energy diagram of AUBM-4 unit. The HOMO-LUMO gaps are reported in eV. The isodensity plots shown are for the HOMO - 3, HOMO - 2, HOMO - 1, HOMO, LUMO, LUMO + 1, LUMO + 2, LUMO + 3 and LUMO + 4.

Table S3: Calculated spectra of AUBM-4 above 350 nm.

| E (nm) | <i>f</i> | Transition |
|--------|----------|---|
| 492.2 | 0.0113 | HOMO-2->LUMO(+95%) |
| 490.5 | 0.0115 | HOMO-2->LUMO+1(+96%) |
| 463.8 | 0.4709 | HOMO->LUMO(+40%) HOMO-1->LUMO+1(+38%) HOMO->LUMO+1(+8%) HOMO-1->LUMO(7%) |
| 432.1 | 0.0231 | HOMO->LUMO+2(+90%) HOMO-1->LUMO+2(+5%) |
| 431.8 | 0.0218 | HOMO-1->LUMO+2(+91%) HOMO->LUMO+2(5%) |
| 427.5 | 0.0135 | HOMO->LUMO+3(+92%) |
| 427.4 | 0.0155 | HOMO-1->LUMO+3(+92%) |
| 425 | 0.2266 | HOMO-2->LUMO+2(+94%) |

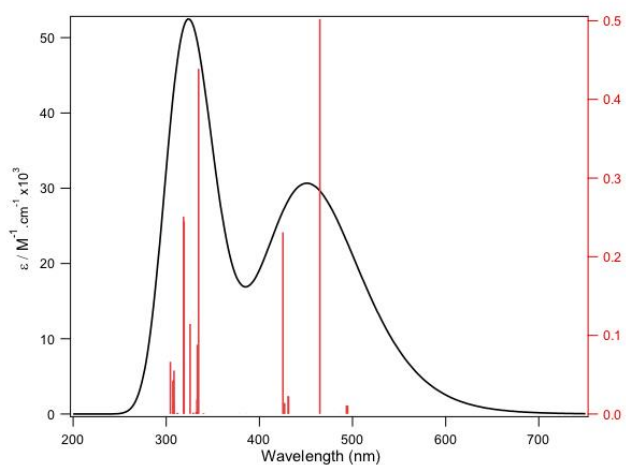


Figure S17: The computed absorption spectrum of AUBM-4 unit.

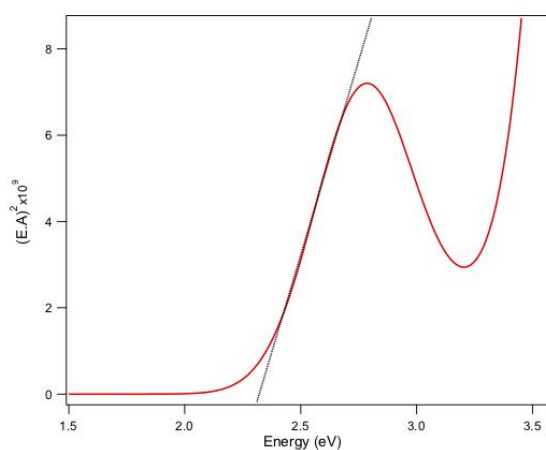


Figure S18: The derived Tauc Plot from the TD-DFT of the AUBM-4 unit showing a band gap of ~ 2.3 eV.

CHAPTER IV

CONCLUSION

This work demonstrated the design and synthesis of new kind of Metal Organic Frameworks (MOFs) using new type of linkers. From the proposed linkers, we have succeeded to prepare a set of new materials with unprecedented electrical, chemical, and topological properties for sensing and photocatalysis applications.

In the first project, we succeeded to create a new set of luminescent MOFs, namely AUBM-2 and AUBM-3. The single crystals of Lanthanides MOFs were obtained by the solvothermal reaction of DNP and NP and $\text{LnNO}_3 \cdot 6\text{H}_2\text{O}$ where Ln is (La and Ce) in a mixture of DMF/H₂O/EtOH. All the four lanthanides-based MOFs were thoroughly characterized using single crystal and powder X-ray diffraction, TGA, IR, UV-Vis, fluorescence analysis. Their sensing properties were further investigated for toxic elements (Pb(II), Cr(IV), As(III), Cd(II), Hg(II)) and paraquat. The quenching effect induced by the mercury metals for AUBM-3(Ce) was great with K_{sv} values of 2061 M⁻¹ and 1289 M⁻¹ after exciting at 300 nm and 370 nm respectively. Compared to the other heavy metals tested, this quenching effect was only evident in the case of mercury thus the AUBM-3(Ce) could be reported as a sensitive and selective detector for mercury ions.

In the second project, we report the first structure of a photoactive Zr-MOF incorporating bis(4-(4-carboxyphenyl)-terpyridine)Ru(II) complex ($\text{Ru}(\text{cptpy})_2$) in its backbone. Interestingly, the obtained Zr cluster was based on the simple ZrO₈ cluster and not the conventional $\text{Zr}_6\text{O}_4(\text{OH})_4(\text{CO}_2)_{12}$, found in UiO-66 topology. The crystal obtained

structure is 1D structure with an unusual Zr cluster that is composed of only one Zirconium atom coordinated to two linkers and the rest of the coordination sphere is occupied by solvent molecules. The new MOF structure was found to be highly stable and highly efficient for the visible light driven conversion of CO₂ to formate, the conversion rate (366 μmol·g⁻¹·h⁻¹) was among the highest reported in the literature. Recyclability of the MOF catalyst was further investigated and showed that our MOF catalyst was highly stable and was successfully regenerated. ¹³CO₂ was used to confirm the origin of the formate ions produced throughout the photochemical reaction. Finally, a mechanism of the CO₂ photoreduction was discussed based on the experimental analysis and the Density Functional Theory (DFT) calculations.

BIBLIOGRAPHY

1. Kim, J.; Chen, B.; Reineke, T. M.; Li, H.; Eddaoudi, M.; Moler, D. B.; O'Keeffe, M.; Yaghi, O. M., Assembly of Metal–Organic Frameworks from Large Organic and Inorganic Secondary Building Units: New Examples and Simplifying Principles for Complex Structures. *Journal of the American Chemical Society* **2001**, *123* (34), 8239-8247.
2. Eichinger, B. E.; Neuburger, N. A., Differential Swelling of Elastomers. In *Biological and Synthetic Polymer Networks*, Kramer, O., Ed. Springer Netherlands: Dordrecht, 1988; pp 415-433.
3. Rungtaweivoranit, B.; Diercks, C. S.; Kalmutzki, M. J.; Yaghi, O., Spiers Memorial Lecture: Progress and prospects of reticular chemistry. *Faraday Discussions* **2017**, *201* (0), 9-45.
4. Li, H.; Eddaoudi, M.; O'Keeffe, M.; Yaghi, O. M., Design and synthesis of an exceptionally stable and highly porous metal-organic framework. *Nature* **1999**, *402*, 276.
5. KICKELBICK, G., *Hybrid Materials – Past, Present and Future*. 2014; Vol. 1.
6. Bauer, C. A.; Jones, S. C.; Kinnibrugh, T. L.; Tongwa, P.; Farrell, R. A.; Vakil, A.; Timofeeva, T. V.; Khrustalev, V. N.; Allendorf, M. D., Homo- and heterometallic luminescent 2-D stilbene metal-organic frameworks. *Dalton transactions (Cambridge, England : 2003)* **2014**, *43* (7), 2925-35.
7. Yasumoto, T.; Murata, M., Marine toxins. *Chemical Reviews* **1993**, *93* (5), 1897-1909.
8. Silva, C. G.; Corma, A.; Garcia, H., Metal-organic frameworks as semiconductors. *Journal of Materials Chemistry* **2010**, *20* (16), 3141-3156.
9. Furukawa, H.; Ko, N.; Go, Y. B.; Aratani, N.; Choi, S. B.; Choi, E.; Yazaydin, A. Ö.; Snurr, R. Q.; O'Keeffe, M.; Kim, J.; Yaghi, O. M., Ultrahigh Porosity in Metal-Organic Frameworks. *Science* **2010**, *329* (5990), 424-428.
10. Saliba, D.; Ammar, M.; Rammal, M.; Al-Ghoul, M.; Hmadeh, M., Crystal Growth of ZIF-8, ZIF-67, and Their Mixed-Metal Derivatives. *Journal of the American Chemical Society* **2018**, *140* (5), 1812-1823.
11. Wu, H.; Yildirim, T.; Zhou, W., Exceptional Mechanical Stability of Highly Porous Zirconium Metal–Organic Framework UiO-66 and Its Important Implications. *The Journal of Physical Chemistry Letters* **2013**, *4* (6), 925-930.
12. Park, K. S.; Ni, Z.; Côté, A. P.; Choi, J. Y.; Huang, R.; Uribe-Romo, F. J.; Chae, H. K.; O'Keeffe, M.; Yaghi, O. M., Exceptional chemical and thermal stability of zeolitic imidazolate frameworks. *Proceedings of the National Academy of Sciences* **2006**, *103* (27), 10186-10191.
13. Furukawa, H.; Cordova, K. E.; O'Keeffe, M.; Yaghi, O. M., The Chemistry and Applications of Metal-Organic Frameworks. *Science* **2013**, *341* (6149).
14. Horike, S.; Dincă, M.; Tamaki, K.; Long, J. R., Size-Selective Lewis Acid Catalysis in a Microporous Metal-Organic Framework with Exposed Mn²⁺ Coordination Sites. *Journal of the American Chemical Society* **2008**, *130* (18), 5854-5855.
15. Matsuda, R.; Kitaura, R.; Kitagawa, S.; Kubota, Y.; Belosludov, R. V.; Kobayashi, T. C.; Sakamoto, H.; Chiba, T.; Takata, M.; Kawazoe, Y.; Mita, Y., Highly controlled acetylene accommodation in a metal–organic microporous material. *Nature* **2005**, *436*, 238.
16. Dechambenoit, P.; Long, J. R., Microporous magnets. *Chemical Society Reviews* **2011**, *40* (6), 3249-3265.
17. Atallah, H.; Elcheikh Mahmoud, M.; Jelle, A.; Lough, A.; Hmadeh, M., A highly stable indium based metal organic framework for efficient arsenic removal from water. *Dalton Transactions* **2018**, *47* (3), 799-806.

18. Moon, H. R.; Lim, D.-W.; Suh, M. P., Fabrication of metal nanoparticles in metal-organic frameworks. *Chemical Society Reviews* **2013**, *42* (4), 1807-1824.
19. Keskin, S.; Kizilel, S., Biomedical Applications of Metal Organic Frameworks. *Industrial & Engineering Chemistry Research* **2011**, *50* (4), 1799-1812.
20. Deng, H.; Grunder, S.; Cordova, K. E.; Valente, C.; Furukawa, H.; Hmadeh, M.; Gándara, F.; Whalley, A. C.; Liu, Z.; Asahina, S.; Kazumori, H.; O’Keeffe, M.; Terasaki, O.; Stoddart, J. F.; Yaghi, O. M., Large-Pore Apertures in a Series of Metal-Organic Frameworks. *Science* **2012**, *336* (6084), 1018-1023.
21. Mortada, B.; Matar, T. A.; Sakaya, A.; Atallah, H.; Kara Ali, Z.; Karam, P.; Hmadeh, M., Postmetalated Zirconium Metal Organic Frameworks as a Highly Potent Bactericide. *Inorganic Chemistry* **2017**, *56* (8), 4739-4744.
22. Nevruzoglu, V.; Demir, S.; Karaca, G.; Tomakin, M.; Bilgin, N.; Yilmaz, F., Improving the stability of solar cells using metal-organic frameworks. *Journal of Materials Chemistry A* **2016**, *4* (20), 7930-7935.
23. Moussa, Z.; Hmadeh, M.; Abiad, M. G.; Dib, O. H.; Patra, D., Encapsulation of curcumin in cyclodextrin-metal organic frameworks: Dissociation of loaded CD-MOFs enhances stability of curcumin. *Food Chemistry* **2016**, *212* (Supplement C), 485-494.
24. Nagarkar, S. S.; Joarder, B.; Chaudhari, A. K.; Mukherjee, S.; Ghosh, S. K., Highly Selective Detection of Nitro Explosives by a Luminescent Metal–Organic Framework. *Angewandte Chemie International Edition* **2013**, *52* (10), 2881-2885.
25. Hoskins, B. F.; Robson, R., Design and construction of a new class of scaffolding-like materials comprising infinite polymeric frameworks of 3D-linked molecular rods. A reappraisal of the zinc cyanide and cadmium cyanide structures and the synthesis and structure of the diamond-related frameworks [N(CH₃)₄][CuI₂ZnII(CN)₄] and CuI[4,4',4'',4'''-tetracyanotetraphenylmethane]BF₄.x₆H₅NO₂. *Journal of the American Chemical Society* **1990**, *112* (4), 1546-1554.
26. Wriedt, M.; Zhou, H.-C. J., Systematic investigations on magneto-structural correlations of copper(ii) coordination polymers based on organic ligands with mixed carboxylic and nitrogen-based moieties. *Dalton Transactions* **2012**, *41* (14), 4207-4216.
27. Zou, W.-Q.; Wang, M.-S.; Li, Y.; Wu, A. Q.; Zheng, F.-K.; Chen, Q.-Y.; Guo; Huang, J.-S., Unprecedented (3,10)-Connected 2-D Metal–Organic Framework Constructed from Octanuclear Cobalt(II) Clusters and a New Bifunctional Ligand. *Inorganic Chemistry* **2007**, *46* (17), 6852-6854.
28. Eddaoudi, M.; Moler, D. B.; Li, H.; Chen, B.; Reineke, T. M.; O’Keeffe, M.; Yaghi, O. M., Modular Chemistry: Secondary Building Units as a Basis for the Design of Highly Porous and Robust Metal–Organic Carboxylate Frameworks. *Accounts of Chemical Research* **2001**, *34* (4), 319-330.
29. Yang, C.-X.; Yan, X.-P., Application of Metal-Organic Frameworks in Sample Pretreatment. *Chinese Journal of Analytical Chemistry* **2013**, *41* (9), 1297-1300.
30. Eunsung, L.; Jungseok, H.; Kimoon, K., A Three-Dimensional Polyrotaxane Network. *Angewandte Chemie International Edition* **2000**, *39* (15), 2699-2701.
31. Hagrman, P. J.; Hagrman, D.; Zubietta, J., Organic-Inorganic Hybrid Materials: From "Simple" Coordination Polymers to Organodiamine-Templated Molybdenum Oxides. *Angewandte Chemie (International ed. in English)* **1999**, *38* (18), 2638-2684.
32. Moulton, B.; Lu, J.; Mondal, A.; Zaworotko, M. J., Nanoballs: nanoscale faceted polyhedra with large windows and cavities. *Chemical Communications* **2001**, (9), 863-864.
33. Song, P.; Liu, B.; Li, Y.; Yang, J.; Wang, Z.; Li, X., Two pillared-layer metal–organic frameworks constructed with Co(ii), 1,2,4,5-benzenetetracarboxylate, and 4,4'-bipyridine: syntheses, crystal structures, and gas adsorption properties. *CrystEngComm* **2012**, *14* (6), 2296-2301.

34. Pachfule, P.; Panda, T.; Dey, C.; Banerjee, R., Structural diversity in a series of metal–organic frameworks (MOFs) composed of divalent transition metals, 4,4'-bipyridine and a flexible carboxylic acid. *CrystEngComm* **2010**, *12* (8), 2381-2389.
35. Robin, A. Y.; Fromm, K. M., Coordination polymer networks with O- and N-donors: What they are, why and how they are made. *Coordination Chemistry Reviews* **2006**, *250* (15), 2127-2157.
36. Silva, P.; Valente, A. A.; Rocha, J.; Almeida Paz, F. A., Fast Microwave Synthesis of a Microporous Lanthanide–Organic Framework. *Crystal Growth & Design* **2010**, *10* (5), 2025-2028.
37. Ni, Z.; Masel, R. I., Rapid Production of Metal–Organic Frameworks via Microwave-Assisted Solvothermal Synthesis. *Journal of the American Chemical Society* **2006**, *128* (38), 12394-12395.
38. Wang, Z.; Cohen, S. M., Postsynthetic modification of metal–organic frameworks. *Chemical Society Reviews* **2009**, *38* (5), 1315-1329.
39. Kawano, M.; Kawamichi, T.; Haneda, T.; Kojima, T.; Fujita, M., The Modular Synthesis of Functional Porous Coordination Networks. *Journal of the American Chemical Society* **2007**, *129* (50), 15418-15419.
40. Ma, S.; Zhou, H.-C., A Metal–Organic Framework with Entatic Metal Centers Exhibiting High Gas Adsorption Affinity. *Journal of the American Chemical Society* **2006**, *128* (36), 11734-11735.
41. Moonhyun, O.; A., M. C., Ion Exchange as a Way of Controlling the Chemical Compositions of Nano- and Microparticles Made from Infinite Coordination Polymers. *Angewandte Chemie International Edition* **2006**, *45* (33), 5492-5494.
42. Wu, C.-D.; Hu, A.; Zhang, L.; Lin, W., A Homochiral Porous Metal–Organic Framework for Highly Enantioselective Heterogeneous Asymmetric Catalysis. *Journal of the American Chemical Society* **2005**, *127* (25), 8940-8941.
43. Gadzikwa, T.; Lu, G.; Stern, C. L.; Wilson, S. R.; Hupp, J. T.; Nguyen, S. T., Covalent surface modification of a metal–organic framework: selective surface engineering via Cu-catalyzed Huisgen cycloaddition. *Chemical Communications* **2008**, (43), 5493-5495.
44. Schröder, F.; Esken, D.; Cokoja, M.; van den Berg, M. W. E.; Lebedev, O. I.; Van Tendeloo, G.; Walaszek, B.; Buntkowsky, G.; Limbach, H.-H.; Chaudret, B.; Fischer, R. A., Ruthenium Nanoparticles inside Porous [Zn₄O(bdc)₃] by Hydrogenolysis of Adsorbed [Ru(cod)(cot)]: A Solid-State Reference System for Surfactant-Stabilized Ruthenium Colloids. *Journal of the American Chemical Society* **2008**, *130* (19), 6119-6130.
45. Mulfort, K. L.; Hupp, J. T., Chemical Reduction of Metal–Organic Framework Materials as a Method to Enhance Gas Uptake and Binding. *Journal of the American Chemical Society* **2007**, *129* (31), 9604-9605.
46. Ingleson, M. J.; Barrio, J. P.; Bacsá, J.; Dickinson, C.; Park, H.; Rosseinsky, M. J., Generation of a solid Brønsted acid site in a chiral framework. *Chemical Communications* **2008**, (11), 1287-1289.
47. Tanabe, K. K.; Cohen, S. M., Postsynthetic modification of metal–organic frameworks— a progress report. *Chemical Society Reviews* **2011**, *40* (2), 498-519.
48. Furukawa, H.; Cordova, K. E.; O’Keeffe, M.; Yaghi, O. M., The chemistry and applications of metal-organic frameworks. *Science* **2013**, *341* (6149), 1230444.
49. Eddaoudi, M.; Kim, J.; Rosi, N.; Vodak, D.; Wachter, J.; O’Keeffe, M.; Yaghi, O. M., Systematic Design of Pore Size and Functionality in Isoreticular MOFs and Their Application in Methane Storage. *Science* **2002**, *295* (5554), 469-472.
50. Rosi, N. L.; Eckert, J.; Eddaoudi, M.; Vodak, D. T.; Kim, J.; O’Keeffe, M.; Yaghi, O. M., Hydrogen storage in microporous metal-organic frameworks. *Science* **2003**, *300* (5622), 1127-9.

51. Kaye, S. S.; Dailly, A.; Yaghi, O. M.; Long, J. R., Impact of Preparation and Handling on the Hydrogen Storage Properties of Zn₄O(1,4-benzenedicarboxylate)₃ (MOF-5). *Journal of the American Chemical Society* **2007**, *129* (46), 14176-14177.
52. Rowsell, J. L. C.; Millward, A. R.; Park, K. S.; Yaghi, O. M., Hydrogen Sorption in Functionalized Metal–Organic Frameworks. *Journal of the American Chemical Society* **2004**, *126* (18), 5666-5667.
53. Wong-Foy, A. G.; Matzger, A. J.; Yaghi, O. M., Exceptional H₂ Saturation Uptake in Microporous Metal–Organic Frameworks. *Journal of the American Chemical Society* **2006**, *128* (11), 3494-3495.
54. Dybtsev, D. N.; Chun, H.; Kim, K., Rigid and flexible: a highly porous metal-organic framework with unusual guest-dependent dynamic behavior. *Angewandte Chemie (International ed. in English)* **2004**, *43* (38), 5033-6.
55. Lee, J. Y.; Olson, D. H.; Pan, L.; Emge, T. J.; Li, J., Microporous Metal–Organic Frameworks with High Gas Sorption and Separation Capacity. *Advanced Functional Materials* **2007**, *17* (8), 1255-1262.
56. Murray, L. J.; Dincă, M.; Long, J. R., Hydrogen storage in metal–organic frameworks. *Chemical Society Reviews* **2009**, *38* (5), 1294-1314.
57. Rowsell, J. L.; Yaghi, O. M., Strategies for hydrogen storage in metal–organic frameworks. *Angewandte Chemie (International ed. in English)* **2005**, *44* (30), 4670-9.
58. Collins, D. J.; Zhou, H.-C., Hydrogen storage in metal–organic frameworks. *Journal of Materials Chemistry* **2007**, *17* (30), 3154-3160.
59. Dinca, M.; Long, J. R., Hydrogen storage in microporous metal-organic frameworks with exposed metal sites. *Angewandte Chemie (International ed. in English)* **2008**, *47* (36), 6766-79.
60. Zhang, Z.; Yao, Z.-Z.; Xiang, S.; Chen, B., Perspective of microporous metal–organic frameworks for CO₂ capture and separation. *Energy & Environmental Science* **2014**, *7* (9), 2868-2899.
61. Furukawa, H.; Miller, M. A.; Yaghi, O. M., Independent verification of the saturation hydrogen uptake in MOF-177 and establishment of a benchmark for hydrogen adsorption in metal–organic frameworks. *Journal of Materials Chemistry* **2007**, *17* (30), 3197-3204.
62. Menon, V. C.; Komarneni, S., Porous Adsorbents for Vehicular Natural Gas Storage: A Review. *Journal of Porous Materials* **1998**, *5* (1), 43-58.
63. Wegrzyn, J.; Gurevich, M., Adsorbent storage of natural gas. *Applied Energy* **1996**, *55* (2), 71-83.
64. Burchell, T.; Rogers, M., Low Pressure Storage of Natural Gas for Vehicular Applications. SAE International: 2000.
65. Lozano-Castelló, D.; Alcañiz-Monge, J.; de la Casa-Lillo, M. A.; Cazorla-Amorós, D.; Linares-Solano, A., Advances in the study of methane storage in porous carbonaceous materials. *Fuel* **2002**, *81* (14), 1777-1803.
66. Orimo, S.-i.; Nakamori, Y.; Eliseo, J. R.; Züttel, A.; Jensen, C. M., Complex Hydrides for Hydrogen Storage. *Chemical Reviews* **2007**, *107* (10), 4111-4132.
67. Struzhkin, V. V.; Militzer, B.; Mao, W. L.; Mao, H.-k.; Hemley, R. J., Hydrogen Storage in Molecular Clathrates. *Chemical Reviews* **2007**, *107* (10), 4133-4151.
68. Gupta, A.; Lachance, J.; Sloan, E. D.; Koh, C. A., Measurements of methane hydrate heat of dissociation using high pressure differential scanning calorimetry. *Chemical Engineering Science* **2008**, *63* (24), 5848-5853.
69. Lee, H.; Lee, J.-w.; Kim, D. Y.; Park, J.; Seo, Y.-T.; Zeng, H.; Moudrakovski, I. L.; Ratcliffe, C. I.; Ripmeester, J. A., Tuning clathrate hydrates for hydrogen storage. In *Materials for Sustainable Energy*, pp 285-288.

70. Ma, S.; Sun, D.; Simmons, J. M.; Collier, C. D.; Yuan, D.; Zhou, H.-C., Metal-Organic Framework from an Anthracene Derivative Containing Nanoscopic Cages Exhibiting High Methane Uptake. *Journal of the American Chemical Society* **2008**, *130* (3), 1012-1016.
71. Celzard, A.; Fierro, V., Preparing a Suitable Material Designed for Methane Storage: A Comprehensive Report. *Energy & Fuels* **2005**, *19* (2), 573-583.
72. Celzard, A.; Albinia, A.; Jasienko-Halat, M.; Marêché, J. F.; Furdin, G., Methane storage capacities and pore textures of active carbons undergoing mechanical densification. *Carbon* **2005**, *43* (9), 1990-1999.
73. Holloway, S., Underground sequestration of carbon dioxide—a viable greenhouse gas mitigation option. *Energy* **2005**, *30* (11), 2318-2333.
74. Arenillas, A.; Smith, K. M.; Drage, T. C.; Snape, C. E., CO₂ capture using some fly ash-derived carbon materials. *Fuel* **2005**, *84* (17), 2204-2210.
75. Xu, X.; Song, C.; Miller, B. G.; Scaroni, A. W., Adsorption separation of carbon dioxide from flue gas of natural gas-fired boiler by a novel nanoporous “molecular basket” adsorbent. *Fuel Processing Technology* **2005**, *86* (14), 1457-1472.
76. Figueroa, J. D.; Fout, T.; Plasynski, S.; McIlvried, H.; Srivastava, R. D., Advances in CO₂ capture technology—The U.S. Department of Energy's Carbon Sequestration Program. *International Journal of Greenhouse Gas Control* **2008**, *2* (1), 9-20.
77. Li, F.; Fan, L.-S., Clean coal conversion processes – progress and challenges. *Energy & Environmental Science* **2008**, *1* (2), 248-267.
78. Millward, A. R.; Yaghi, O. M., Metal–Organic Frameworks with Exceptionally High Capacity for Storage of Carbon Dioxide at Room Temperature. *Journal of the American Chemical Society* **2005**, *127* (51), 17998-17999.
79. Llewellyn, P. L.; Bourrelly, S.; Serre, C.; Vimont, A.; Daturi, M.; Hamon, L.; De Weireld, G.; Chang, J.-S.; Hong, D.-Y.; Kyu Hwang, Y.; Hwa Jung, S.; Férey, G., High Uptakes of CO₂ and CH₄ in Mesoporous Metal–Organic Frameworks MIL-100 and MIL-101. *Langmuir* **2008**, *24* (14), 7245-7250.
80. Cavenati, S.; Grande, C. A.; Rodrigues, A. E., Adsorption Equilibrium of Methane, Carbon Dioxide, and Nitrogen on Zeolite 13X at High Pressures. *Journal of Chemical & Engineering Data* **2004**, *49* (4), 1095-1101.
81. Bloch, E.; Llewellyn, P. L.; Vincent, D.; Chaspoul, F.; Hornebecq, V., Adsorption of CO and CO₂ in Large Pore Sized Ag@SiO₂ Nanocomposite. *The Journal of Physical Chemistry C* **2010**, *114* (51), 22652-22658.
82. Hayashi, H.; Côté, A. P.; Furukawa, H.; O’Keeffe, M.; Yaghi, O. M., Zeolite A imidazolate frameworks. *Nature Materials* **2007**, *6*, 501.
83. Banerjee, R.; Phan, A.; Wang, B.; Knobler, C.; Furukawa, H.; O’Keeffe, M.; Yaghi, O. M., High-Throughput Synthesis of Zeolitic Imidazolate Frameworks and Application to CO₂ Capture. *Science* **2008**, *319* (5865), 939-943.
84. Wang, B.; Côté, A. P.; Furukawa, H.; O’Keeffe, M.; Yaghi, O. M., Colossal cages in zeolitic imidazolate frameworks as selective carbon dioxide reservoirs. *Nature* **2008**, *453*, 207.
85. Banerjee, R.; Furukawa, H.; Britt, D.; Knobler, C.; O’Keeffe, M.; Yaghi, O. M., Control of Pore Size and Functionality in Isorecticular Zeolitic Imidazolate Frameworks and their Carbon Dioxide Selective Capture Properties. *Journal of the American Chemical Society* **2009**, *131* (11), 3875-3877.
86. Couck, S.; Denayer, J. F. M.; Baron, G. V.; Rémy, T.; Gascon, J.; Kapteijn, F., An Amine-Functionalized MIL-53 Metal–Organic Framework with Large Separation Power for CO₂ and CH₄. *Journal of the American Chemical Society* **2009**, *131* (18), 6326-6327.
87. Dietzel, P. D. C.; Panella, B.; Hirscher, M.; Blom, R.; Fjellvåg, H., Hydrogen adsorption in a nickel based coordination polymer with open metal sites in the cylindrical cavities of the desolvated framework. *Chemical Communications* **2006**, (9), 959-961.

88. Allendorf, M. D.; Bauer, C. A.; Bhakta, R. K.; Houk, R. J. T., Luminescent metal–organic frameworks. *Chemical Society Reviews* **2009**, *38* (5), 1330-1352.
89. P., D. F.; A., B. C.; J., S. A.; G., G. P.; D., A. M., Scintillating Metal-Organic Frameworks: A New Class of Radiation Detection Materials. *Advanced Materials* **2009**, *21* (1), 95-101.
90. Dai, J.-C.; Wu, X.-T.; Fu, Z.-Y.; Cui, C.-P.; Hu, S.-M.; Du, W.-X.; Wu, L.-M.; Zhang, H.-H.; Sun, R.-Q., Synthesis, Structure, and Fluorescence of the Novel Cadmium(II)–Trimesate Coordination Polymers with Different Coordination Architectures. *Inorganic Chemistry* **2002**, *41* (6), 1391-1396.
91. B., C.; Y., Y.; F., Z.; G., L.; G., Q.; B., L. E., Luminescent Open Metal Sites within a Metal–Organic Framework for Sensing Small Molecules. *Advanced Materials* **2007**, *19* (13), 1693-1696.
92. Chen, B.; Wang, L.; Xiao, Y.; Fronczek, F. R.; Xue, M.; Cui, Y.; Qian, G., A luminescent metal-organic framework with Lewis basic pyridyl sites for the sensing of metal ions. *Angewandte Chemie (International ed. in English)* **2009**, *48* (3), 500-3.
93. Chen, B.; Wang, L.; Zapata, F.; Qian, G.; Lobkovsky, E. B., A Luminescent Microporous Metal–Organic Framework for the Recognition and Sensing of Anions. *Journal of the American Chemical Society* **2008**, *130* (21), 6718-6719.
94. Anjian, L.; Kunhao, L.; Haohan, W.; H., O. D.; J., E. T.; Woosok, K.; Maochun, H.; Jing, L., A Luminescent Microporous Metal–Organic Framework for the Fast and Reversible Detection of High Explosives. *Angewandte Chemie International Edition* **2009**, *48* (13), 2334-2338.
95. Lee, J.; Farha, O. K.; Roberts, J.; Scheidt, K. A.; Nguyen, S. T.; Hupp, J. T., Metal-organic framework materials as catalysts. *Chemical Society Reviews* **2009**, *38* (5), 1450-1459.
96. Ma, L.; Lin, W., Unusual Interlocking and Interpenetration Lead to Highly Porous and Robust Metal–Organic Frameworks. *Angewandte Chemie International Edition* **2009**, *48* (20), 3637-3640.
97. Kitaura, R.; Onoyama, G.; Sakamoto, H.; Matsuda, R.; Noro, S. i.; Kitagawa, S., Immobilization of a Metallo Schiff Base into a Microporous Coordination Polymer. *Angewandte Chemie International Edition* **2004**, *43* (20), 2684-2687.
98. Ma, L.; Abney, C.; Lin, W., Enantioselective catalysis with homochiral metal–organic frameworks. *Chemical Society Reviews* **2009**, *38* (5), 1248-1256.
99. Lee, Y.; Kim, S.; Kang, J. K.; Cohen, S. M., Photocatalytic CO₂ reduction by a mixed metal (Zr/Ti), mixed ligand metal-organic framework under visible light irradiation. *Chemical Communications* **2015**, *51* (26), 5735-5738.
100. Li, Y.; Xu, H.; Ouyang, S.; Ye, J., Metal-organic frameworks for photocatalysis. *Physical Chemistry Chemical Physics* **2016**, *18* (11), 7563-7572.
101. Sun, L.; Campbell, M. G.; Dincă, M., Electrically Conductive Porous Metal–Organic Frameworks. *Angewandte Chemie International Edition* **2016**, *55* (11), 3566-3579.
102. Song, J. Y.; Ahmed, I.; Seo, P. W.; Jhung, S. H., UiO-66-Type Metal–Organic Framework with Free Carboxylic Acid: Versatile Adsorbents via H-bond for Both Aqueous and Nonaqueous Phases. *ACS Applied Materials & Interfaces* **2016**, *8* (40), 27394-27402.
103. Bueken, B.; Van Velthoven, N.; Willhammar, T.; Stassin, T.; Stassen, I.; Keen, D. A.; Baron, G. V.; Denayer, J. F. M.; Ameloot, R.; Bals, S.; De Vos, D.; Bennett, T. D., Gel-based morphological design of zirconium metal-organic frameworks. *Chemical Science* **2017**, *8* (5), 3939-3948.
104. Wang, C.; Liu, X.; Keser Demir, N.; Chen, J. P.; Li, K., Applications of water stable metal–organic frameworks. *Chemical Society Reviews* **2016**, *45* (18), 5107-5134.
105. Liu, X.; Inagaki, S.; Gong, J., Heterogeneous Molecular Systems for Photocatalytic CO₂ Reduction with Water Oxidation. *Angewandte Chemie (International ed. in English)* **2016**, *55* (48), 14924-14950.

106. Sun, M.; Yan, S.; Sun, Y.; Yang, X.; Guo, Z.; Du, J.; Chen, D.; Chen, P.; Xing, H., Enhancement of visible-light-driven CO₂ reduction performance using an amine-functionalized zirconium metal–organic framework. *Dalton Transactions* **2018**, *47* (3), 909–915.
107. Yan, S. C.; Ouyang, S. X.; Gao, J.; Yang, M.; Feng, J. Y.; Fan, X. X.; Wan, L. J.; Li, Z. S.; Ye, J. H.; Zhou, Y.; Zou, Z. G., A room-temperature reactive-template route to mesoporous ZnGa₂O₄ with improved photocatalytic activity in reduction of CO₂. *Angewandte Chemie (International ed. in English)* **2010**, *49* (36), 6400–4.
108. Yu, J.; Low, J.; Xiao, W.; Zhou, P.; Jaroniec, M., Enhanced photocatalytic CO₂-reduction activity of anatase TiO₂ by coexposed {001} and {101} facets. *J Am Chem Soc* **2014**, *136* (25), 8839–42.
109. Inoue, H.; Moriwaki, H.; Maeda, K.; Yoneyama, H., Photoreduction of carbon dioxide using chalcogenide semiconductor microcrystals. *Journal of Photochemistry and Photobiology A: Chemistry* **1995**, *86* (1), 191–196.
110. Lee, J.; Farha, O. K.; Roberts, J.; Scheidt, K. A.; Nguyen, S. T.; Hupp, J. T., Metal-organic framework materials as catalysts. *Chem Soc Rev* **2009**, *38* (5), 1450–9.
111. Li, L.; Zhang, S.; Xu, L.; Wang, J.; Shi, L.-X.; Chen, Z.-N.; Hong, M.; Luo, J., Effective visible-light driven CO₂ photoreduction via a promising bifunctional iridium coordination polymer. *Chemical Science* **2014**, *5* (10), 3808–3813.
112. Fu, Y.; Sun, D.; Chen, Y.; Huang, R.; Ding, Z.; Fu, X.; Li, Z., An amine-functionalized titanium metal-organic framework photocatalyst with visible-light-induced activity for CO₂ reduction. *Angewandte Chemie (International ed. in English)* **2012**, *51* (14), 3364–7.
113. Cavka, J. H.; Jakobsen, S.; Olsbye, U.; Guillou, N.; Lamberti, C.; Bordiga, S.; Lillerud, K. P., A new zirconium inorganic building brick forming metal organic frameworks with exceptional stability. *J Am Chem Soc* **2008**, *130* (42), 13850–1.
114. Zhang, S.; Li, L.; Zhao, S.; Sun, Z.; Luo, J., Construction of Interpenetrated Ruthenium Metal–Organic Frameworks as Stable Photocatalysts for CO₂ Reduction. *Inorganic Chemistry* **2015**, *54* (17), 8375–8379.
115. Xu, H. Q.; Hu, J.; Wang, D.; Li, Z.; Zhang, Q.; Luo, Y.; Yu, S. H.; Jiang, H. L., Visible-Light Photoreduction of CO₂ in a Metal-Organic Framework: Boosting Electron-Hole Separation via Electron Trap States. *J Am Chem Soc* **2015**, *137* (42), 13440–3.
116. Chen, D.; Xing, H.; Wang, C.; Su, Z., Highly efficient visible-light-driven CO₂ reduction to formate by a new anthracene-based zirconium MOF via dual catalytic routes. *Journal of Materials Chemistry A* **2016**, *4* (7), 2657–2662.
117. Gu, Z.-Y.; Park, J.; Raiff, A.; Wei, Z.; Zhou, H.-C., Metal–Organic Frameworks as Biomimetic Catalysts. *ChemCatChem* **2014**, *6* (1), 67–75.
118. Dhakshinamoorthy, A.; Opanasenko, M.; Čejka, J.; Garcia, H., Metal organic frameworks as heterogeneous catalysts for the production of fine chemicals. *Catalysis Science & Technology* **2013**, *3* (10), 2509–2540.
119. Liu, Y.; Xuan, W.; Cui, Y., Engineering Homochiral Metal-Organic Frameworks for Heterogeneous Asymmetric Catalysis and Enantioselective Separation. *Advanced Materials* **2010**, *22* (37), 4112–4135.
120. Corma, A.; García, H.; Llabrés i Xamena, F. X., Engineering Metal Organic Frameworks for Heterogeneous Catalysis. *Chemical Reviews* **2010**, *110* (8), 4606–4655.
121. Lu, X.; Ye, J.; Sun, Y.; Bogale, R. F.; Zhao, L.; Tian, P.; Ning, G., Ligand effects on the structural dimensionality and antibacterial activities of silver-based coordination polymers. *Dalton Transactions* **2014**, *43* (26), 10104–10113.
122. Fei, H.; Sampson, M. D.; Lee, Y.; Kubiak, C. P.; Cohen, S. M., Photocatalytic CO₂ Reduction to Formate Using a Mn(I) Molecular Catalyst in a Robust Metal–Organic Framework. *Inorganic Chemistry* **2015**, *54* (14), 6821–6828.

123. Manna, K.; Zhang, T.; Greene, F. X.; Lin, W., Bipyridine- and Phenanthroline-Based Metal–Organic Frameworks for Highly Efficient and Tandem Catalytic Organic Transformations via Directed C–H Activation. *Journal of the American Chemical Society* **2015**, *137* (7), 2665-2673.
124. Manna, K.; Zhang, T.; Lin, W., Postsynthetic Metalation of Bipyridyl-Containing Metal–Organic Frameworks for Highly Efficient Catalytic Organic Transformations. *Journal of the American Chemical Society* **2014**, *136* (18), 6566-6569.
125. Wang, C.; Liu, D.; Lin, W., Metal–Organic Frameworks as A Tunable Platform for Designing Functional Molecular Materials. *Journal of the American Chemical Society* **2013**, *135* (36), 13222-13234.
126. Zhang, S.; Yang, Y.; Xia, Z.-Q.; Liu, X.-Y.; Yang, Q.; Wei, Q.; Xie, G.; Chen, S.-P.; Gao, S.-L., Eu-MOFs with 2-(4-Carboxyphenyl)imidazo[4,5-f]-1,10-phenanthroline and Ditopic Carboxylates as Coligands: Synthesis, Structure, High Thermostability, and Luminescence Properties. *Inorganic Chemistry* **2014**, *53* (20), 10952-10963.
127. Cui, Y.; Yue, Y.; Qian, G.; Chen, B., Luminescent Functional Metal–Organic Frameworks. *Chemical Reviews* **2012**, *112* (2), 1126-1162.
128. Wu, Y.-P.; Xu, G.-W.; Dong, W.-W.; Zhao, J.; Li, D.-S.; Zhang, J.; Bu, X., Anionic Lanthanide MOFs as a Platform for Iron-Selective Sensing, Systematic Color Tuning, and Efficient Nanoparticle Catalysis. *Inorganic Chemistry* **2017**, *56* (3), 1402-1411.
129. Barkhordarian, A. A.; Kepert, C. J., Two new porous UiO-66-type zirconium frameworks; open aromatic N-donor sites and their post-synthetic methylation and metallation. *Journal of Materials Chemistry A* **2017**, *5* (11), 5612-5618.